



Swansea University  
Prifysgol Abertawe

# Investigating the Use of Crystal Plasticity Finite Element (CPFE) Modeling to Determine Ballistic Performance of Novel Titanium Alloys

---

**Jonathan Gordon MSc. BEng.**

**29/09/2017**

## Declaration

This work has not previously been accepted in substance for any degree and is not being concurrently submitted in candidature for any degree.

Signed ..... (candidate)

Date .....

### STATEMENT 1

This thesis is the result of my own investigations, except where otherwise stated. Where correction services have been used, the extent and nature of the correction is clearly marked in a footnote(s).

Other sources are acknowledged by footnotes giving explicit references. A bibliography is appended.

Signed ..... (candidate)

Date .....

### STATEMENT 2

I hereby give consent for my thesis, if accepted, to be available for photocopying and for inter-library loans **after expiry of a bar on access approved by the Swansea University.**

Signed ..... (candidate)

Date .....

## Summary

The demand for lightweight and strong alloys in the aviation industry, such as titanium 6Al-4V, has grown with the increase in air travel. The fan blades on aero engines which are usually made from titanium 6Al-4V are susceptible to high strain rate deformation due to bird strike or other events associated with engine failure. The desire to optimise titanium alloys has led to the desire for greater understanding of titanium deformation mechanics.

In this research a hyperelastic-viscoplastic single-crystal rate-dependent material model is proposed. This model allows for the slip families of crystals to have their own unique material properties assigned to them. The crystallographic orientation is governed through the use of Euler angles. These Euler angles define the initial slip system configuration within the crystal.

A method for generating computational microstructures known as representative volume elements for titanium 6Al-4V is detailed. The generated microstructures are compared to EBSD data and the correct volume fraction of beta phase is obtained. The average alpha grain size is also well matched but the beta grains are larger than found in the EBSD data set.

The constructed microstructure is then meshed with brick elements and the model is used to simulate its response to macro and micro scale loadings. The model captures the general trends but does not give an exact match to the experimental data.

## **Acknowledgements**

I would like to thank Professor E. A. de Souza Neto for his support and guidance on this project and valuable knowledge of continuum mechanics and simulations.

I would also like to thank Dr. Matthew Thomas and Mr. Roger Thomas of Timet UK Ltd. for their valuable insight into titanium microstructures and processes.

I would also like to thank Dr. N. Croft for his help in C language and the many hours of helping with error messages.

I would also like to thank Fauzan Adziman, Daniel de Bortoli and Benjamin Cousins for their help and informative discussions.

I would also like to say a big thank you to my girlfriend Suz Richards who has kept me going and encouraged me along with proof reading this thesis.

The Author Jonathan Gordon would like to acknowledge the support of the EPSRC (EP/I015507/1) funded EDT MATTER - Manufacturing Advances Through Training Engineering Researchers, Timet UK Ltd. and part-funding from the European Social Fund through the Welsh European Funding Office.”

## Contents

Declaration.....	i
Summary.....	ii
Acknowledgements.....	iii
Contents.....	iv
List of Figures.....	vii
List of Tables.....	ix
Chapter 1 Introduction.....	10
1.1 Motivation for Research.....	10
1.2 Why look at the microscale?.....	12
1.3 Modelling titanium alloys.....	12
1.3.1 Dislocation density-based crystal plasticity constitutive model for prismatic slip in $\alpha$ -titanium.....	12
1.3.2 Zerilli-Armstrong strength model.....	14
1.3.3 Cellular automaton model.....	15
1.3.4 Lengthscale-dependent, elastically anisotropic, physically based hcp crystal plasticity model.....	16
1.4 Layout of thesis.....	16
Chapter 2 Titanium alloys.....	17
2.1 Applications.....	17
2.2 The titanium microstructure.....	17
2.2.1 Titanium alloys and its phases.....	17
2.2.2 Effects of grain boundaries and grain size.....	20
2.2.3 Effect of heat treatment on titanium microstructure.....	21
2.2.4 Deformation mechanics.....	22
2.3 Micro mechanical testing.....	26
2.4 Alpha grain properties.....	28
2.5 $\beta$ phase properties.....	32
2.6 Physical impact testing.....	34
2.7 Electron Backscatter Diffraction.....	41

Chapter 3 Phenomenological model of single crystals .....	42
3.1 Continuum mechanics basic principles.....	42
3.1.1 Deformation gradient.....	42
3.1.2 Volume changes .....	43
3.1.3 Isochoric / volumetric split of the deformation gradient .....	44
3.1.4 Stretches and rotation .....	44
3.1.5 Strain measures.....	45
3.1.6 Velocity gradient .....	46
3.1.7 Stress measures.....	46
3.2 Continuum thermodynamics fundamental laws.....	48
3.2.1 Conservation of mass.....	49
3.2.2 Momentum balance .....	49
3.2.3 First and second principles .....	49
3.2.4 Clausius-Duhem inequality .....	50
3.3 Constitutive principles .....	50
3.3.1 Constitutive axioms .....	50
3.4 Phenomenological and micromechanical approaches .....	51
3.5 Anisotropic finite single crystal plasticity .....	51
3.5.1 General single crystal plasticity.....	52
3.6 Finite element in nonlinear solid mechanics.....	54
3.7 Homogenised deformation gradient.....	55
3.8 Minimum and actual RVE kinematical constraints .....	55
3.9 Equilibrium of RVE.....	56
3.10 Average of the First Piola-Kirchhoff stress .....	56
3.11 The Hill-Mandel principle of macrohomogeneity .....	57
3.12 The choice of kinematical constraints.....	57
3.13 Finite strain macroscopic stress tensor .....	59

3.14 Computational homogenisation finite element discretisation .....	59
Chapter 4 Finite element simulation of a multiscale model .....	62
4.1 Material model .....	62
4.1.1 Multi-surface plasticity .....	63
4.1.2 Return mapping algorithm .....	65
4.1.3 Computation of the tensor exponential .....	66
4.1.4 Exponential map derivative .....	66
4.1.5 Perić slip rate law .....	67
4.1.6 Exponential map-based integration algorithm .....	67
4.1.7 The local Newton-Raphson algorithm .....	68
Chapter 5 RVE-based multiscale modelling of polycrystals .....	69
5.1 RVE-based modelling .....	69
5.2 RVE generation .....	69
5.2.1 NEPER .....	71
5.2.2 Coupled MATLAB and Neper RVE generation .....	73
5.2.3 Trimming the EBSD data .....	75
5.2.4 RVE generated from EBSD data .....	75
Chapter 6 Simulations of Titanium-6AL-4V .....	78
6.1 EBSD data and RVE generation .....	80
6.2 Macroscale modelling of RVE .....	81
6.2.1 Rate independent case .....	81
6.2.2 High strain rate case .....	84
6.3 Microscopic modelling of RVE .....	87
Chapter 7 Conclusions .....	90
7.1 Research outcomes .....	90
7.2 Looking forward .....	90
Appendix .....	92
References .....	93

## List of Figures

<b>Figure 1.1:</b> Air traffic numbers (taken from [1]) .....	10
<b>Figure 1.2:</b> Number of reported animal strikes to civil aircraft from 1990- 2012 (taken from [2]).....	11
<b>Figure 2.1:</b> Phase diagram showing the effect of Vanadium on the beta transus temperature in titanium alloy with 6% Al [19]. .....	18
<b>Figure 2.2:</b> HCP preferential slip planes.....	19
<b>Figure 2.3:</b> Beta slip system families. ....	19
<b>Figure 2.4:</b> Heat treated microstructures (taken from [10])......	21
<b>Figure 2.5:</b> Adiabatic Shear Band Formation (taken from [27]).....	23
<b>Figure 2.6:</b> Three stages of shear band formation (taken from [27]).....	24
<b>Figure 2.7:</b> Tensile sample [33]. ....	26
<b>Figure 2.8:</b> Warwick's test set-up [33]. ....	27
<b>Figure 2.9:</b> CRSS for prism planes (image taken from [38]).....	30
<b>Figure 2.10:</b> CRSS for basal slip for four different concentrations of aluminium (image taken from [38]).....	30
<b>Figure 2.11:</b> CRSS for parallel to the c-axis (image taken from [38]).....	30
<b>Figure 2.12:</b> Variation of Young's modulus with inclination from the c-axis (image taken from [29]).....	32
<b>Figure 2.13:</b> Optical micrographs of over-aged equiaxed(g) and bimodal microstructures(f) (taken from [25]).....	36
<b>Figure 2.14:</b> Dong-Geun Lee et al. test set-up [25]. ....	37
<b>Figure 2.15:</b> B. Bhav Singh et al. test set-up [24].....	37
<b>Figure 2.16:</b> Example of petalling on the rear surface (taken from [24]). ....	38
<b>Figure 2.17:</b> Results from B. Bhav Singh et al. ballistic testing (taken from [24]). ....	39
<b>Figure 3.1:</b> Deformation gradient representation. ....	42
<b>Figure 3.2:</b> The determinant of the deformation gradient, governing the volume changes. ...	43
<b>Figure 3.3:</b> The First Piola-Kirchhoff stress tensor.....	48
<b>Figure 3.4:</b> Multiplicative decomposition of the deformation gradient [54]. ....	53
<b>Figure 3.5:</b> Periodic RVE boundary displacement function. ....	58
<b>Figure 5.1:</b> Neper terminal. ....	71
<b>Figure 5.2:</b> Laguerre tessellation diagram [79].....	72
<b>Figure 5.3:</b> Voronoi tessellation diagram [79]. ....	73



<b>Figure 5.4:</b> MATLAB code seed points. Green and red circles represent beta and alpha seed point respectively. ....	74
<b>Figure 5.5:</b> 102 Grain RVE created in GMSH from EBSD data. ....	76
<b>Figure 5.6:</b> Cross section view of RVE in GMSH, showing realistic geometries achieved by the voronoi method. ....	76
<b>Figure 6.1:</b> Process of RVE simulation, from RVE generation through to final results.....	79
<b>Figure 6.2:</b> Ti-6Al-4V EBSD map showing the variety of grain sizes and there distribution. ....	80
<b>Figure 6.3:</b> Comparison of True Stress - Strain curves for experimental and simulated Quasi-static rate case. ....	82
<b>Figure 6.4:</b> Grains in the final deformed configuration showing the positions of grain boundaries. The colouring is based on the material ID, not the grain orientation.....	83
<b>Figure 6.5:</b> Stress distributions on RVE for Quasi-static uniaxial tension. ....	84
<b>Figure 6.6:</b> Comparison of Experimental and simulation response to a high strain rate loading condition. ....	85
<b>Figure 6.7:</b> Grain deformation for high strain rate loading .....	86
<b>Figure 6.8:</b> Distribution of stresses on RVE for high strain rate.....	87
<b>Figure 6.9:</b> True stress -strain response of the RVE. ....	88
<b>Figure 6.10:</b> Stress distribution for shear loading in microscale. ....	89
<b>Figure 6.11:</b> Deformed grains in microscale shear. ....	89

## List of Tables

<b>Table 2.1:</b> CRSS values for commercially pure titanium.....	29
<b>Table 2.2:</b> BCC ratio table.....	33
<b>Table 2.3:</b> Heat treatments used to create microstructures [24].....	34
<b>Table 2.4:</b> Mechanical properties of the microstructures [24]. ....	34
<b>Table 2.5:</b> Heat treatments for microstructures [26]. ....	35
<b>Table 2.6:</b> Mechanical properties of microstructures [26]. ....	35
<b>Table 2.7:</b> Overaged microstructure's material properties [25]. ....	36
<b>Table 2.8:</b> B. Bhav Singh et al. ballistic test results [24]. ....	38
<b>Table 2.9:</b> Dong-Geun Lee ballistic test results [25]. ....	40

## Chapter 1 Introduction

This thesis is concerned with a development of a material model for use within a finite element frame work. The model is constructed for use with dual phase titanium alloys under high strain rate loadings at the micro-structural level.

### 1.1 Motivation for Research

The volume of air traffic has been increasing steadily for many years; Figure 1.1 shows this trend on a global perspective for the years 2000 – 2010 [1]. This increase in the aviation sector has possibly lead to the increase in the number of reported strikes on aircraft per year, the majority of these strikes have involved birds. The increase in number of strikes and the split of birds to other animals can be seen in Figure 1.2 [2].



**Figure 1.1:** Air traffic numbers (taken from [1]).

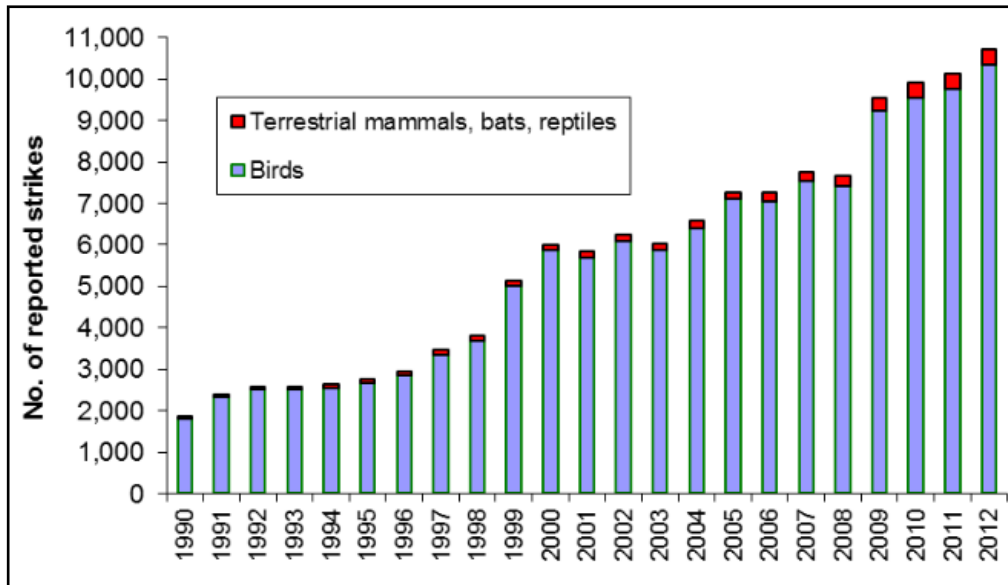


**Figure 1.2:** Number of reported animal strikes to civil aircraft from 1990- 2012 (taken from [2]).

Looking more in depth at American air travel and wildlife interaction also shows a trend of more bird strikes. In the four flyways of the United States the resident Canada goose population has risen by 3.6 fold since 1990 [3]. It should be noted that a typical Canada goose weighs 3.6 to 4.5 kg [4] which exceeds the bird certification standard for most aircraft engines [5], [6]. Canada geese also exhibit flocking behaviour which increases the chance of multiple strikes, with 598 of the total 1,403 strikes reported between 1990-2012 involving multiple geese [3]. It is also important to note that it is not compulsory to report bird strikes to the Federal Aviation Administration [7].

The rise in the goose population has come at a time in which more aircraft are using turbofan engines which are more susceptible to bird ingestion, [5] with their number, increasing from 4,148 in 1990 to 6,670 in 2008 [8]. It should also be noted that turbofan powered planes now tend to have two engine variants rather than three or four engine variants back in 1990. It is believed that Canada geese were responsible for the double engine failure of the A320 that was forced to land in the Hudson river in 2009 [9].

Aero engine manufacturers such as Rolls Royce are under increasing pressure to provide more efficient engines for future aircraft. This drive can be seen in documents from the European commission that quote:

*“In 2050 technologies and procedures available allow a 75% reduction in CO<sub>2</sub> emissions per passenger kilometre to support the ATAG target and a 90% reduction in NO<sub>x</sub> emissions.”* [10] This target is relative to typical new aircraft in 2000.

Reducing the weight of the engine will also lead to lighter engine support structures, which in turn reduces the overall weight of the plane. This of course has a knock on effect on the fuel consumption of the aircraft.

## **1.2 Why look at the microscale?**

Most currently available models are “descriptive” macroscale models that may describe the behaviour of a given alloy. Often the model parameters have been identified from experiments. Microscale models, on the other hand, are necessary if predictions of the macro behaviour of a given micro-structure are required. As such micro-modelling is essential in the “design” of alloys

## **1.3 Modelling titanium alloys**

Other modelling techniques have been applied to titanium alloys by others in the past. In the next few subsections some of these models are outlined to give the reader some background information on the modelling of titanium. For a more in-depth explanation of these models the reader is referred to the relative works of A. Alankar et al. [11], H.W. Mayer Jr. et al. [12], H. Pourian et al. [13], and F.P. E. Dunne et al. [14].

### **1.3.1 Dislocation density-based crystal plasticity constitutive model for prismatic slip in $\alpha$ -titanium**

In this model the slip activity is modelled using a set of dislocation density-based rate equations and different constitutive laws that are used to describe the velocities of edge and screw dislocations [11].

The total dislocation density is a combination of the total edge and screw type dislocations which is given in (1.1) [11]

$$\rho^\alpha = \rho_e^\alpha + \rho_s^\alpha. \quad (1.1)$$

Where  $\alpha$  represents prismatic slip system and  $e$  and  $s$  represent the edge and screw dislocation densities respectively. In this model the kinematics of shear rate on each

slip system is given in terms of the generalised Orowan form. The total plastic shear strain rate is given by:

$$\gamma^\alpha = b^\alpha (\rho_e^\alpha \bar{v}_e^\alpha + \rho_s^\alpha \bar{v}_s^\alpha) \text{sign}(\bar{\tau}^\alpha). \quad (1.2)$$

Where  $\bar{v}_e^\alpha$  and  $\bar{v}_s^\alpha$  represent the edge and screw dislocation velocities respectively. The screw dislocation segments are assumed to move via formation of kink pairs. The edge dislocation segments whose velocities are not affected by interstitials and impurities are pinned at the forest dislocation segments [11].

In this model the edge dislocation velocity is governed by (1.3) [11]

$$\bar{v}_e^\alpha = \bar{v}_{0,e} \exp \left[ -\frac{F_0}{k_B T} \left( 1 - \left( \frac{|\tau^\alpha|}{\tau_{0,e} + S^\alpha} \right)^{pe} \right)^{qe} \right]. \quad (1.3)$$

And the screw dislocation velocity is governed by (1.4) [11]

$$\bar{v}_s^\alpha = b^\alpha \frac{l^\alpha v_D}{l_0 l_0} \exp \left[ -\frac{F_{kink,0}}{k_B T} \left( 1 - \left( \frac{|\tau^\alpha|}{\tau_P} \right)^{ps} \right)^{qs} \right]. \quad (1.4)$$

Where  $\bar{v}_s^\alpha$  is the velocity of a straight screw dislocation segment  $l^\alpha$ ,  $l_0$  is the critical length for kink pair nucleation,  $v_D$  is the Debye frequency,  $\tau_P$  is the Peierls stress, and  $b^\alpha$  is the magnitude of the Burgers vector.

Another important part to this model is the forest hardening given by (1.5) [11]. The slip resistance  $S^\alpha$  on slip system  $\alpha$  is given by a modified Taylor type equation.

$$S^\alpha = \mu b^\alpha \sqrt{\sum_\beta g^{\alpha\beta} (\rho_e^\beta \mathbf{n}^\alpha \cdot \mathbf{t}^\beta + \rho_s^\beta \mathbf{n}^\alpha \cdot \mathbf{t}^\beta)}. \quad (1.5)$$

Where  $\mu$  is the shear modulus,  $g^{\alpha\beta}$  is the latent hardening coefficient for slip systems  $\alpha$  and  $\beta$ , and  $\rho^\beta$  is the forest dislocation density.

The average segment length of the dislocation is given by (1.6) [11]

$$l^\alpha = \frac{\lambda}{\sqrt{\sum_\beta g^{\alpha\beta} (\rho_e^\beta \mathbf{n}^\alpha \cdot \mathbf{t}^\beta + \rho_s^\beta \mathbf{n}^\alpha \cdot \mathbf{t}^\beta)}} \quad (1.6)$$

This model is based on dislocation mechanics and as such needs to take into account the multiplication and annihilation of dislocations within the material. The edge and screw dislocation densities are described through the use of dislocation loops. This means that the edge dislocation density increases with the moving screw dislocations and vice versa and are governed by equations (1.7) and (1.8)

$$\rho_{e,gen}^{\alpha} = \frac{(\rho_s^{\alpha} \bar{v}_s^{\alpha})}{l^{\alpha}}, \quad (1.7)$$

$$\rho_{s,gen}^{\alpha} = \frac{(\rho_e^{\alpha} \bar{v}_e^{\alpha})}{l^{\alpha}}. \quad (1.8)$$

When two dislocations of opposite sign get within a critical distance they will annihilate each other. In the model the annihilation is governed by equations (1.9) and (1.10)

$$\dot{\rho}_{e,ann}^{\alpha} = -\frac{1}{2} \rho_e^{\alpha^2} R_e^{\alpha} \bar{v}_e^{\alpha}, \quad (1.9)$$

$$\dot{\rho}_{s,ann}^{\alpha} = -\frac{1}{2} \rho_s^{\alpha^2} R_s^{\alpha} \bar{v}_s^{\alpha}. \quad (1.10)$$

Where  $R_e^{\alpha}$  and  $R_s^{\alpha}$  are the critical distances for the edge and screw dislocation. These equations quantify how far the dislocations travel through a field of randomly distributed dislocations of opposite sign before they are annihilated.

In this simulation only one finite element brick consisting of 8 integration points coupled with periodic boundary conditions along the x, y and z directions is used. The z direction is identical to the tensile direction [11].

### 1.3.2 Zerilli-Armstrong strength model

The Zerilli-Armstrong (ZA) strength model is based on the theory of dislocation mechanics of which there are two forms: one that relates to face-centred cubic (fcc) material and one that relates to body-centred cubic (bcc). In the case of titanium the bcc model gives better results due to the similarities in behaviour between hexagonally close packed (hcp) and bcc crystal structures [12]. The ZA model describes the yield flow through the following equation:

$$Y = c_0 + c_1 e^{(-c_3 T + c_4 T \ln \dot{\epsilon})} + c_5 \dot{\epsilon}^n. \quad (1.11)$$

Where  $T$  is the absolute temperature,  $\varepsilon$  is the equivalent plastic strain,  $\dot{\varepsilon}$  is the strain rate, and  $c_0, c_1, c_3, c_4, c_5$  and  $n$  are constants. The parameters in this model cannot be decoupled, therefore, a global fitting process is needed to determine the constants [12].

In this bcc form of the model, the strain rate and temperature behaviour of the flow stress are independent of strain effects. It must also be noted that the strain rate and temperature dependencies are coupled in this model [12].

### 1.3.3 Cellular automaton model

The Cellular automaton (CA) method has mostly been used to model micro-structural evolution, especially for static/dynamic recrystallisation [15][16]. The CA method has also been used to model the solidification process [13] and the motion of grain boundaries [17]. In the study by Pourian [13] an isotropic elastic stiffness was allocated, calculated by Fisher and Renken to determine the isotropic Youngs modulus and the Poisson ratio. Each cell's bulk and shear modulus can be calculated elastically from the cell's Youngs modulus and Poisson ratio [13]. This study only considers slip on the basal and prismatic slip systems, as only cold deformation was looked at [13]. In the study by Pourian [13] only one slip system was allowed to be active within each cell, therefore, only the maximum Schmid factor characterised each cell.

In the study the Critical Resolved Shear Stress (CRSS) value is used to calculate the hardening behaviour given by

$$\tau_{CRSS} = \tau_0 + H\gamma_s^{cum}. \quad (1.12)$$

Where  $\gamma_s^{cum}$  is the cumulative slip rate of all slip systems  $\gamma_s$ , and  $\tau_0$  is the initial value of the CRSS [13]. Pourian points out that the CA model has to be validated by a more reliable approach such as Finite Element (FE) in order to test the hypotheses [13].

In the FE simulations conducted by Pourian the behaviour of the central grain depends not only on the first degree neighbours but also on the behaviour of the other grains within the microstructure [13]. Due to the simple assumptions used in the Pourian application of the CA model it cannot capture the large field effects upon the aggregate when under loading conditions [13]. Pourian states that the FE simulation



results provide a good representation of mechanical behaviours at the macro and microscopic scales. This comes at a computational price, and prevents modelling of large numbers of grains or complex loading conditions [13].

#### **1.3.4 Lengthscale-dependent, elastically anisotropic, physically based hcp crystal plasticity model**

In a study by Dunne [14] on lengthscale-dependent, elastically anisotropic physically-based hcp crystal plasticity Ti-6Al-4V is used, as it is a near- $\alpha$  alloy and as such is mainly comprised of single hcp phase. Beta phase is, therefore, neglected from the simulation [14]. Another simplification for the model is that, for computational efficiency, slip is not permitted to occur on the pyramidal slip planes as well as being run as a 2D plane strain scenario [14]. In the study by Dunne the plane strain condition is imposed by ensuring that an equal and opposite elastic out-of-plane strain is imposed, such that the total out-of-plane strain remains zero [14]. This condition leads to the model sometimes being over-constrained when coupled with certain crystallographic orientations. For example, when the c-axis is normal to both the out-of-plane direction and the loading direction. This can lead to higher stresses than expected. In the study Dunne simply chooses to avoid crystallographic orientations that cause this scenario [14].

### **1.4 Layout of thesis**

Chapter 2 discusses the physical aspects of titanium alloys including their uses within the aero engine sector and microstructural configuration.

Chapter 3 gives information on Phenomenological model of single crystals from the base principles.

Chapter 4 outlines the finite element simulation of a multiscale model constructed for this research.

Chapter 5 discusses the process used to create the microstructural Representative Volume Elements (RVEs) used in this project and how they are simulated.

Chapter 6 shows results of simulations conducted in this research and what information this provides to titanium manufacturers.

Chapter 7 gives the conclusions of this thesis.

## **Chapter 2 Titanium alloys**

### **2.1 Applications**

Titanium alloys can be used in many applications from medical to aerospace. This is due to titanium's high strength to weight ratio and corrosion resistance. In the aerospace sector titanium is used extensively within the gas turbine engines. The majority of the front section of the aero engine is made of titanium alloys including the fan blades, fan containment casing, low pressure compressor, and high pressure compressor [18]. Strike cases tend to happen on any leading edge of the aircraft, including the front of the engine. In the case of the turbofan engine the fan blades constitute the leading edge. Due to the location of these components impact events due to Foreign Object Damage (FOD) such as ingestion of birds or runway debris is likely to occur.

The titanium alloys used in the leading edge components will therefore need to withstand impact loadings that might be seen in service. The materials deformation behaviour under these load cases needs to be known, this will lead safer and more efficient jet engine designs.

### **2.2 The titanium microstructure**

#### **2.2.1 Titanium alloys and its phases**

There are several different classes of titanium alloys:

1. Alpha: low strength, corrosion resistant
2. Near alpha: high strength, elevated temperature
3. Alpha/Beta: general purpose high strength, good toughness
4. Near beta: high strength, high toughness, good forgeability
5. Beta: very high strengths up to 1800 MPa

Each of these different classes of alloys has different amounts of the alpha or beta phases present within them. Ti-6Al-4V is the alloy that is commonly used for aero engine fan blades and blade containment casings and is alpha/beta class alloy. The alpha phase is a HCP crystal structure and the beta phase is a BCC crystal structure.

The amount of each phase present within the alloy is determined by the amount of alpha and beta stabilisers added.

Aluminium is a commonly used alpha phase stabiliser; the addition of aluminium will strengthen the alpha phase of the titanium microstructure, and will allow for the formation of the alpha/beta phase. Vanadium is used as a beta stabiliser, without the addition of which the beta phase would not exist at room temperature. Figure 2.1 shows the effect of Vanadium upon the beta transus temperature for a set amount of aluminium content. Adding an alpha stabiliser will increase the beta transus temperature, where as adding vanadium will decrease the beta transus temperature.

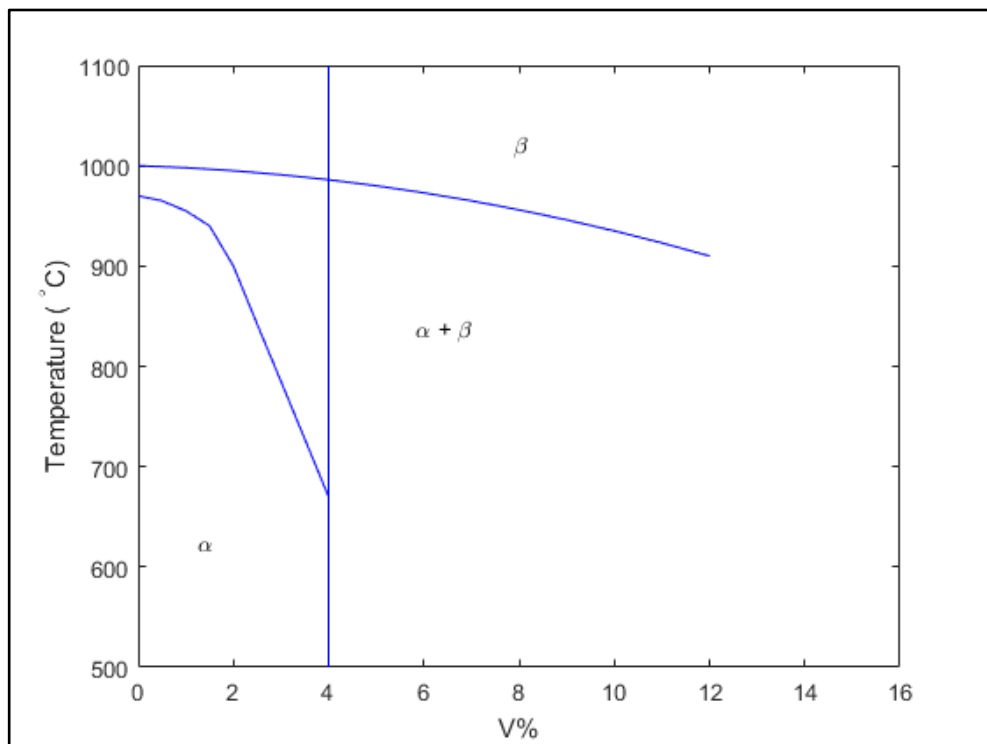


**Figure 2.1:** Phase diagram showing the effect of Vanadium on the beta transus temperature in titanium alloy with 6% Al [19].

In Ti-6Al-4V the alpha phase is the predominant phase within the microstructure. In plastic deformation, slip can occur on any or all of the thirty slip systems that are present within the crystal. These thirty slip systems fit into five slip families as seen in Figure 2.2 [20]. Each of these five families has its own Critical Resolved Shear Stress (CRSS) which governs the point of slip.

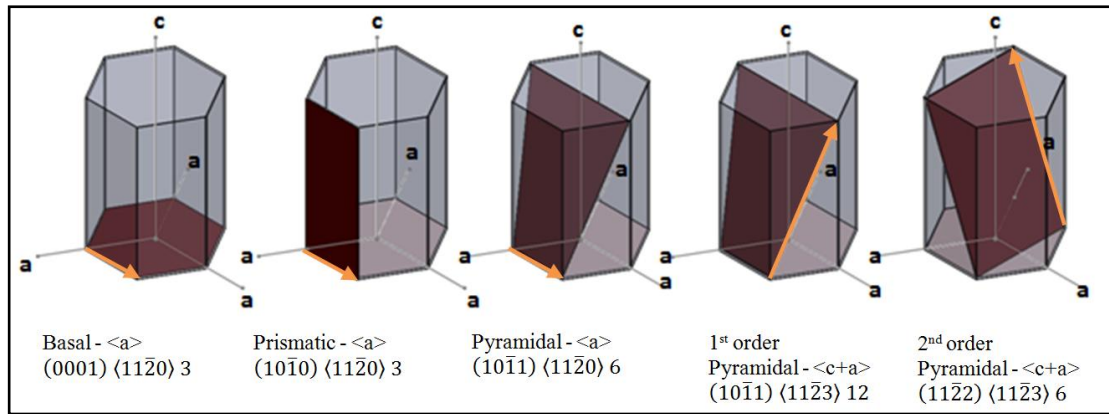


**Figure 2.2:** HCP preferential slip planes.

For the beta phase, however, there are three families of slip systems that give a total of forty eight slip systems. Figure 2.3 shows the configuration of the beta phase slip families.

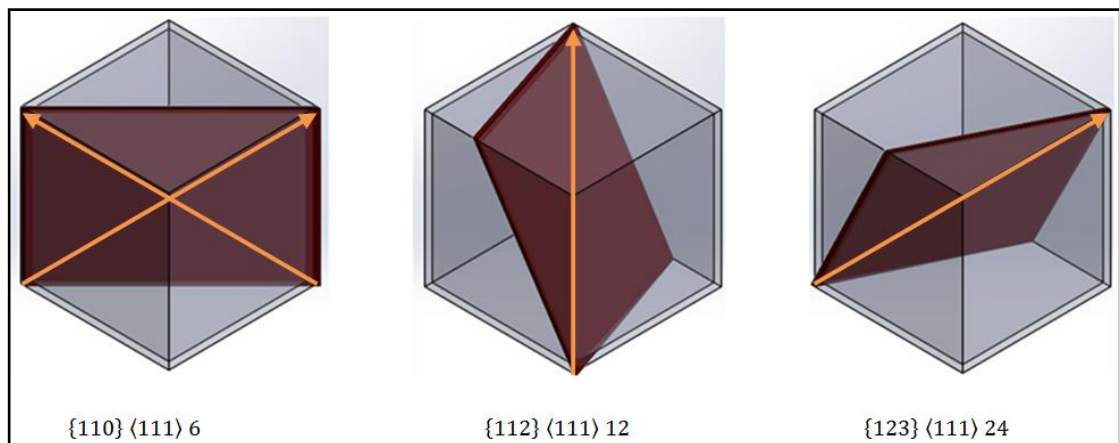


**Figure 2.3:** Beta slip system families.

It is convenient to think of the CRSS value as the yield point for the slip system. Slip will occur when the shear stress on the slip system is greater than the CRSS. The shear stress upon the system is governed by

$$\tau = \sigma \cos \phi \cos \lambda \quad (2.1)$$

Where  $\cos \phi \cos \lambda$  is the Schmidt factor of the slip system.

### 2.2.2 Effects of grain boundaries and grain size

Ti-6Al-4V is a polycrystalline alloy which means there will be grain boundaries present between the different colonies of  $\alpha$  and  $\beta$  phases and between different orientations of the same phase. These grain boundaries can have significant effect upon the macro properties of the alloy. The grain boundaries have high surface energy, and as such serve as preferential sites for phase transformations [21]. The grain boundaries impose conditions upon how the grains deform. A single crystal can deform freely upon its preferential slip plane and change its lattice orientation.

During the deformation of a polycrystalline alloy the grain boundaries continuity must be maintained so that the grain boundaries between the crystals remain intact [21]. This means the individual grains cannot deform as they wish and causes the activation of several slip systems within the grain itself. These slip systems do not have to be the preferential ones and therefore slip can occur on the non-close packed planes, thus causing more slip systems to be activated near the boundary [21].

Having these slip systems near the grain boundary causes the grain hardness near the edges to be higher compared to the hardness of the centre of the grain. As the grain size is reduced the overall hardness of the grain increases, thus giving greater strain hardening in fine grain metals compared to coarse grain metals [21].

The mechanical strengthening from grain boundaries has been proven by experiments, which showed that the yield stress increases with increased misorientation across the grain boundary [22].

It can therefore be seen that grain size can have a considerable effect on the alloys behaviour. One mathematical model used to determine yield stress from grain size is the Hall-Petch Relation given by (2.2) [23].

$$\sigma_0 = \sigma_i + kD^{-1/2} \quad (2.2)$$

Where  $\sigma_0$  is the yield stress,  $\sigma_i$  is the “friction stress” representing the overall resistance of the crystal lattice to dislocation movement.  $k$  is the “locking parameter” which measures the relative hardening contribution of the grain boundaries and  $D$  is the grain diameter.

### 2.2.3 Effect of heat treatment on titanium microstructure

As with many metals, titanium's microstructure can be affected by heat treatments. This allows for the titanium alloy to have different microstructures depending upon the processing route taken.

The Figure 2.4 shows four different microstructure which have come from the same baseline material and have undergone varying heat treatments.

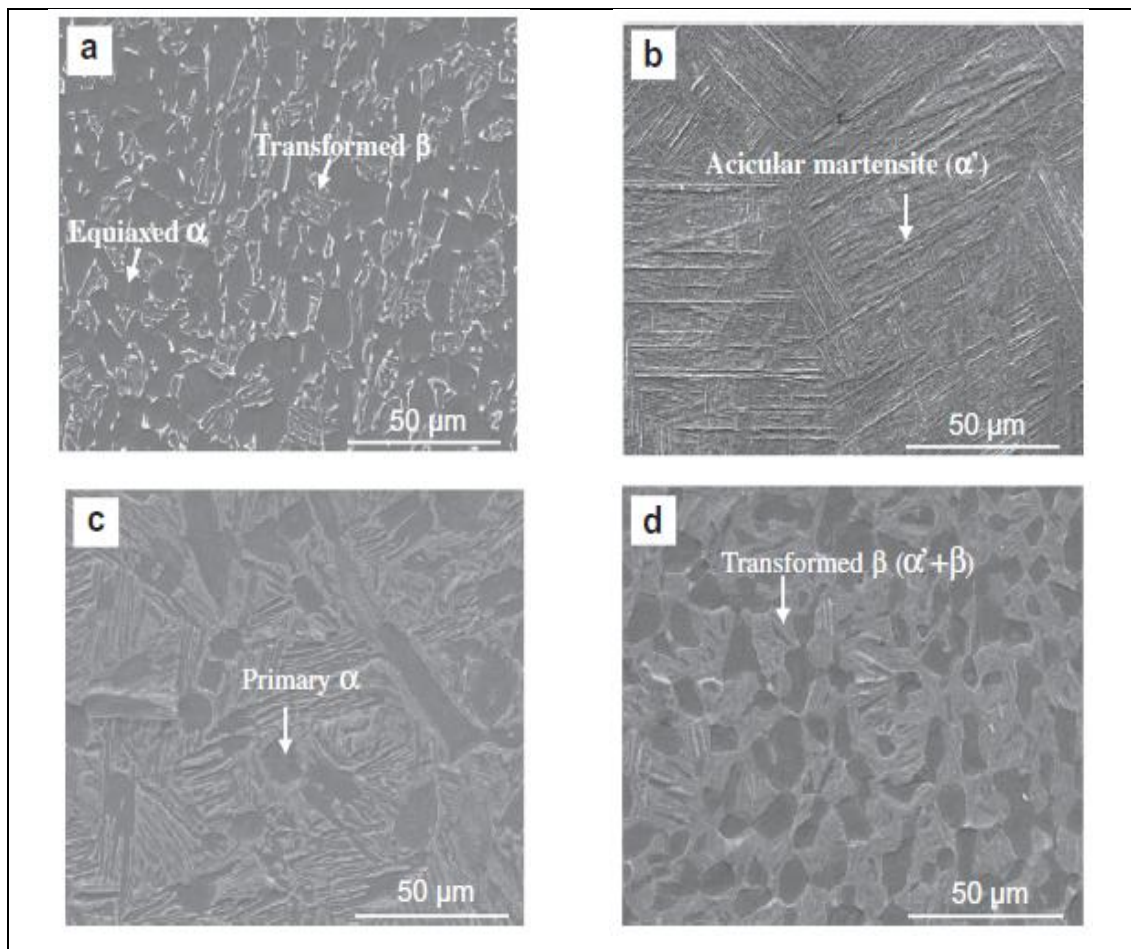


**Figure 2.4:** Heat treated microstructures (taken from [10]).

The microstructure a, from Figure 2.4, is the standard mill annealed product and has an equiaxed microstructure consisting of Primary alpha and Transformed beta. Microstructure b started as the standard microstructure given in a. Microstructure b was then heated to 1000°C and held for 1 hour at this temperature. It was then water quenched and then held at 540°C for 4 hours and then left to air cool [24]. This gives

microstructure b an acicular martensite ( $\alpha'$ ) in the prior beta grains. It is noted that microstructure b has been heated to above the beta transus temperature.

Microstructure c has been heated to 950°C for 1 hour and then water quenched and air cooled to the same conditions as the previous microstructure [24]. Microstructure d is heated to 950°C and again is treated the same as the previous example [24]. These heat treatments conducted on microstructures c and d lead to both having a bimodal structure with differing volume fractions of equiaxed primary alpha and transformed beta. Microstructure c has volume fraction of primary alpha of 21% and microstructure d has 40% [24].

Other heat treatments have been used to obtain microstructures by Dong-Geun Lee et al. [25], [26].

#### **2.2.4 Deformation mechanics**

In this section the possible deformation mechanisms that can occur in Ti-6Al-4V will be looked into, the first mechanism being Adiabatic Shear Bands (ASB). This is an important deformation mode generally observed in ballistic impact [27]. It is widely accepted that ASBs are triggered by a local inhomogeneity, such as geometric or dimensional variations, and possibly the presence of voids or inclusions in the microstructure [27].

During the formations of ASBs, temperatures higher than the beta transus temperature can be experienced in the localised area [27]. This can cause the transformation of the alpha phase to the beta phase and possible melting in this localised area [27]. When recrystallisation occurs a finer microstructure is created within the shear band [27]

ASBs tend to form in narrow bands of 5  $\mu\text{m}$  to 100  $\mu\text{m}$  across [28]. This finer microstructure gives rise to a higher microhardness compared to the surrounding microstructure outside of the shear band itself [27].

The formation of shear bands leads to the loss of the load carrying and energy dissipation capacity and, as such, ASBs are a precursor to failure in Ti-6Al-4V [28].

This can be illustrated in Figure 2.5 with the numbers on the graph referring to the image numbers. The formation of the shear band can be split into three distinct

sections. The first of these sections is when the deformation is homogeneous followed by the second stage where the deformation becomes inhomogeneous. The final stage is when the shear band is being formed. These stages can be seen in Figure 2.6, where the grid lines help define the stages. In the first stage the grid lines are straight but inclined, the second stage the grid lines are curved, and the third stage the grid lines are discontinuous [27].

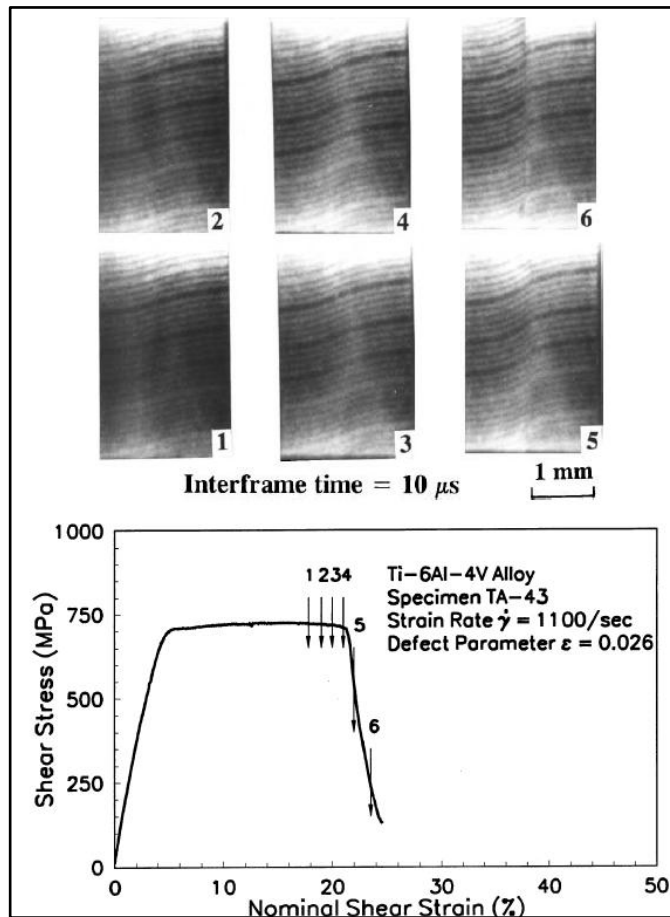


**Figure 2.5:** Adiabatic Shear Band Formation (taken from [27]).



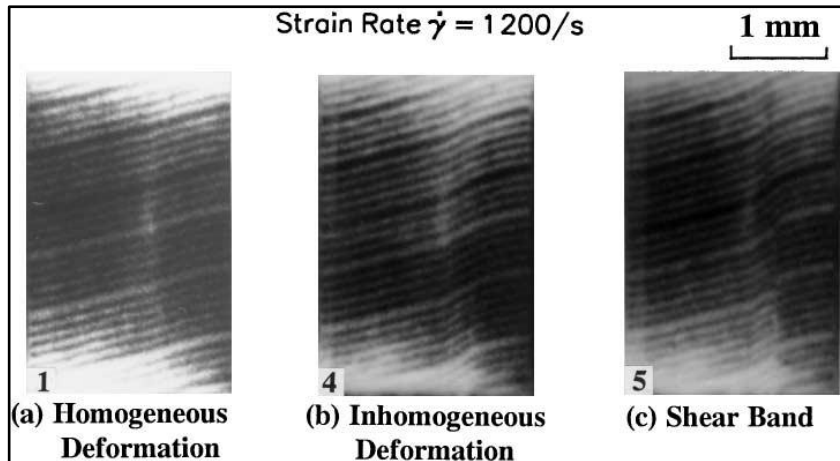


**Figure 2.6:** Three stages of shear band formation (taken from [27]).

Another important deformation mechanism is twinning. Twinning differs from slip in several ways. In slip the orientation of the crystal above and below the slip plane is the same after deformation as before, while in twinning there is an orientation change across the twin plane [21]. Generally it is considered slip occurs in discrete multiples of atomic spacing, whereas twinning can occur in much less than an atomic spacing. There are two types of twins referred to as “mechanical twins” and “annealing twins”, mechanical twins are produced in HCP metals through rapid rate loading cases such as impact [21]. Annealing twins are normally broader and have straighter edges compared to mechanical twins [21]. The presence of annealing twins gives an indication that the metal has been given mechanical deformation prior to annealing [21].

Titanium can experience twinning due to only having four independent slip systems, where as five are needed for homogeneous deformation in a polycrystalline material such as Ti-6Al-4V [15]. The  $\{10\bar{1}0\}$ ,  $\{10\bar{1}1\}$  and  $\{0001\}$  planes in HCP are the three most common slip planes with  $\langle 11\bar{2}0 \rangle$  as the direction. None of the aforementioned slip systems can support deformation in the  $c$ -direction and, as such, twin systems or  $\langle c + a \rangle$  pyramidal slip is necessary to maintain deformation compatibility [29].

The twinning process can be divided into four stages, the first of which being when twinning related dislocations accumulate in a location which may or may not lead to a successful twin [30]. In the second stage dislocations related to twinning reach a critical level that can lead to twin inception. This twin, during the third stage, forms

as a needle shape typically crossing a whole grain, which then thickens during the final stage [30].

In  $\alpha$  titanium there are four predominant twinning modes, of which the  $\{10\bar{1}2\}$  and  $\{11\bar{2}1\}$  are the planes that involve the smallest shear and simplest shuffles. The  $\{10\bar{1}2\}$  is preferred due to the Burgers vector for  $\langle a \rangle$  type slip along the  $\langle 11\bar{2}0 \rangle$  direction, as this does not have a c-axis component [29].

Due to the crystal structure of the  $\alpha$  phase the crystal is inherently isotropic, however, at the macroscale the effect of the elastic anisotropy seems to have little significance [14]. It can also be seen that the effect of anisotropic slip seems to outweigh the effect of elastic anisotropy [14].

Several authors have noted that the planar glide is the dominant deformation mechanism, with slip on the basal and prismatic slip systems being preferential. This is due to the fact that the CRSS value for pyramidal slip is generally seen to be three times higher than the previously mentioned slip systems [13], [14]. Some authors go as far as to say that for  $\alpha/\beta$  polycrystalline titanium alloys, single prismatic slip is the dominant mechanism in the majority of grains when the temperature is below 500 K [31], [32].

The primary basal and prismatic slip systems are not capable of deforming along the c-axis. Therefore, either twinning or  $\langle c + a \rangle$  modes, such as 1<sup>st</sup> and 2<sup>nd</sup> order pyramidal systems, are needed to allow for complete plastic deformation [33]. That being said, with Ti-6Al-4V's high aluminium content, twinning is unlikely to occur due to aluminium suppressing the activation [33],[34]. Grains in a polycrystalline environment stress the crystal nearly parallel to the c-axis such that the resolved shear stress on  $\langle a \rangle$  systems is almost 0. This can also be achieved by deforming the material at low temperatures or at high strain rates, where slip on  $\langle c + a \rangle$  systems is preferential, and has been observed near the grain boundaries [34].

### 2.3 Micro mechanical testing

Various mechanical tests need to be conducted to find the material properties at the grain level. In this section techniques used by other authors are explored.

Warwick [33] machined threaded cylindrical tensile specimens, which had a gauge diameter of 6.8 mm and a length of 30 mm. The tensile samples were machined so that the tensile axis was parallel to the rolling/extruding direction as seen in Figure 2.7 [33].

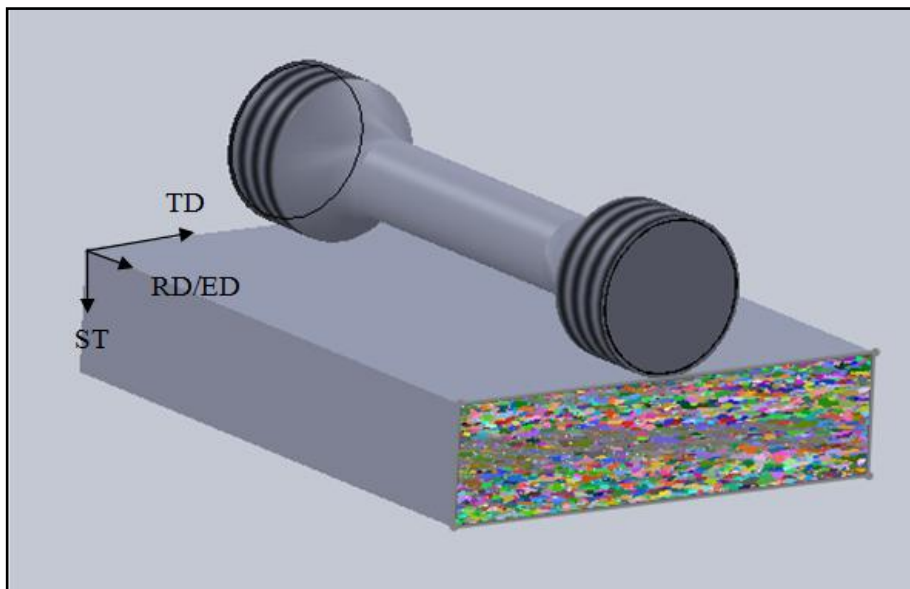


**Figure 2.7:** Tensile sample [33].

The samples were then loaded and diffraction measurements taken in a set-up shown in Figure 2.8.

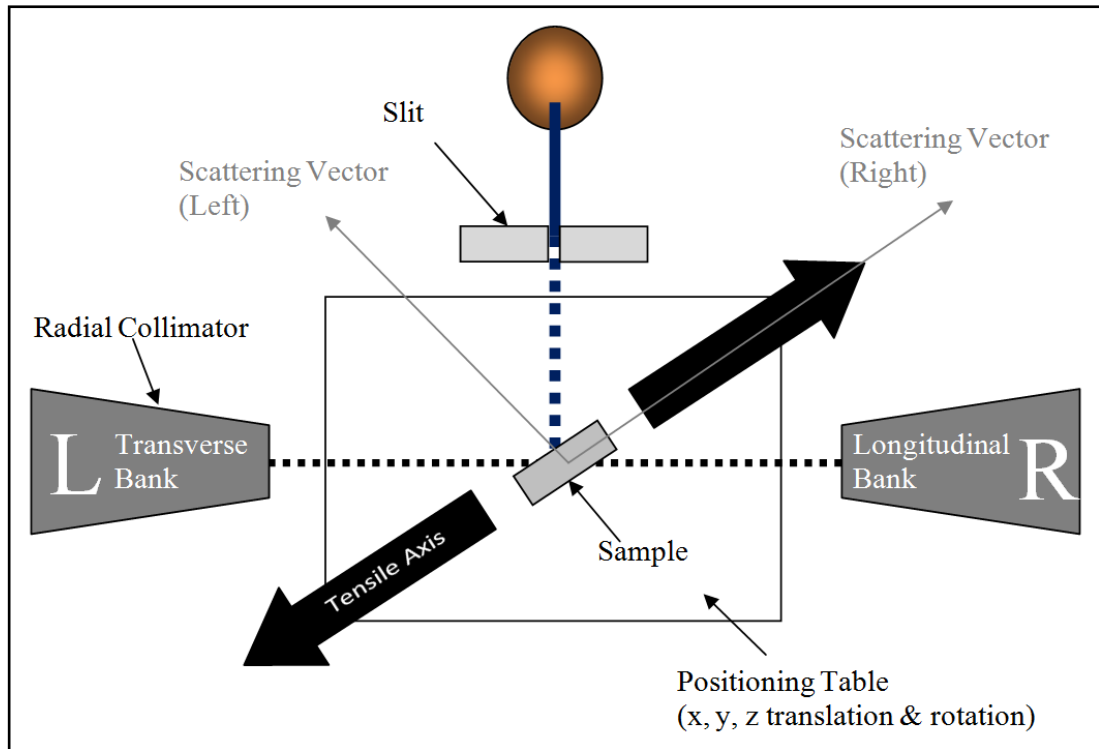


**Figure 2.8:** Warwick's test set-up [33].

The tensile specimens were tested at a strain rate of  $10^{-4} s^{-1}$  and angled at  $45^\circ$  to the incident beam with the detector banks perpendicular to the incident beam [33]. An extensometer was placed on the samples to provide an accurate measure of engineering stress [33]. The scattering volume provided by this set-up is  $\sim 4 \times 8 \times 4 \text{ mm}^3$ , with a counting time of 25 min per diffraction measurement [33]. Taking the gradient from the elastic graph from each grain orientation gives the diffracted elastic modulus for that orientation [33]. After the yield point has been reached, periodic unloading of the sample is conducted and measurements taken. This is due to the limited plastic flow that occurs when titanium alloys are kept at high homologous stresses [33]. So waiting for the neutron measurement would not be appropriate in this case [33].

In a study by Ledbetter electromagnetic-acoustic resonance was used. This requires putting the test sample into a solenoid coil which is in turn placed inside a cylindrical vacuum [35]. The specimen's temperature is then increased to  $1030^\circ\text{C}$  by the use of a heater next to the solenoid coil [35]. A biasing magnetic field is applied to the specimen through the use of two permanent magnets positioned outside the cylindrical vacuum. This excites and detect the free vibrations from the sample via

the Lorentz-force mechanism [35]. The outer magnets can be rotated about the vacuum cylinder central axis to excite different vibration modes [35].

Jones conducted research into the stress-strain dependence of slip in HCP metal, where the starting material was a very strongly textured plate, such that the  $\{1\bar{2}10\}$  system was parallel to the plate surface [36]. Due to the sharpness of the texture in the plate it approximately resembled a single crystal and, as such, samples were cut out from the plate at different angles to allow for compression tests along the various slip systems [36]. The various samples were either compressed or tensioned to 0.5% proof stress and once the value was known the CRSS values could be determined for the slip systems [36].

## 2.4 Alpha grain properties

Nano-indentation can be a useful technique to gain information on the mechanical properties of single grains. Gerday did several indentation tests per grain and only used results that were comparable for each grain. The reason for the selective results was to rule out the effects of the grain boundary or inhomogeneities in the grain [20].

Another way in which the properties can be attained is by the use of a micro-cantilever beam and systematically changing the crystal direction along it. The cantilever beam is created in the grain through the use of a Focused Ion Beam (FIB) [37].

J.Gong et al. used the results of these tests coupled with the finite element software ABAQUS. This was achieved with the use of the constitutive equation from Dunne's physically based crystal plasticity model with the velocity gradient defined as [37]

$$\mathbf{L}^P = \sum_j \rho b^2 v \exp\left(\frac{-\Delta F}{k_B T}\right) \sinh\left(\frac{(\tau^j - \tau_c^j)\Delta V}{k_B T}\right) \mathbf{s}^j \otimes \mathbf{n}^j. \quad (2.3)$$

Where  $\rho$  is the density of gliding dislocations,  $b$  is the magnitude of the Burgers vector,  $v$  is the jump attempt frequency of dislocations trying to pass energy barriers,  $k_B$  is the Boltzman constant,  $T$  is the absolute temperature,  $\Delta F$  is the Holmholtz free energy,  $\Delta V$  is the activation volume,  $\mathbf{s}^j$  is the unit slip direction and  $\mathbf{n}^j$  is the unit

normal to the slip plane of the  $j^{\text{th}}$  slip system, which has a CRSS of  $\tau_c^j$  and is under the shear stress of  $\tau^j$  [37].

The values for the CRSS are found from a reverse fitting process of the finite element model compared to the experimental load-displacement data from the micro-cantilever beams.

Table 2.1 shows the values of CRSS obtained by J. Gong et al. with target beam dimensions of 30  $\mu\text{m}$  long and 5  $\mu\text{m}$  wide with an equilateral triangle cross section [37].

**Table 2.1:** CRSS values for commercially pure titanium.

Slip System	Critical resolved shear stress (MPa)				Average (MPa)	Standard Deviation (MPa)
	Beam 1	Beam 2	Beam 3	Beam 4		
Prismatic Plane	184	188	185	168	181	8
Pyramidal Plane	483	468	474	472	474	5
Basal Plane	205	223	217	189	209	13

It must be noted that different authors obtain different results for the CRSS values due to different testing techniques. Criteria that can affect the CRSS value include the width of the cantilever, temperature, aluminium content, or if the alpha grain is subjected to a tensile load or compressive load.

The content of the aluminium within the alloy can affect the results of the CRSS along with the temperature. J. C. Williams et al. conducted compression tests on single crystal alpha grains at various temperature states. The following figures show the effect of aluminium and temperature on the CRSS for basal slip [38].

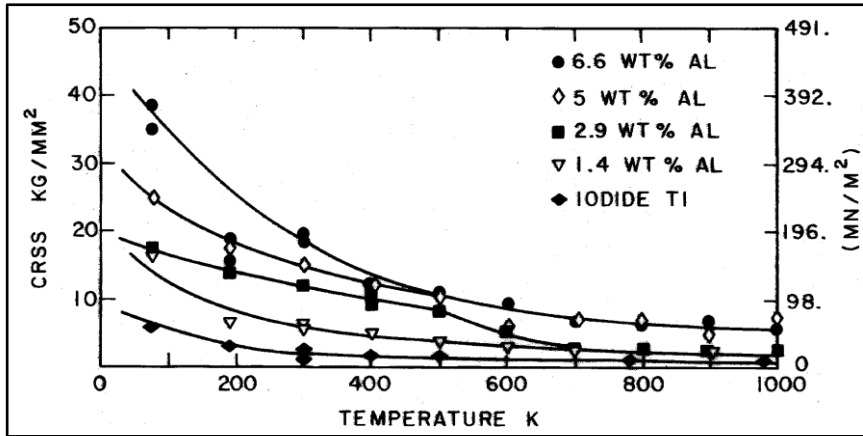


Figure 2.9: CRSS for prism planes (image taken from [38]).

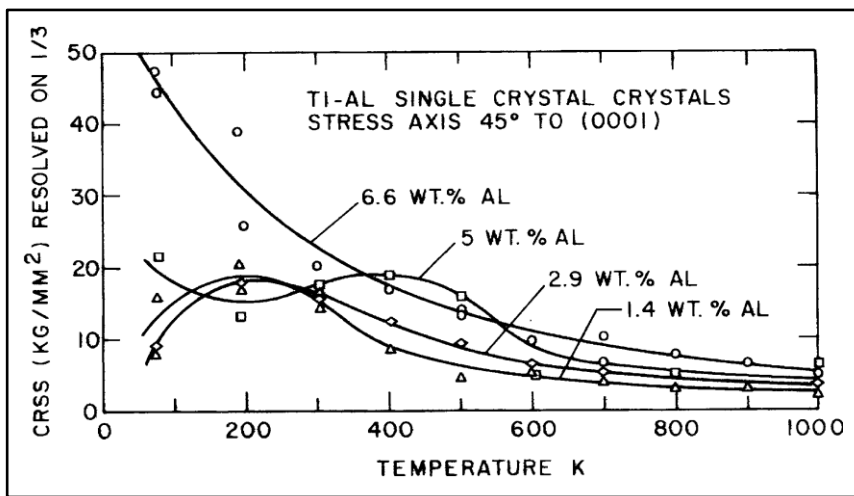


Figure 2.10: CRSS for basal slip for four different concentrations of aluminium (image taken from [38]).

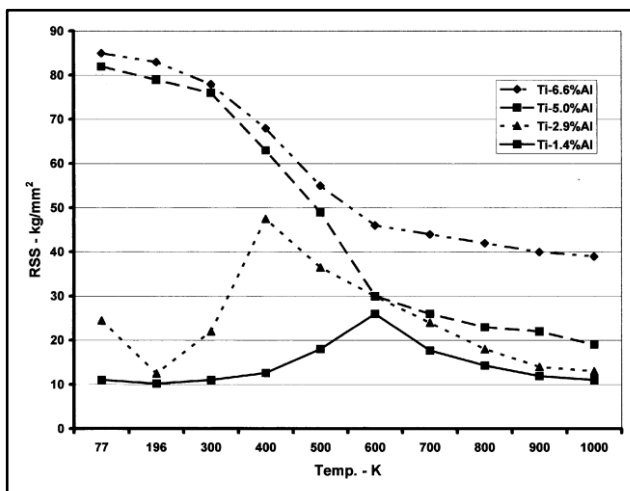


Figure 2.11: CRSS for parallel to the c-axis (image taken from [38]).

CRSS values in the alpha phase are a little varied, Han [39] quotes the Basal  $\langle a \rangle$ , Prismatic  $\langle a \rangle$ , and Pyramidal  $\langle a \rangle$  CRSS values as 420MPa, 370Mpa, and 490Mpa respectively. These values are in agreement with Bridier who also specifies the 2<sup>nd</sup> order pyramidal CRSS value as 590MPa [40]. However, these values differ to the ones quoted by Warwick who specifies the Basal  $\langle a \rangle$ , Prismatic  $\langle a \rangle$ , Pyramidal  $\langle a \rangle$ , Pyramidal 1<sup>st</sup> order  $\langle c+a \rangle$ , Pyramidal 2<sup>nd</sup> order  $\langle c+a \rangle$  as 330MPa, 350MPa, 380MPa, 490MPa, and 520MPa respectively [33]. Warwick also points out that in single crystal experiments,  $\langle c+a \rangle$  slip is found to be around 3 times higher than basal slip, where as he found in Ti-6Al-4V and Ti-834 that it was about 1.5 times higher [33].

In compression at 300 kelvin the CRSS values are 232.91, 193.68, 710.99 MPa for prism, basal and parallel to the c-axis respectively. It can be seen that the CRSS values of the slip systems are considerably lower in compression than in tension. This must be taken into account when creating and running a computational model of the alpha grains. The fact that the CRSS values are dependent on temperature will also mean that the constitutive model will have to run at a set temperature and the correct CRSS value will have to be set due to the following criteria: Temperature, aluminium content, and whether it is compression or tension.

In terms of the other Parameters, Han listed the hardening parameters of the basal, prismatic and pyramidal as 631.2Mpa, 436.2Mpa, and 436.2Mpa respectively [39]. This differs to Pourian who has a parameter H which is used in a similar way for the hardening variable used in a linear isotropic hardening model, for which the value given was 2500MPa [13]. As can be seen there is quite a bit of discrepancy between the two sets of values. The author believes that each slip system could in fact have its own hardening rate which agrees more with the values presented by Han. Bridier also has an inverse strain rate sensitivity parameter M which has the value of 15 [40].

Key information needed for alpha grain simulation is the Youngs modulus of the grain. Figure 2.12 shows how the Youngs modulus changes with the variation of angle from the c-axis, with the least stiff modulus being 99 GPa in the  $[10\bar{1}0]$  direction and the maximum being 131 GPa in the  $[0001]$  direction [41].



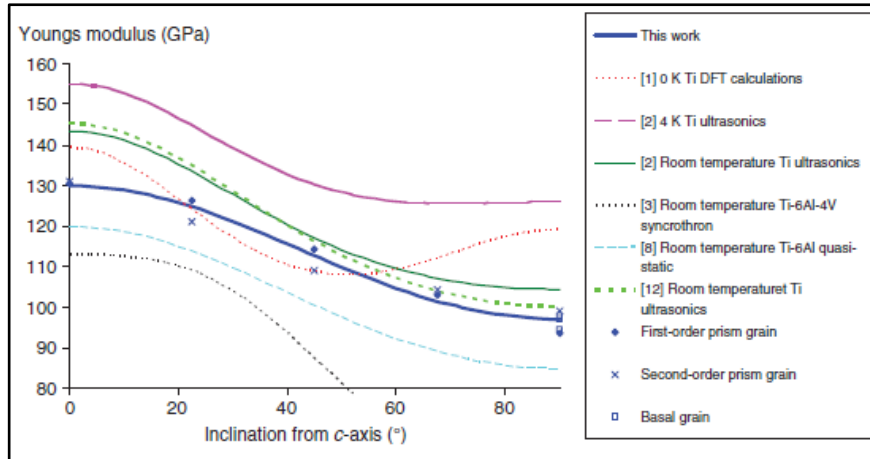


**Figure 2.12:** Variation of Young's modulus with inclination from the c-axis (image taken from [29]).

For the material model the material properties of each phase need to be known. Current literature has used the following material properties in simulations. The bulk modulus is given as 106.43 GPa and the shear modulus is given as 43.99 GPa [35]. As the elastic part of the model is isotropic, the values will be the same for all directions.

## 2.5 $\beta$ phase properties

Starting with the elastic properties the bulk modulus is 87.7GPa and the shear modulus is 20.7Gpa [35]. As the material model to be used is elastically isotropic these values will be the same in all directions.

For the BCC crystal structure the CRSS values for the  $\{110\}$ ,  $\{112\}$ , and  $\{123\}$  planes according to Warwick are 290MPa, 310MPa, and 350MPa respectively[33]. Bieler provides a table of ratios relative to the basal plane as seen below[42].

Though this table does not give the whole picture due to the fact it quotes a ratio for CRSS values to the  $\langle 111 \rangle$  slip direction. This direction is common to all BCC slip planes but the table gives the impression that all BCC slip planes have the same CRSS values, which is in disagreement with Warwick.

A.F. Gerday [43] also specifies the CRSS value for BCC slip to be 300 Mpa in Ti-5553, again this model assumes all the slip systems have the same CRSS values.

Gerday [43] provides a friction coefficient for  $\mu$  of 0.2 and provides a hardening parameter for the Pan model of 13,120 Mpa and for the BW model of 7,428 MPa. It

can be seen that there is quite a difference between the two models for the value of the hardening parameter.

**Table 2.2:** BCC ratio table.

BCC:	Prism:	Basal:	Pyramidal:		Comments
<111 >:	<a>:	<a>:	<c+a> :	<a>	Polycrystals and 13-16° off c-axis single crystal experiments unstable shear bands above 300°C (paton et al., 1973)
-:	0.8:	1:	2.1:	- (22°C)	
-:	0.3:	1:	-:	- (815°C)	
-:	0.2:	1:	1.6-3:	1	Matched 22°C yield stress, plastic strain ratio, yield loci, twinning CRSS 3x basal <a> Taylor model (Fundenberger et al., 1997)
0.33:	0.67:	1:	2:	0.67	Pyramidal <a> dominates, more basal than prism slip at low volume fractions of β VPSC (Dunst and Mecking, 1996)
0.25:	1:	1:	8:	-	Relative amount of prism slip increases, beta slip decreases with increasing strain, VPSC (Lebensohn and Canova, 1997)
-:	0.7:	1:	3:	-	Matched 815-955°C yield stress, plastic strain ratio with rate sensitive Taylor-Lapp with n=4 (Semiatin and Bieler, 2001 a,b)

## 2.6 Physical impact testing

Physical testing is conducted to provide an insight into how the sample will deform in the impact loading case. It can also be used to see how different microstructure affects the results from the test. B. Bhav Singh et al. created the microstructures shown in Figure 2.4 through the use of the heat treatments shown in Table 2.3.

Table 2.4 shows the mechanical properties associated with the different microstructures.

**Table 2.3:** Heat treatments used to create microstructures [24].

Designation	Heat treatment	Microstructure
a	Mill annealed	Equiaxed
b	1000°C/1 h/water quenched + 540°C /4 h/air cooling	Acicular
c	950°C /1 h/water quenched + 540°C /4 h/air cooling	Bimodal
d	900°C/1 h/water quenched + 540°C/4 h/air cooling	Bimodal

**Table 2.4:** Mechanical properties of the microstructures [24].

Designation	0.2% Yield Stress YS (MPa)	Ultimate Tensile Strength UTS (MPa)	Elongation to failure (%)	Area under engineering stress-strain curve (MJ/m <sup>3</sup> )	Hardness Vickers Hardness Number (VHN)
a	906 ± 5	961 ± 7	9.0 ± 1.0	92	285
b	1036 ± 18	1112 ± 20	4.5 ± 0.3	44	376
c	1050 ± 20	1143 ± 11	10.7 ± 0.5	120	335
d	1018 ± 17	1123 ± 12	12.7 ± 1.0	137	332

Dong-Geun Lee et al. also created microstructures through the use of heat treatments. The heat treatments used can be seen in Table 2.5 and the mechanical properties of these microstructures can be seen in Table 2.6.

**Table 2.5:** Heat treatments for microstructures [26].

Designation	Heat Treatment	Microstructure
e	Holding at 788°C for 6 h followed by furnace cooling	Equiaxed
f	Holding at 774°C for 6 h followed by furnace cooling, holding at 950°C for 1 hour and aging for 24 hours at 600°C and air cooled	Bimodal

**Table 2.6:** Mechanical properties of microstructures [26].

Designation	YS (MPa)	UTS (MPa)	Elongation (%)
e	1005 ± 26	1046 ± 24	18.0 ± 1.2
f	1048 ± 32	1095 ± 27	16.8 ± 0.9

In microstructure e there is a 5% by volume of the  $\beta$  phase which appears at the triple points of the  $\alpha$  grains and the  $\alpha$  phase accounts for 95% by volume of the alloy with an average  $\alpha$  grain size of 13  $\mu\text{m}$  [26]. Microstructure f consists of tempered martensite and  $\alpha$ , as well as residual  $\beta$ . The volume fractions of tempered martensite,  $\alpha$  and  $\beta$  are 50, 40 and 10 respectively [26].

It can be seen that the yield strength and the ultimate tensile strength are generally higher in the bimodal structures compared to that of the equiaxed microstructures, while the elongation is higher in the equiaxed microstructures.

Dong-Geun Lee et al. also over-aged microstructures e and f to produce nanometer-sized  $\alpha_2$  ( $\text{Ti}_3\text{Al}$ ) phases which can be homogeneously precipitated inside the  $\alpha$  phase, which leads to an improvement in the mechanical properties [12]. The over-aging process follows the same initial heat treatment as microstructures e and f except they are then over-aged at 540°C for 200 hours.

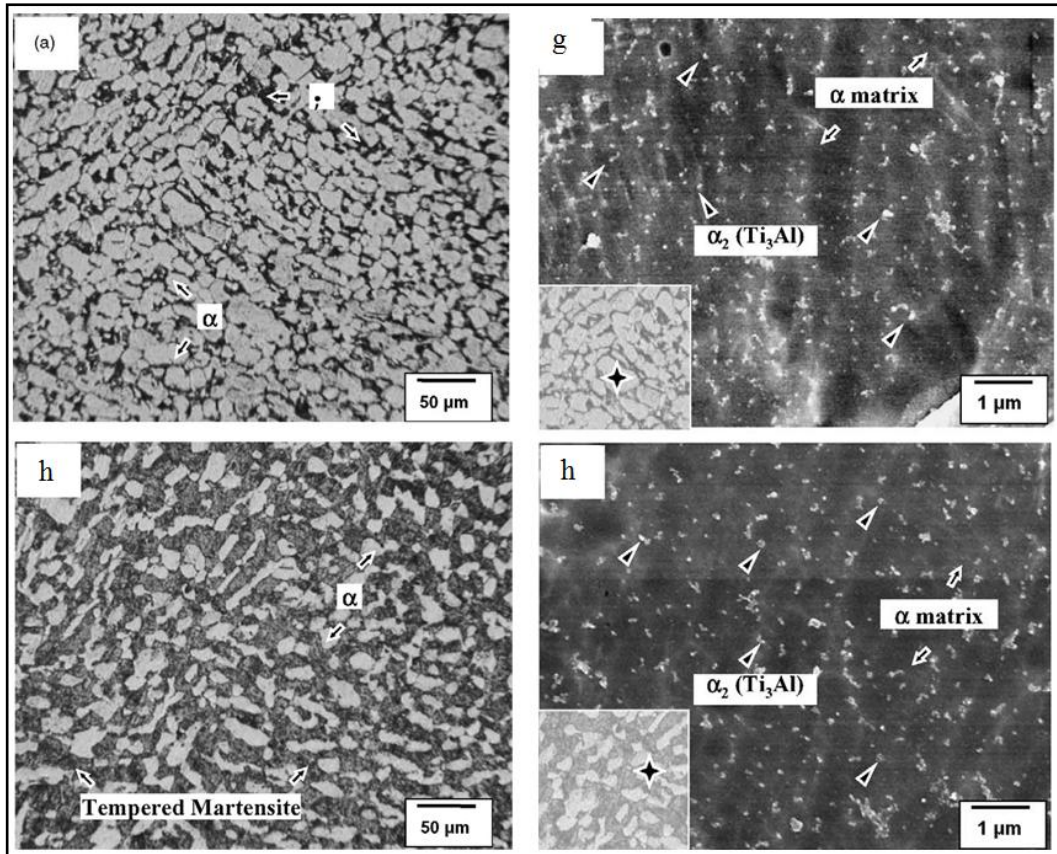


**Figure 2.13:** Optical micrographs of over-aged equiaxed(g) and bimodal microstructures(f) (taken from [25]).

The material properties for these microstructures are given in Table 2.7

**Table 2.7:** Overaged microstructure's material properties [25].

designation	YS (MPa)	UTS (MPa)	Elongation (%)
g	926	962	17.3
h	1020	1054	15.0

The following figures show the test set-up used by Dong-Geun Lee et al. and B. Bhav Singh et al.. As can be seen, these set-ups are very similar to each other, both having gun velocity probes and a target. The main difference is the spacing between the various parts of the apparatus. B. Bhav Singh et al. also uses velocity probes after the target plate to record the exit velocity of the projectile [24].

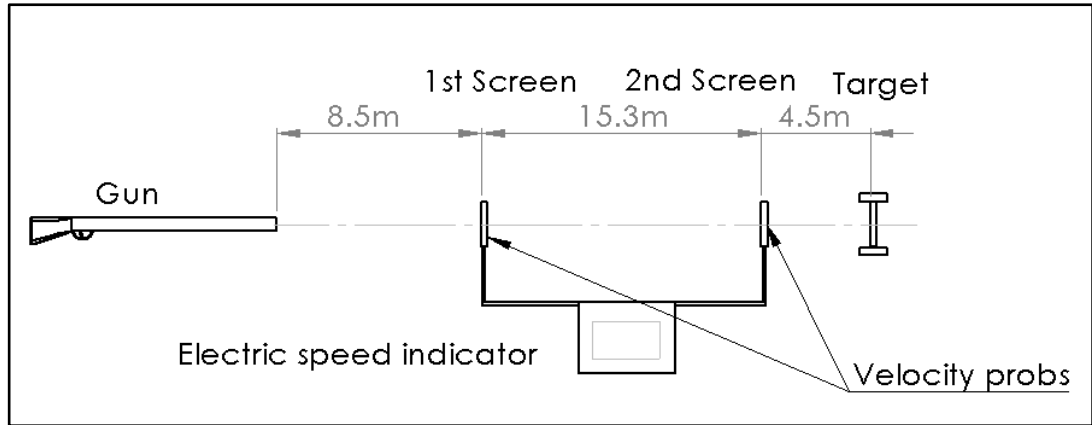


**Figure 2.14:** Dong-Geun Lee et al. test set-up [25].

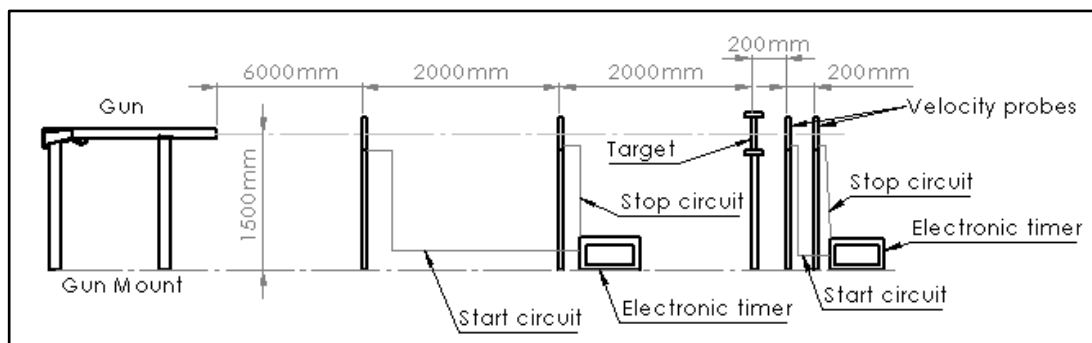


**Figure 2.15:** B. Bhav Singh et al. test set-up [24].

To analyse the results Dong-Geun Lee et al. compared the  $V_{50}$  ballistic limit ratio and mass efficiency value of the specimens. B. Bhav Singh et al. compared different plate thicknesses for the different microstructures and observed the rear face condition of the target.

The  $V_{50}$  ballistic limit ratio refers to the velocity of the projectile having a penetration probability of 50%, with higher values of  $V_{50}$  indicating better ballistic performance [26].

The mass efficiency  $E_m$  is the weight ratio against the Rolled Homogeneous Armour (RHA) having identical properties [12]. RHA is a steel based product that was commonly used on tanks and other armoured vehicles during World War 2 and as such has become a baseline test material for other armours to be compared against. Equation (2.4) shows the calculation for the mass efficiency [25].

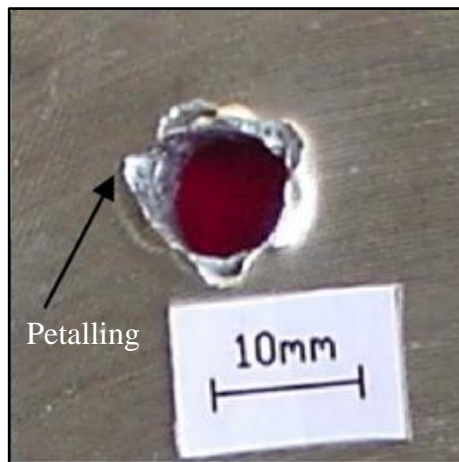
$$E_m = \frac{(\text{weight/area}) \text{ of RHA}}{(\text{weight/area}) \text{ of Ti - 6Al - 4V}} \text{ at same } V_{50}. \quad (2.4)$$

Table 2.8 gives the results of B. Bhav Singh et al. ballistic tests for different plate thickness and provides observations on the rear surface of the sample [24].

**Table 2.8:** B. Bhav Singh et al. ballistic test results [24].

Microstructure	Thickness (mm)	Perforation (yes/no)	Rear face observation
a	15.0	No	Smooth bulge
a	12.7	Yes	Petalling
b	15.0	No	Radial cracks
b	12.7	Yes	No petalling
c	15.0	No	Smooth surface
c	12.7	No	Smooth surface
c	10.0	Yes	Petalling
d	15.0	No	Smooth surface
d	12.7	No	Smooth bulge
d	10.0	Yes	Petalling

Figure 2.16 shows an example of the petalling on the rear surface of the test target. The presence of petalling indicates that plugging has occurred after bulging [24].



**Figure 2.16:** Example of petalling on the rear surface (taken from [24]).

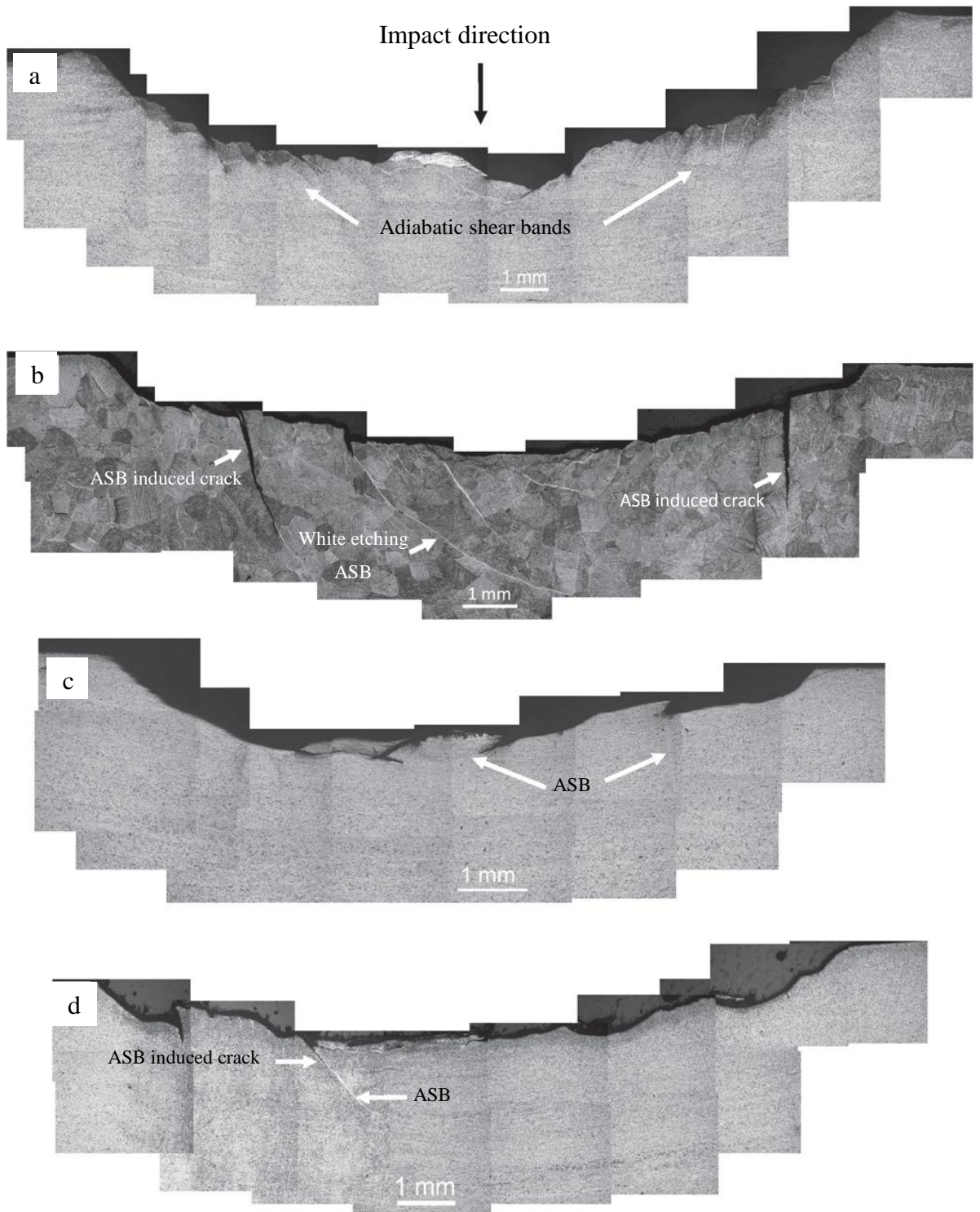


**Figure 2.17:** Results from B. Bhav Singh et al. ballistic testing (taken from [24]).

Figure 2.17 shows the results of the impact tests. In microstructure a, adiabatic shear bands have been formed as well as adiabatic shear band induced cracks. Microstructure b has a high number of adiabatic shear bands as well as two long adiabatic shear band induced cracks at the edges of the creator. Microstructures c and



d have less adiabatic shear bands compared to the standard product which is microstructure a. Microstructure c demonstrates no sign of any adiabatic shear band induced cracks and microstructure d has only a small number of induced cracks.

The reduced number of ASBs and ASB induced cracks in the bimodal microstructure shows that these types of microstructure have a higher energy absorption compared to the other types of microstructure. This may be due to the fact that the bimodal microstructures have a finer grain size compared to the other microstructures.

Table 2.9 gives the results to Dong-Geun Lee et al. ballistic tests in terms of  $V_{50}$  ballistic limit ratio and mass efficiency [25].

**Table 2.9:** Dong-Geun Lee ballistic test results [25].

Microstructure	Thickness of target specimen (mm)	$V_{50}$ ballistic limit ratio	Mass efficiency
Unaged equiaxed	20.0	1.00	1.23
Unaged bimodal	25.4	1.05	1.44
Aged equiaxed	25.4	1.01	1.34
Aged bimodal	25.4	1.06	1.46

In the aged equiaxed microstructure serious plastic flow is observed along the direction of the projectile. ASBs and cracks tend to form along the plastic flow lines. The number of voids formed in the aged specimens is greater than the un-aged specimens because of the  $\alpha_2$  precipitation. This causes the driving force behind adiabatic shear formation to decrease by as much as the deformation energy used for void formation and thus reducing the probability of adiabatic shear formation [25].

The number of voids in the bimodal microstructures is greater than the equiaxed microstructures. This is most likely due to the presence of tempered martensite as well as the  $\alpha$  and  $\beta$  phases increasing the number of void initiation sites [25]. It can be seen from the results that reducing the number of shear bands will increase the ballistic performance of the material.

## **2.7 Electron Backscatter Diffraction**

To be able to see the microstructure, Electron Backscatter Diffraction (EBSD) can be used. This can provide grain maps of the sample that will be tested. Using this technique the grain map can be imported into a finite element software where it can be analysed. The maps produced by the EBSD are 2D. Hamidreza Abdolvand et al. [44] then used the 2D maps and extrapolated them into 3D so that 3D boundary conditions could be imposed upon the finite element model. In Hamidreza Abdolvand et al.'s paper [44] the S1 samples were made from Zircaloy-2 slab with 14 mm gauge length, 3 mm width and 2 mm thickness. The S2 samples have the same starting dimensions but have been cold rolled to 10% and then heat treated at 720°C for 48 hours and provide an equiaxed grain structure with an average grain size of 50  $\mu\text{m}$  [44].

## Chapter 3 Phenomenological model of single crystals

### 3.1 Continuum mechanics basic principles

#### 3.1.1 Deformation gradient

The deformation gradient is a second order tensor denoted by  $\mathbf{F}$  and is defined by

$$\mathbf{F}(\mathbf{p}, t) = \nabla_{\mathbf{p}} \varphi(\mathbf{p}, t) = \frac{\partial \mathbf{x}_t}{\partial \mathbf{p}}. \quad (3.1)$$

Where  $\varphi(\mathbf{p}, t)$  can be expressed as

$$\varphi(\mathbf{p}, t) = \mathbf{p} + \mathbf{u}(\mathbf{p}, t), \quad (3.2)$$

with  $\varphi$  referring to a one to one mapping of each of the material points  $\mathbf{p}$  of a given body into a point  $\mathbf{x} = \varphi(\mathbf{p})$ . This therefore allows it to be written in the following form

$$\mathbf{F} = \mathbf{I} + \nabla_{\mathbf{p}} \mathbf{u}. \quad (3.3)$$

With this form being expressed in Cartesian components as

$$F_{ij} = \frac{\partial x_i}{\partial p_j} = \delta_{ij} + \frac{\partial u_i}{\partial p_j}. \quad (3.4)$$

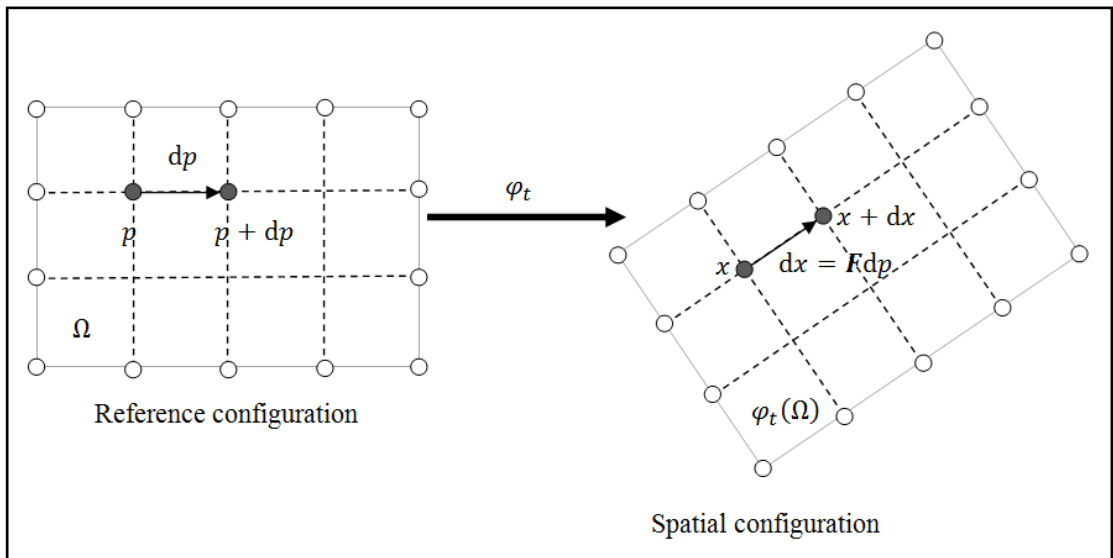


**Figure 3.1:** Deformation gradient representation.

The Figure 3.1 above shows how the deformation gradient governs the movement of particles between configurations. Let us then consider points  $\mathbf{p}$  and  $\mathbf{p} + d\mathbf{p}$  that are two neighbouring material points connected together by an infinitesimal fibre  $d\mathbf{p}$ . As the body is deformed by the deformation  $\varphi_t$  the points  $\mathbf{p}$  and  $\mathbf{p} + d\mathbf{p}$  are now mapped to  $\mathbf{x}$  and  $\mathbf{x} + d\mathbf{x}$  in the deformed configuration. It can be seen in (3.5) that the deformed configuration  $d\mathbf{x}$  of the material fibre is related to the initial configuration of the material fibre  $d\mathbf{p}$  through the use of the deformation gradient  $\mathbf{F}$ :

$$d\mathbf{x} = \mathbf{F} d\mathbf{p}. \quad (3.5)$$

### 3.1.2 Volume changes

The calculation of volume changes within continuum mechanics can be done by taking the determinant of the deformation gradient. Looking at Figure 3.2 where an infinitesimal volume  $dv_0$  is defined by the vectors  $d\mathbf{a}$ ,  $d\mathbf{b}$  and  $d\mathbf{c}$ . This volume is then deformed by  $\varphi_t$  which leads to the mapped form of the initial vectors  $\mathbf{F}d\mathbf{a}$ ,  $\mathbf{F}d\mathbf{b}$  and  $\mathbf{F}d\mathbf{c}$ , respectively. Therefore, the determinant of the deformation gradient is

$$J \equiv \det \mathbf{F} = \frac{(\mathbf{F}d\mathbf{a} \times \mathbf{F}d\mathbf{b}) \cdot \mathbf{F}d\mathbf{c}}{(d\mathbf{a} \times d\mathbf{b}) \cdot d\mathbf{c}}. \quad (3.6)$$

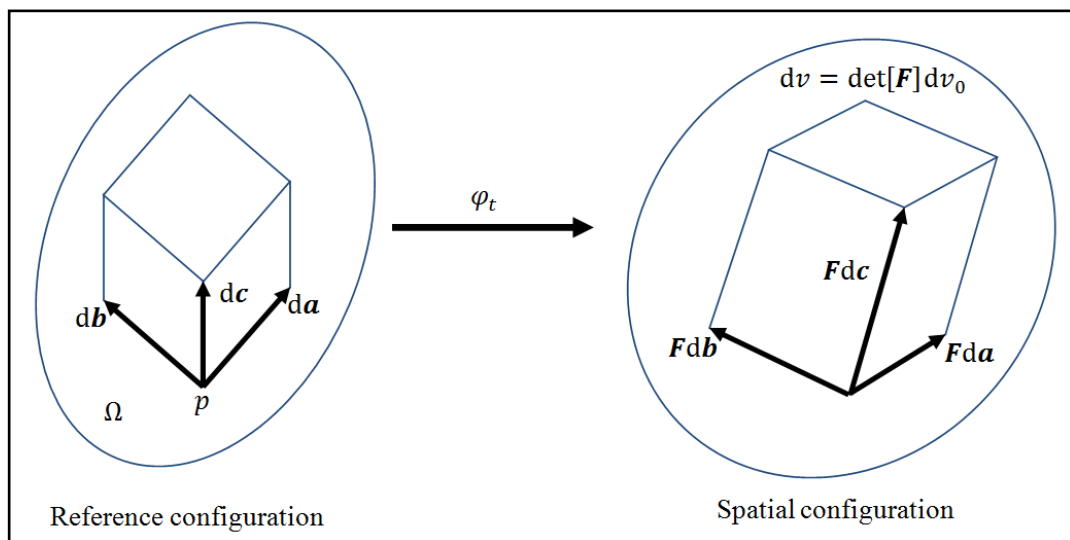


**Figure 3.2:** The determinant of the deformation gradient, governing the volume changes.

If, however,  $J = 0$  then volume has collapsed into a material particle. This is not feasible due to the fact that the body is not allowed to penetrate itself and, as such,  $J > 0$ . This is due to the fact that at the initial configuration  $\mathbf{F} = \mathbf{I}$  and thus  $J = 1$

### 3.1.3 Isochoric / volumetric split of the deformation gradient

Another concept that is widely used in computational plasticity is the isochoric / volumetric split, where the deformation gradient can be decomposed into an isochoric deformation followed by a pure volumetric deformation or vice versa. The deformation gradient can always be split multiplicatively as seen in

$$\mathbf{F} = \mathbf{F}_{iso}\mathbf{F}_v = \mathbf{F}_v\mathbf{F}_{iso} \quad (3.7)$$

Where  $\mathbf{F}_{iso}$  is the isochoric deformation gradient and  $\mathbf{F}_v$  is the volumetric deformation gradient. Each of these components can be calculated from the total deformation gradient and is given by

$$\mathbf{F}_v = (J)^{\frac{1}{3}}\mathbf{I}, \quad (3.8)$$

and

$$\mathbf{F}_{iso} = (J)^{-\frac{1}{3}}\mathbf{F}. \quad (3.9)$$

Due to  $\mathbf{F}_v$  being a purely volumetric deformation, it produces the same volumetric change as the total deformation gradient

$$\det \mathbf{F}_v = \left[ (J)^{\frac{1}{3}} \right]^3 \det \mathbf{I} = \det \mathbf{F}. \quad (3.10)$$

The isochoric component is the volume preserving deformation

$$\det \mathbf{F}_{iso} = \left[ (J)^{-\frac{1}{3}} \right]^3 \det \mathbf{F} = 1. \quad (3.11)$$

### 3.1.4 Stretches and rotation

The deformation gradient can be split using the polar decomposition theorem and thus the following is obtained

$$\mathbf{F} = \mathbf{R}\mathbf{U} = \mathbf{V}\mathbf{R}. \quad (3.12)$$

Where  $\mathbf{R}$  is a proper orthogonal tensor related to the local rotation, and  $\mathbf{U}$  and  $\mathbf{V}$  are symmetric positive definite tensors that are the right and left stretch tensors respectively. The stretch tensors are related to each other by the rotations such that

$$\mathbf{V} = \mathbf{R}\mathbf{U}\mathbf{R}^T . \quad (3.13)$$

$\mathbf{U}$  and  $\mathbf{V}$  can be expressed in terms of the right  $\mathbf{C}$  and left  $\mathbf{B}$  Cauchy-Green strain tensors as

$$\mathbf{U} = \sqrt{\mathbf{C}} , \quad \mathbf{V} = \sqrt{\mathbf{B}} . \quad (3.14)$$

The strain tensors can be related back to the deformation gradient as

$$\mathbf{C} = \mathbf{U}^2 = \mathbf{F}^T \mathbf{F} , \quad \mathbf{B} = \mathbf{V}^2 = \mathbf{F} \mathbf{F}^T . \quad (3.15)$$

### 3.1.5 Strain measures

Consider Figure 3.1, where the deformation of  $d\mathbf{p}$  due to the deformation  $\varphi_t$  is shown. The square of deformed configuration  $dx$  can be written as

$$\|dx\|^2 = \mathbf{C} d\mathbf{p} \cdot d\mathbf{p} = (\mathbf{I} + 2\mathbf{E}^{(2)})d\mathbf{p} \cdot d\mathbf{p} \quad (3.16)$$

Where  $\mathbf{E}^{(2)}$  is the Green-Lagrange strain measure and is defined by

$$\mathbf{E}^{(2)} = \frac{1}{2} (\mathbf{C} - \mathbf{I}) . \quad (3.17)$$

The Green-Lagrange strain measure is not unique way of quantifying strain. The Green-Lagrange belongs to a family of Lagrangian strain tensors, which are based on the Lagrangian triad [45]–[47]. This family includes Biot, Hencky and Almansi strain [45]–[47].

Strain can also be specified along the principle Eulerian directions and leads to the Eulerian family of strain tensors, which can be related to the Lagrangian family strain tensors through the following:

$$\varepsilon^{(m)} = \mathbf{R}\mathbf{E}^{(m)}\mathbf{R}^T . \quad (3.18)$$

### 3.1.6 Velocity gradient

The velocity gradient is a spatial field  $\mathbf{L}$  and is defined as:

$$\mathbf{L} = \nabla_x \mathbf{v} . \quad (3.19)$$

If the chain rule is applied to (3.19) then the following is obtained:

$$\mathbf{L} = \frac{\partial}{\partial t} \left( \frac{\partial \varphi}{\partial \mathbf{p}} \right) \frac{\partial \mathbf{p}}{\partial \mathbf{x}} = \dot{\mathbf{F}} \mathbf{F}^{-1} . \quad (3.20)$$

If the velocity gradient is split into its symmetric and skew components then the rate of deformation tensor  $\mathbf{D}$  and the spin tensor  $\mathbf{W}$  can be recovered.

$$\mathbf{D} = \text{sym}(\mathbf{L}), \quad \mathbf{W} = \text{skew}(\mathbf{L}) . \quad (3.21)$$

For a body under the influence of a uniform motion prescribed by the velocity gradient, the velocity field is defined as

$$\mathbf{v}(\mathbf{x}, t) = \mathbf{v}(\mathbf{y}, t) + \mathbf{L}(t)(\mathbf{x} - \mathbf{y}) . \quad (3.22)$$

If  $\mathbf{L}$  is decomposed into the symmetric and skew parts the above equation can be rewritten as

$$\mathbf{v}(\mathbf{x}, t) = \mathbf{v}^R(\mathbf{x}, t) + \mathbf{v}^S(\mathbf{x}, t) . \quad (3.23)$$

Where  $\mathbf{v}^R$  and  $\mathbf{v}^S$  are defined as:

$$\mathbf{v}^R(\mathbf{x}, t) = \mathbf{v}(\mathbf{y}, t) + \mathbf{W}(t)(\mathbf{x} - \mathbf{y}) , \quad (3.24)$$

$$\mathbf{v}^S(\mathbf{x}, t) = \mathbf{D}(t)(\mathbf{x} - \mathbf{y}) . \quad (3.25)$$

It can be seen that the velocity  $\mathbf{v}^R$  is associated with the spin tensor and, as such, it can be identified as a rigid velocity. It then becomes clear that the only term contributing to straining is the  $\mathbf{v}^S$  term, which is linked to the rate of deformation tensor.

### 3.1.7 Stress measures

The previous sections of this chapter have been concerned with the mathematics of the kinematics of deformation. So far no mention has been made of the forces that

act upon the body or how they are transferred through the material. These forces can be split into three groups:

1. **Boundary forces:** These are forces that act upon the surface of the body.
2. **Body forces:** These are forces that are acting upon the interior of the body.
3. **Internal interactions between adjacent parts of a body:** Internal forces come from the action of one part of the body upon the adjacent part and are transferred through the connecting surface.

It is seen that boundary forces and internal interactions can be considered the same type of force and can collectively be considered surface forces. The concept of stress can be introduced to describe mathematically the surface forces. Cauchy theorem is one of the fundamental concepts in understanding stress and is outlined in the next sub section.

### 3.1.7.1 Cauchy stress tensor

Cauchy's theorem, which has been formally proved by Wang and Truesdell, Gurtin, Martins, Marsden, Hughes, and Ciarlet [48]–[53], states that due to the axiom of momentum balance, the dependence of the surface force  $\mathbf{t}$  upon the unit normal  $\mathbf{n}$  is linear, therefore, the following is true:

$$\mathbf{t}(\mathbf{x}, \mathbf{n}) = \boldsymbol{\sigma}(\mathbf{x})\mathbf{n}. \quad (3.26)$$

Where  $\boldsymbol{\sigma}(\mathbf{x})$  is a symmetric tensor due to the balance of angular momentum and is a second order tensor called the Cauchy stress tensor, also known as the true stress tensor or stress tensor.

The Cauchy stress tensor can be split into two parts, the spherical part and the traceless part, this is convenient for constitutive modelling. The stress tensor is an additive split as seen in (3.27)

$$\boldsymbol{\sigma} = \mathbf{s} + p\mathbf{I}. \quad (3.27)$$

Where the invariant, called the hydrostatic pressure, is:

$$p \equiv \frac{1}{3}I_1(\boldsymbol{\sigma}) = \frac{1}{3} \text{tr} \boldsymbol{\sigma}. \quad (3.28)$$



### 3.1.7.2 First Piola-Kirchhoff stress

The First Piola-Kirchhoff stress is defined through the use of the counterpart of the traction vector  $\mathbf{t}$  which is denoted as  $\bar{\mathbf{t}}$ . This measures the force that acts across a surface whose normal is  $\mathbf{n}$  in the deformed configuration per unit reference area.

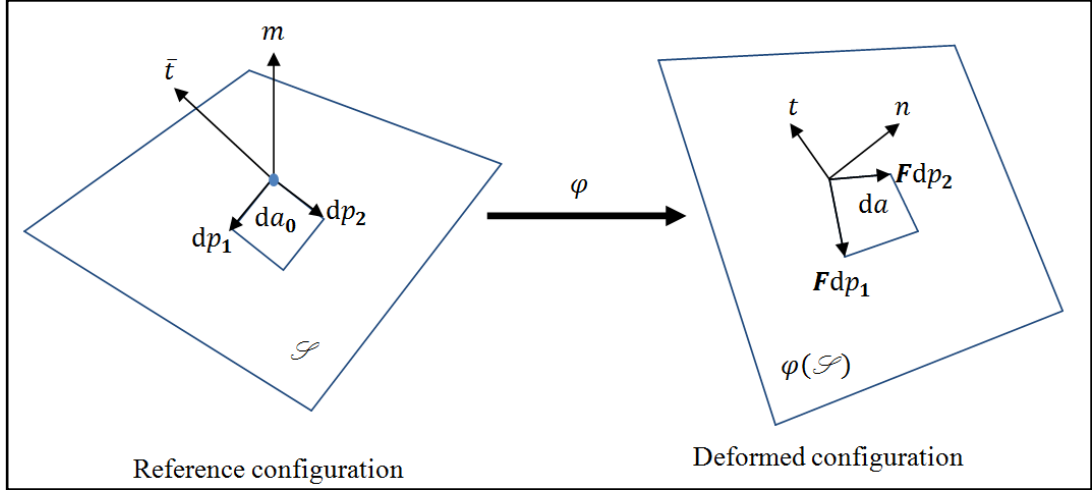


**Figure 3.3:** The First Piola-Kirchhoff stress tensor.

The First Piola-Kirchhoff stress tensor is defined by:

$$\mathbf{P} \equiv J\boldsymbol{\sigma}\mathbf{F}^{-T}. \quad (3.29)$$

Unlike the Cauchy stress, the First Piola-Kirchhoff stress is generally unsymmetric.

### 3.1.7.3 Second Piola-Kirchhoff stress and Kirchhoff stresses

The Second Piola-Kirchhoff stress tensor is defined as:

$$\mathbf{S} \equiv J\mathbf{F}^{-1}\boldsymbol{\sigma}\mathbf{F}^{-T}. \quad (3.30)$$

And the Kirchhoff stress tensor is:

$$\boldsymbol{\tau} \equiv J\boldsymbol{\sigma}. \quad (3.31)$$

## 3.2 Continuum thermodynamics fundamental laws

In this section the scalar fields  $\theta$ ,  $e$ ,  $s$  and  $r$  are introduced, and represent the temperature, specific internal energy, specific entropy and the density of heat production respectively. The vectors  $\mathbf{b}$  and  $\mathbf{q}$  represent body force and heat flux respectively.

### 3.2.1 Conservation of mass

The conservation of mass is given as:

$$\dot{\rho} + \rho \operatorname{div}_x \dot{\mathbf{u}} = 0. \quad (3.32)$$

Where  $\rho$  is the density and  $\operatorname{div}_x$  is the spatial divergence of  $(\cdot)$ .

### 3.2.2 Momentum balance

The momentum balance of a given body in the spatial or deformed configuration can be shown as:

$$\operatorname{div}_x \boldsymbol{\sigma} + \mathbf{b} = \rho \dot{\mathbf{u}} \quad \text{in } \varphi(\Omega), \quad (3.33)$$

$$\mathbf{t} = \boldsymbol{\sigma} \mathbf{n} \quad \text{in } \varphi(\partial\Omega). \quad (3.34)$$

The above equations are referred to as the strong form of equilibrium; these equations can also be expressed in terms of the reference configuration with the use of the First Piola-Kirchhoff stress tensor and are given as:

$$\operatorname{div}_p \mathbf{P} + \bar{\mathbf{b}} = \bar{\rho} \dot{\mathbf{u}} \quad \text{in } \Omega, \quad (3.35)$$

$$\bar{\mathbf{t}} = \mathbf{P} \mathbf{m} \quad \text{in } \partial\Omega. \quad (3.36)$$

Where  $\bar{\mathbf{b}}$  is the reference body force,  $\bar{\rho}$  is the reference density and  $\bar{\mathbf{t}}$  is the reference boundary traction, with  $\mathbf{m}$  being the outward normal to boundary surface in its initial configuration.

### 3.2.3 First and second principles

The first principle is the conservation of energy. This states that the rate of internal energy per unit of deformed volume must be equal to the sum of the stress power and heat production per unit deformed volume minus the spatial divergence of the heat flux. This is written mathematically as:

$$\rho \dot{e} = \boldsymbol{\sigma} : \mathbf{D} + \rho r - \operatorname{div}_x \mathbf{q}. \quad (3.37)$$

The second principle is the irreversibility of entropy production which can be written as:

$$\rho \dot{s} + \operatorname{div}_x \left[ \frac{\mathbf{q}}{\theta} \right] - \frac{\rho r}{\theta} \geq 0. \quad (3.38)$$

### 3.2.4 Clausius-Duhem inequality

By combining the first and second principles defined above the following inequality can be obtained [54]:

$$\rho \dot{s} + \operatorname{div}_x \left[ \frac{\mathbf{q}}{\theta} \right] - \frac{1}{\theta} (\rho \dot{e} - \boldsymbol{\sigma} : \mathbf{D} + \rho r - \operatorname{div}_x \mathbf{q}) \geq 0. \quad (3.39)$$

With the introduction of the specific free energy  $\psi$  as defined in (3.40) and the identity seen in (3.41) the Clausius-Duhem inequality can be obtained, and is seen in (3.42) [54].

$$\psi = e - \theta s, \quad (3.40)$$

$$\operatorname{div}_x \left[ \frac{\mathbf{q}}{\theta} \right] = \frac{1}{\theta} \operatorname{div}_x \mathbf{q} - \frac{1}{\theta^2} \mathbf{q} \cdot \nabla_x \theta, \quad (3.41)$$

$$\boldsymbol{\sigma} : \mathbf{D} - \rho (\dot{\psi} + s \dot{\theta}) - \frac{1}{\theta} \mathbf{q} \cdot \mathbf{g} \geq 0. \quad (3.42)$$

The left-hand side of the inequality represents the dissipation per unit deformed volume.

## 3.3 Constitutive principles

The principles outlined so far are valid for any continuum body, and do not take into account the material that the body is made from. A constitutive model must therefore be created that captures the material characteristics that the body is made from. To create a constitutive model the following axioms are needed as the starting point.

### 3.3.1 Constitutive axioms

Before laying out the axioms it is useful to introduce the definitions of thermokinetic and calorodynamic processes [55]. The thermokinetic process of a body is a pair of fields

$$\boldsymbol{\varphi}(\mathbf{p}, t) \text{ and } \theta(\mathbf{p}, t). \quad (3.43)$$

And the calorodynamic process of a body is a set of fields that satisfy the balance of momentum and the first and second principles of thermodynamics:

$$\boldsymbol{\sigma}(\mathbf{p}, t), e(\mathbf{p}, t), s(\mathbf{p}, t), r(\mathbf{p}, t), \mathbf{b}(\mathbf{p}, t), \mathbf{q}(\mathbf{p}, t). \quad (3.44)$$

The first of the continuum axioms is the principle of thermodynamic compatible determinism [55]. The principle states “The history of the thermokinetic process to which a neighbourhood of a point  $\mathbf{p}$  of a body has been subjected determines a calorodynamic process for a body at point  $\mathbf{p}$ ” [55]. The second axiom is the principle of material objectivity or frame invariance. This principle states “The material response is independent of the observer”. The third axiom is the material symmetry, where the symmetry group is defined as “The set of density preserving changes of reference configuration under which the material response functionals are not affected”.

### **3.4 Phenomenological and micromechanical approaches**

Two types of continuum modelling can be considered when creating a new material model, the phenomenological approach or the micromechanical approach.

Phenomenological models are used on elements of materials that are a homogeneous continuum, where the internal variables are directly related to the dissipative behaviour observed at the macroscale level of the continuum. Micromechanical approach on the other hand is related to variables associated at the atomic, molecular or crystalline levels. The variables are discrete quantities and their continuum quantities can be defined by means of homogenisation techniques.

### **3.5 Anisotropic finite single crystal plasticity**

The isotropic hypothesis provides a good approximation for a wide range of cases. When a polycrystalline metal is subjected to a finite inelastic straining the deformation is rarely isotropic [54].

The physics of single crystal plasticity is well established, since the discovery of diffraction x-rays by metallic crystals by Von Laue in 1912, which showed that metals were composed of atoms in specific lattices [56].

Plastic deformation in metals usually occurs by the sliding of blocks of the crystal over defined crystallographic slip planes. The initiation of slip on a slip plane is due to the shear stress component resolved on to the slip plane and is referred to as Schmid’s Law [57].

Crystal plasticity simulations using a finite element framework were initially introduced by Peirce et al. [58], Asaro [59], and Needleman et al. [60]. Crystal

plasticity has since then become widely accepted due to the desire to simulate metallurgical processes. These processes include dislocation, shear band formation, mechanical twinning, super plastic grain boundary shear, diffusion mechanisms, solid state phase transformations, recrystallisation, damage, void growth and more [54], [61]–[66]. Computational plasticity allows for more information to be gained at the microscale compared to other techniques, and allows metallurgists to gain a microstructural design and optimisation tool to develop new and better suited alloys and products.

### 3.5.1 General single crystal plasticity

This model is created from the framework of the hyperelastic based multiplicative plasticity. This allows for the deformation gradient tensor to be split into elastic and plastic components. The plastic deformation gradient measures the microscopic sliding along the crystallographic slip planes, whereas the elastic deformation gradient provides the measure of the lattice distortion. The multiplicative split is visualised in Figure 3.4.

The plastic component of the deformation gradient tensor is calculated by the following equation:

$$\mathbf{F}^p = \mathbf{I} + \gamma \mathbf{s} \otimes \mathbf{m} \quad (3.45)$$

Where  $\gamma$  is the magnitude of plastic slip and where  $\mathbf{s}$  and  $\mathbf{m}$  are the unit vectors in the slip direction and the unit normal vector to the slip plane respectively.

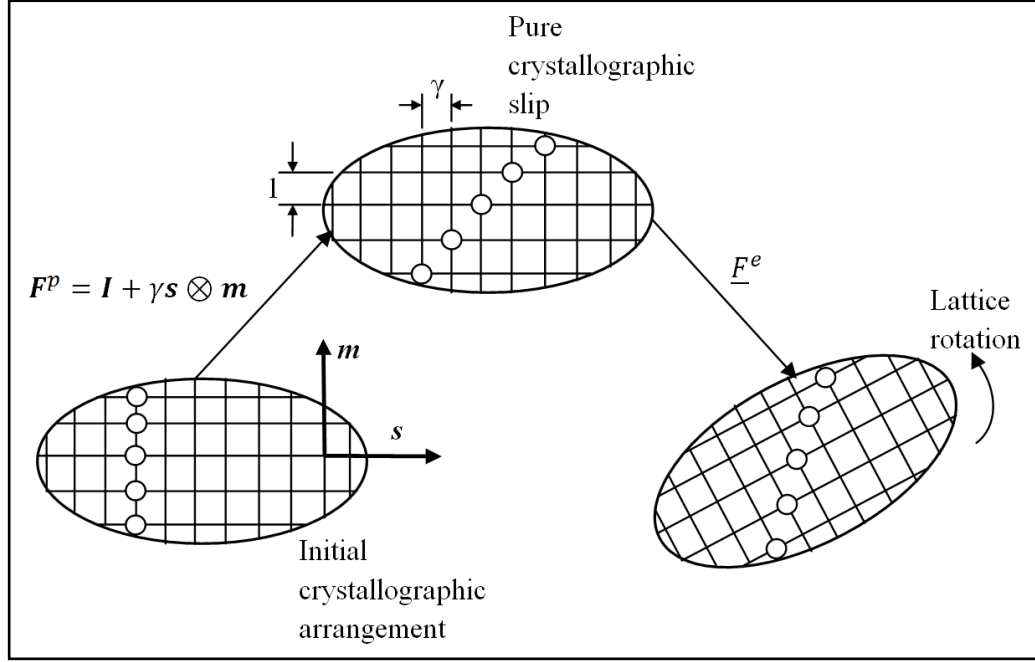


**Figure 3.4:** Multiplicative decomposition of the deformation gradient [54].

In a single slip system scenario the evolution of the plastic deformation gradient is defined by the equation

$$\mathbf{L}^p = \dot{F}^p F^{p-1}. \quad (3.46)$$

In this research slip in the crystal is likely to occur on several systems at the same time, therefore, the above equation can be rewritten in a general form for any number of active slip systems  $n_{act}$  [54] as

$$\mathbf{L}^p = \sum_{\alpha=1}^{n_{act}} \dot{\gamma}^{\alpha} \mathbf{s}^{\alpha} \otimes \mathbf{m}^{\alpha}. \quad (3.47)$$

Where  $s^{\alpha}$  and  $m^{\alpha}$  are the unit vectors that define the slip system  $\alpha$  and the multiplier  $\dot{\gamma}^{\alpha}$  is the plastic shear rate in system  $\alpha$ . For accurate prediction of the problem it is key to know when a slip system becomes active. This is achieved through knowing the critical resolved shear stress of the slip system, which can be determined through experimentation [20], [37], [38]. In simulation the Kirchhoff stress tensor  $\boldsymbol{\tau}$  can be used to define when a slip system has reached the critical stress state. The resolved shear stress on a slip system  $\alpha$  is calculated with the following formula [54].

$$\boldsymbol{\tau}^\alpha \equiv \mathbf{R}^{eT} \boldsymbol{\tau} \mathbf{R}^e : \mathbf{s}^\alpha \otimes \mathbf{m}^\alpha. \quad (3.48)$$

### 3.6 Finite element in nonlinear solid mechanics

In this subsection a brief outline of the finite element method is shown. For a more in-depth look at the finite element method the works of Belytschko et al. [67] and Zienkiewicz et al. [68] are recommended.

The constitutive initial value problem is defined when the constitutive model is inserted into the equilibrium equations. Once this is done a numerical approximation method is used to solve the problem.

To construct the finite element solution two numerical approximations are needed. The first of these approximations is a time discretisation of the underlying constitutive initial value problem. This means solving the initial value problem defined by the constitutive equations. The second approximation is a finite element discretisation. This is a finite element approximation of the virtual work statement where the domain of the body and associated functional sets are replaced with finite-dimensional counterparts generated by finite element interpolation functions.

In large strain cases the incremental boundary value problem that has to be solved can be expressed as [54]:

$$\int_{\varphi_{n+1}(\Omega)} [\widehat{\boldsymbol{\sigma}}(\boldsymbol{\alpha}_n, \mathbf{F}_{n+1}) : \nabla_x^s \boldsymbol{\eta} - \mathbf{b}_{n+1} \cdot \boldsymbol{\eta}] dv - \int_{\varphi_{n+1}(\partial\Omega_t)} \mathbf{t}_{n+1} \cdot \boldsymbol{\eta} da. \quad (3.49)$$

The discrete model of the above equation relies on finding a kinematically admissible global displacement vector  $\mathbf{u}_{n+1}$  that satisfies the standard incremental equation [54]

$$\mathbf{r}(\mathbf{u}_{n+1}) \equiv \mathbf{f}^{int}(\mathbf{u}_{n+1}) - \mathbf{f}_{n+1}^{ext} = \mathbf{0}. \quad (3.50)$$

With the external and internal force vectors being defined as:

$$\mathbf{f}_{(e)}^{int} = \int_{\varphi_{n+1}(\Omega^{(e)})} \mathbf{B}^T \widehat{\boldsymbol{\sigma}}(\boldsymbol{\alpha}_n, \mathbf{F}(\mathbf{u}_{n+1})) dv, \quad (3.51)$$

$$\mathbf{f}_{(e)}^{ext} = \int_{\varphi_{n+1}(\Omega^{(e)})} \mathbf{N}^T \mathbf{b}_{n+1} dv + \int_{\varphi_{n+1}(\partial\Omega_t^{(e)})} \mathbf{N}^T \mathbf{t}_{n+1} da. \quad (3.52)$$

Where  $\mathbf{B}$  is the spatial discrete symmetric gradient operator and  $\mathbf{N}$  is the interpolation matrix [54].

### 3.7 Homogenised deformation gradient

The homogenised deformation gradient  $\mathbf{F}$  is defined as the starting point of the kinematical variation formulation of large strain multi-scale models. This homogenised deformation gradient is the volume average of the microscopic deformation gradient field,  $\mathbf{F}_\mu$ , over the RVE [69], defined as:

$$\mathbf{F}(x, t) = \frac{1}{V_\mu} \int_{\Omega_\mu} [I + \nabla u_\mu(y, t)] dV. \quad (3.53)$$

Where  $\Omega_\mu$  denotes the reference configuration of the RVE domain and  $V_\mu$  is the volume of the RVE in the reference configuration.

### 3.8 Minimum and actual RVE kinematical constraints

From section 3.7 it is implicated that only microscopic displacement fields that satisfy the homogenised deformation fields and the homogenised deformation gradient can be permitted. If a displacement fluctuation is introduced into the microscopic domain  $\tilde{u}_\mu$ , the microscopic deformation gradient can be decomposed into [69]

$$\mathbf{F}_\mu \equiv \mathbf{F} + \nabla \tilde{u}_\mu. \quad (3.54)$$

If any further constraints are to be placed upon the kinematics of the RVE, they must be such that the actual set of kinematically admissible displacement fluctuations [69]

$$\tilde{\mathcal{K}}_\mu \subset \tilde{\mathcal{K}}_\mu^*. \quad (3.55)$$

Is a subspace of

$$\tilde{\mathcal{K}}_\mu^* \equiv \left\{ \mathcal{V} \text{ sufficiently regular} \mid \int_{\delta\Omega_\mu} \mathcal{V} \otimes \eta dA = 0 \right\}. \quad (3.56)$$

Where  $\mathcal{V}$  is the vector field and  $\tilde{u}_\mu \in \tilde{\mathcal{K}}_\mu^*$  is the minimally constrained vector space of kinematically admissible fluctuations of the RVE [69].



### 3.9 Equilibrium of RVE

The equilibrium of the RVE must be maintained throughout the whole history of the deformation gradient. This equilibrium is stated through the principle of virtual work which, when taken in the reference configuration, provides the variational equation

$$\begin{aligned} \int_{\Omega_\mu^e} \mathbf{P}_\mu(\mathbf{y}, t) : \nabla \eta \, d\mathbf{v} - \int_{\Omega_\mu^e} \mathbf{b}_{\text{ref}}(\mathbf{y}, t) \cdot \eta \, d\mathbf{v} - \int_{\partial\Omega_\mu} \mathbf{t}_{\text{ref}}^e(\mathbf{y}, t) \cdot \eta \, dA \\ - \int_{\partial\Omega_\mu^v} \mathbf{t}_{\text{ref}}^v(\mathbf{y}, t) \cdot \eta \, dA = 0 \quad \forall \eta \in \mathcal{V}_\mu. \end{aligned} \quad (3.57)$$

Where  $\mathbf{P}_\mu$  is the microscopic First Piola-Kirchhoff stress, and  $\mathbf{b}_{\text{ref}}$ ,  $\mathbf{t}_{\text{ref}}^e$ , and  $\mathbf{t}_{\text{ref}}^v$  are the external and internal surface tractions measured per unit reference area respectively [70]. It should be noted that all the above integrals are conducted over the reference configuration of their respective domains. When the differential form of the field  $\mathbf{P}_\mu$  is sufficiently regular, the corresponding equilibrium equations are

$$\begin{cases} \text{div } \mathbf{P}_\mu(\mathbf{y}, t) = \mathbf{b}_{\text{ref}}(\mathbf{y}, t) \quad \forall \mathbf{y} \in \Omega_\mu^s, \\ \text{div } \mathbf{P}_\mu(\mathbf{y}, t) = \mathbf{b}_{\text{ref}}(\mathbf{y}, t) \quad \forall \mathbf{y} \in \Omega_\mu^v, \\ \mathbf{P}_\mu(\mathbf{y}, t) \mathbf{n} = \mathbf{t}_{\text{ref}}^e(\mathbf{y}, t) \quad \forall \mathbf{y} \in \partial\Omega_\mu, \\ \llbracket \mathbf{P}_\mu(\mathbf{y}, t) \mathbf{n} \rrbracket = 0 \quad \forall \mathbf{y} \in \partial\Omega_\mu^v. \end{cases} \quad (3.58)$$

Where  $\text{div}(\cdot)$  is the material divergence of  $(\cdot)$  with respect to the reference coordinates of the RVE [70].

### 3.10 Average of the First Piola-Kirchhoff stress

The macroscopic First Piola-Kirchhoff stress is crucial to the formulation of large strain multi-scale constitutive models and is defined as equation (3.59) [69].

$$\mathbf{P} = \frac{1}{V_\mu} \int_{\Omega_\mu} \mathbf{P}_\mu \, dV. \quad (3.59)$$

If this is then written in the spatial RVE configuration, the macroscopic stress tensor reads

$$\boldsymbol{\sigma} \equiv \frac{1}{V_\mu} \int_{\varphi(\Omega_\mu)} \boldsymbol{\sigma}_\mu \, dV. \quad (3.60)$$

Where  $\boldsymbol{\sigma}_\mu \equiv (\det \mathbf{F}_\mu)^{-1} \mathbf{P}_\mu \mathbf{F}_\mu^T$ . de Souza Neto and Feijoo [70] show that macroscopic Cauchy stress differs from the spatial volume averaging of the microscopic Cauchy stress in general.

### 3.11 The Hill-Mandel principle of macrohomogeneity

Another important consideration is the Hill-Mandel principle of macrohomogeneity [71]. This principle states that the macroscopic stress power is equal to the volume average of the microscopic stress power over the RVE. In a large strain setting it can be written such that [69]

$$\mathbf{P} : \dot{\mathbf{F}} \equiv \frac{1}{V_\mu} \int_{\Omega_\mu} \mathbf{P}_\mu : \dot{\mathbf{F}}_\mu dV. \quad (3.61)$$

### 3.12 The choice of kinematical constraints

So that the RVE equilibrium is well posed, a suitable space of kinematically admissible displacement fluctuations is needed. Different macroscopic response functionals are obtained through different choices [72], which include:

- i) Linear boundary displacement model

$$\mathcal{Z}_\mu = \text{lin } \mathcal{Z}_\mu \equiv \{ \mathcal{Z} \text{ sufficiently regular} \mid \mathcal{Z}(\mathbf{y}) = 0 \ \forall \mathbf{y} \in \partial\Omega_\mu \}. \quad (3.62)$$

The full prescription of the displacement of the boundary of the RVE are given by

$$u_\mu(\mathbf{y}) = \boldsymbol{\varepsilon} \mathbf{y} \ \forall \mathbf{y} \in \partial\Omega_\mu. \quad (3.63)$$

The reaction to the prescribed boundary displacements of the RVE yield the boundary surface traction field:

$$b(\mathbf{y}) = 0 \ \forall \mathbf{y} \in \Omega_\mu. \quad (3.64)$$

- ii) Periodic boundary fluctuations

This assumption is usually used for a media with a periodic microstructure, where the macrostructure is generated by the periodic repetition of the RVE. To clearly represent this model imagine a square RVE. Each pair  $i$  of sides has equally sized subsets.

$$\Gamma_i^+ \text{ and } \Gamma_i^-, \quad (3.65)$$

Of  $\partial\Omega_\mu$  with respective unit normals

$$n_i^+ \text{ and } n_i^-. \quad (3.66)$$

A one-to-one relationship exists between the equally sized subsets, such that each point  $y^+ \in \Gamma_i^+$  has a respective pair of  $y^- \in \Gamma_i^-$

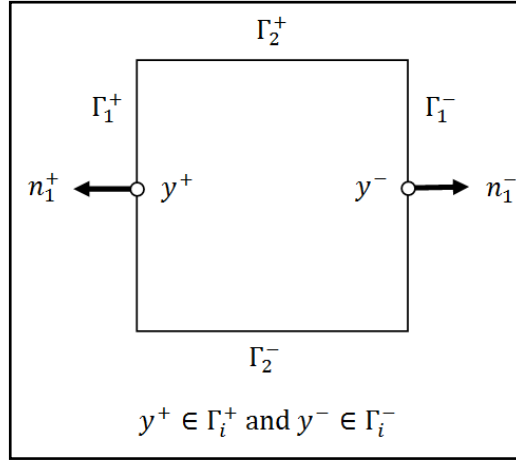


**Figure 3.5:** Periodic RVE boundary displacement function.

iii) Uniform boundary traction model

The uniform boundary traction model is the minimum kinematical constraint for the RVE.

$$\mathcal{V}_\mu = \text{uni } \mathcal{V}_\mu \equiv \mathcal{K}_\mu^*. \quad (3.67)$$

The above three models have different kinematical constraint definitions. The different model constraints give different results which can be seen as the limits of the stiffness response, with  $\text{lin } \mathcal{V}_\mu$  being the stiffest response and  $\text{uni } \mathcal{V}_\mu$  being the softest.

### 3.13 Finite strain macroscopic stress tensor

For the reference configuration of the RVE the finite strain microscopic equilibrium problem is [70]

$$\begin{aligned} {}_{trg}G(\mathbf{F}, \tilde{\mathbf{u}}_\mu, \boldsymbol{\eta}) &\equiv \int_{\Omega_\mu^s} \mathfrak{B}_y \left\{ [\mathbf{F}(x, t) + \nabla \tilde{\mathbf{u}}_\mu(y, t)]^t \right\} : \nabla \boldsymbol{\eta} dv \\ &- \int_{\partial \Omega_\mu^v} \mathbf{t}_{\text{ref}}^v(\mathbf{y}, t) \cdot \boldsymbol{\eta} dA. \end{aligned} \quad (3.68)$$

Where the large strain virtual work functional is  ${}_{trg}G$ . By choosing an appropriate space  $\mathcal{V}_\mu \subset {}_{trg}\mathcal{X}_\mu^*$  which poses the equilibrium problem well, the definition of the multi-scale model is complete.

Once the solution to  $\tilde{\mathbf{u}}_\mu$  is known the macroscopic Piola-Kirchhoff stress  $\mathbf{P}$  is [70]

$$\mathbf{P} = \frac{1}{V_\mu} \int_{\Omega_\mu^s} \mathfrak{B}_y \left[ (\mathbf{F} + \nabla \tilde{\mathbf{u}}_\mu)^t \right] dV. \quad (3.69)$$

And represents the solution to the finite element strain of the RVE equilibrium problem followed by volume averaging of the microscopic stress field.

### 3.14 Computational homogenisation finite element discretisation

The solution to the generally non-linear problem of the RVE equilibrium can be solved by the use of the Newton-Raphson scheme, with an iteration ( $k$ ) which consists of solving the linearised form [72],

$$[\mathbf{F}^{(k-1)} + \mathbf{K}^{(k-1)} \delta \tilde{\mathbf{u}}_\mu^{(k)}] \cdot \boldsymbol{\eta} = 0 \quad \forall \boldsymbol{\eta} \in \mathcal{V}_\mu^h. \quad (3.70)$$

For ease of notation the time station subscript has been omitted from the above equation. When  $\delta \tilde{\mathbf{u}}_\mu^{(k)}$  is known then a new guess  $\tilde{\mathbf{u}}_\mu^{(k)}$  for the displacement fluctuation at a time step of  $t_{n+1}$  is found through the use of the Newton-Raphson update formula

$$\tilde{\mathbf{u}}_\mu^{(k)} = \tilde{\mathbf{u}}_\mu^{(k-1)} + \delta \tilde{\mathbf{u}}_\mu^{(k)}. \quad (3.71)$$

Again the  $n + 1$  subscript has been omitted [72].

In this method the finite element method used for solving the RVE equilibrium equation is similar to that of a conventional quasi-static boundary value problem.

The difference comes from the definition of the kinematical constraints acting on the RVE,  $\boldsymbol{\eta}$ , which are yet to be defined.  $\boldsymbol{\eta}$  is divided into corresponding sets of degrees of freedom that act upon the boundary of the RVE. For a more in-depth explanation of partitions of  $\boldsymbol{\eta}$  the publication by Peric et al. [72] is advised.

Therefore, for the uniform traction constraint, the vectors  $\boldsymbol{\eta}$ ,  $\mathbf{f}$ ,  $\mathbf{K}_T$ , and  $\delta\tilde{\mathbf{u}}$  are split into free (f), independent (i) and dependent (d) degrees of freedom [72].

$$\left\{ \begin{bmatrix} \mathbf{f}_i^{int} \\ \mathbf{f}_f^{int} \\ \mathbf{f}_d^{int} \end{bmatrix}^{(k-1)} + \begin{bmatrix} \mathbf{K}_{ii} & \mathbf{K}_{if} & \mathbf{K}_{id} \\ \mathbf{K}_{fi} & \mathbf{K}_{ff} & \mathbf{K}_{fd} \\ \mathbf{K}_{di} & \mathbf{K}_{df} & \mathbf{K}_{dd} \end{bmatrix}^{(k-1)} \begin{bmatrix} \delta\tilde{\mathbf{u}}_i \\ \delta\tilde{\mathbf{u}}_f \\ \delta\tilde{\mathbf{u}}_d \end{bmatrix}^{(k)} \right\} \cdot \begin{bmatrix} \boldsymbol{\eta}_i \\ \boldsymbol{\eta}_f \\ \boldsymbol{\eta}_d \end{bmatrix} = 0 \quad \forall \boldsymbol{\eta}_i, \boldsymbol{\eta}_f, \boldsymbol{\eta}_d. \quad (3.72)$$

For the periodic boundary displacement fluctuations model, the RVE geometry must comply with the imposed constraints as laid out in part (ii) of Section 3.12. For this model it is useful to assume that each boundary node  $i^+$ , with associated coordinates  $y_i^+$ , has a pair  $i^-$ , which has coordinates  $y_i^-$ . Knowing this, the nodal displacement fluctuation vectors housed inside the kinematically admissible discretised area can be defined as [72]

$$\mathcal{V}_\mu^h = \left\{ v = \begin{bmatrix} v_i \\ v_+ \\ v_- \end{bmatrix} \mid v_+ = v_- \right\}. \quad (3.73)$$

Where  $v_i$ ,  $v_+$  and  $v_-$  denote the vectors containing, respectively, the degrees of freedom of the RVE interior and the portions  $\Gamma_+$  and  $\Gamma_-$  of the boundary. As before the vectors  $\boldsymbol{\eta}$ ,  $\mathbf{F}$ ,  $\mathbf{K}_T$ , and  $\delta\tilde{\mathbf{u}}$  are split such that [72]

$$\left\{ \begin{bmatrix} \mathbf{F}_i \\ \mathbf{F}_+ \\ \mathbf{F}_- \end{bmatrix}^{(k-1)} + \begin{bmatrix} \mathbf{K}_{ii} & \mathbf{K}_{i+} & \mathbf{K}_{i-} \\ \mathbf{K}_{+i} & \mathbf{K}_{++} & \mathbf{K}_{+-} \\ \mathbf{K}_{-i} & \mathbf{K}_{-+} & \mathbf{K}_{--} \end{bmatrix}^{(k-1)} \begin{bmatrix} \delta\tilde{\mathbf{u}}_i \\ \delta\tilde{\mathbf{u}}_+ \\ \delta\tilde{\mathbf{u}}_- \end{bmatrix}^{(k)} \right\} \cdot \begin{bmatrix} \boldsymbol{\eta}_i \\ \boldsymbol{\eta}_+ \\ \boldsymbol{\eta}_- \end{bmatrix} = 0 \quad \forall \boldsymbol{\eta}_i, \boldsymbol{\eta}_+, \boldsymbol{\eta}_-. \quad (3.74)$$

Due to the arbitrary nature of  $\boldsymbol{\eta}_i$ ,  $\boldsymbol{\eta}_f$ , and  $\boldsymbol{\eta}_+$  in equations (3.72) and (3.74), the linear systems of the equation for  $\delta\tilde{\mathbf{u}}^{(k)}$  can be simplified. For the linear boundary condition, discretisation is simple. The boundary nodes are identified and the virtual displacements and fluctuations' degrees of freedom are set to zero. The internal nodes' degrees of freedom are, however, unconstrained. Therefore, the boundary

conditions are described as prescribed (P) degrees of freedom and the internal nodes are described as free (f) degrees of freedom such that

$$[\mathbf{f}_f^{int}]^{(k-1)} + [\mathbf{K}_{ff}]^{(k-1)} [\delta \tilde{\mathbf{u}}_\mu]^{(k)} = 0. \quad (3.75)$$

## Chapter 4 Finite element simulation of a multiscale model

In this thesis the following hyperelastic-viscoplastic material model is used. This model is adapted from a previous two dimensional model and expanded to three dimensions. The model is also now designed to work with HCP crystal structures such as titanium alpha phase, but can also simulate the BCC crystal structure found within the beta phase. The model allows for slip on all families of slip systems, along with linear hardening. All the families of slip systems have their own material parameters which govern how and when they slip. The orientation of the grains is controlled through the use of Euler angles using the Bunge convention.

### 4.1 Material model

In this research a finite element program called HYPLAS is used. HYPLAS is an implicit finite element solver which is already capable of single crystal plasticity simulations. This provided a solid foundation from which to build this project.

HYPLAS provides the deformation gradient to the material subroutine.

Based on the kinematic assumption of the multiplicative split of the deformation gradient into the elastic deformation gradient ( $\mathbf{F}^e$ ), and the plastic deformation gradient ( $\mathbf{F}^p$ ), equation (4.1) is obtained. The plastic deformation gradient is the continuum measure of the slip along the crystallographic slip-systems for a given crystal. The elastic deformation gradient measures distortion of the crystal lattice as well as rigid body rotations with respect to the initial configuration of the lattice. In metals the distortion of the crystal lattice is typically infinitesimal [54].

$$\mathbf{F} = \mathbf{F}^e \mathbf{F}^p. \quad (4.1)$$

A hyperelastic law is used within the model to govern the reversible behaviour. The stresses are found through the use of the hyperelastic potential ( $\mathbf{F}^e$ ). The Kirchhoff stress tensor as a function of the elastic deformation gradient is given by [54]:

$$\boldsymbol{\tau}(\mathbf{F}^e) = \frac{dW}{d\mathbf{F}^e} \mathbf{F}^{eT}. \quad (4.2)$$

A compressible neo-Hookean model is used to describe the elastic behaviour, which gives the potential seen in equation (4.3). The use of compressible neo-Hookean

material in single crystal plasticity leads to a simple format of the return mapping equations and was originally proposed by Miehe [73], [74].

$$W(\mathbf{B}_{iso}^e) \equiv \frac{1}{2} G(\text{tr}[\mathbf{B}_{iso}^e] - 3) + \frac{1}{2} K(\ln J^e)^2. \quad (4.3)$$

Where  $G$  and  $K$  are shear and bulk modulus respectively and  $\mathbf{B}_{iso}^e$  is the isochoric component of the elastic left Cauchy-Green strain tensor  $\mathbf{B}^e$ :

$$\mathbf{B}_{iso}^e \equiv \mathbf{F}_{iso}^e (\mathbf{F}_{iso}^e)^T = (J^e)^{\frac{-2}{3}} \mathbf{B}^e. \quad (4.4)$$

Where  $J^e$  is the determinant of  $\mathbf{F}^e$ , and  $\mathbf{F}_{iso}^e$  is the isochoric component of the elastic deformation gradient:

$$\mathbf{F}_{iso}^e \equiv (J^e)^{\frac{-1}{3}} \mathbf{F}^e. \quad (4.5)$$

The Kirchhoff stress can then be written from the potential seen in equation (4.3) as:

$$\boldsymbol{\tau} \equiv G \text{dev}[\mathbf{B}_{iso}^e] + K(\ln J^e) \mathbf{I}. \quad (4.6)$$

Due to metal crystals' lattices having small elastic distortions, use of a different elastic law will have little effect upon results of numerical simulations. As such, the use of the neo-Hookean model will result in the formulation of relatively simple return mapping equations. The elastic model used is for numerical convenience, rather than being grounded in the intricate physics of the elastic deformation of the crystal.

#### 4.1.1 Multi-surface plasticity

To formulate a yield criterion for single crystal plasticity with a multi-surface definition, it is useful to split the physical slip system into two mirrored parts [54]:

$$\{s^\alpha, m^\alpha\} \text{ and } \{s^\beta, m^\beta\} \equiv \{-s^\alpha, m^\alpha\}. \quad (4.7)$$

This will mean the material model will have double the number of slip systems compared to the physical crystal. This makes sense as, in reality, a slip system can slip in either direction in the physical crystal, where, in the code the slip systems are defined by vectors. This means two sets of vectors (one positive set and one negative set) are needed adequately describe the full potential movement of the slip system.



This leads to defining  $2 \times$  number of systems ( $n_{syst}$ ) yield surfaces as shown in equation (4.8) [54].

$$\Phi^\alpha(\tau^\alpha, \tau_y^\alpha) \equiv \tau^\alpha - \tau_y^\alpha, \quad \alpha = 1, \dots, 2n_{syst}. \quad (4.8)$$

Where  $\tau_y^\alpha$  is the critical resolved shear stress (CRSS) for slip system alpha. If hardening is present then the CRSS value of the slip system  $\alpha$  depends on the history of the deformation. In this work a linear hardening law is adopted to govern the evolution of the CRSS value of each slip system.  $\tau^\alpha$  is the Schmid resolved shear stress in the slip system alpha [54]:

$$\tau^\alpha \equiv \mathbf{R}^{eT} \boldsymbol{\tau} \mathbf{R}^e : \mathbf{s}_0^\alpha \otimes \mathbf{m}_0^\alpha. \quad (4.9)$$

Where  $\mathbf{R}^e$  is the elastic rotations due to polar decomposition of the elastic deformation gradient.  $\mathbf{s}_0^\alpha$  is the slip system alpha vector and  $\mathbf{m}_0^\alpha$  is the unit normal vector to the slip vector. Due to using the neo-Hookean hyperelastic model, the Schmid resolved shear stress can be rewritten as [54]:

$$\tau^\alpha \equiv G \mathbf{s}^\alpha \cdot \mathbf{m}^\alpha. \quad (4.10)$$

Where  $\mathbf{s}^\alpha$  and  $\mathbf{m}^\alpha$  are the elastic push forward of  $\mathbf{s}_0^\alpha$  and  $\mathbf{m}_0^\alpha$ . Assuming an isotropic Taylor hardening law where  $\tau_y$  is a given function

$$\tau_y = \tau_y(\gamma). \quad (4.11)$$

With the accumulated slip  $\gamma$  in rate form being expressed as

$$\dot{\gamma} \equiv \sum_{\alpha}^{2n_{syst}} \dot{\gamma}^\alpha. \quad (4.12)$$

In rate form the plastic deformation gradient can be shown to be:

$$\dot{\mathbf{F}}^p \mathbf{F}^{p-1} = \sum_{\alpha}^{2n_{syst}} \dot{\gamma}^\alpha \mathbf{s}_0^\alpha \otimes \mathbf{m}_0^\alpha. \quad (4.13)$$

Where  $\dot{\gamma}^\alpha$ , the plastic multiplier, denotes the contribution of a given slip system alpha to the total rate of plastic deformation.

#### 4.1.2 Return mapping algorithm

Assuming a time interval of  $[t_n, t_{n+1}]$  and an initial value of  $\mathbf{F}_n^p$ , the differential equation seen in equation (4.13) for  $\mathbf{F}^p$  can be numerically integrated in an implicit fashion with the use of the tensor exponential function. This implicit exponential approximation to the plastic flow equation yields the following discrete form [54]:

$$\mathbf{F}_{n+1}^p = \exp \left[ \sum_{\alpha}^{2nsyst} \dot{\gamma}^\alpha \mathbf{s}_0^\alpha \otimes \mathbf{m}_0^\alpha \right] \mathbf{F}_n^p. \quad (4.14)$$

Due to the multiplicative of  $\mathbf{F}$ , the elastic deformation gradient update formula can be written as:

$$\mathbf{F}_{n+1}^e = \mathbf{F}^{e\ trial} \exp \left[ - \sum_{\alpha}^{2nsyst} \dot{\gamma}^\alpha \mathbf{s}_0^\alpha \otimes \mathbf{m}_0^\alpha \right]. \quad (4.15)$$

Where

$$\mathbf{F}^{e\ trial} = \mathbf{F}_\Delta \mathbf{F}_n^e. \quad (4.16)$$

With  $\mathbf{F}^{e\ trial}$  being the elastic trial deformation gradient and  $\mathbf{F}_\Delta$  being the incremental deformation gradient for the given time interval. The internal hardening variable  $\gamma$  is updated by the following formula.

$$\gamma_{n+1} = \gamma_n + \sum_{\alpha}^{2nsyst} \Delta\gamma^\alpha. \quad (4.17)$$

Where  $\Delta\gamma^\alpha$ , the incremental plastic multiplier.

The stress update procedure requires the solution of the following non-linear system of  $n_{act}$  algebraic equations:

$$\tilde{\Phi}^\alpha(\Delta\bar{\gamma}) = 0, \quad \alpha \in A. \quad (4.18)$$

Where  $A$  is the set of active slip system numbers and  $\Delta\bar{\gamma}$  is defined by:

$$\Delta\bar{\gamma} \equiv \{\Delta\gamma^\alpha | \alpha \in A \}. \quad (4.19)$$

#### 4.1.3 Computation of the tensor exponential

The tensor exponential function can be explicitly written in terms of its series representation [54]:

$$\exp[\mathbf{X}] = \sum_{n=0}^{n_{max}} \frac{1}{n!} \mathbf{X}^n. \quad (4.20)$$

The scalar counterpart of the above equation can be used to evaluate the tensor exponential function to any given degree of accuracy. In a finite element environment the tensor exponential can be calculated by truncating the above series [54]. This is achieved by setting  $n_{max}$  to the following:

$$\frac{1}{n_{max}!} |\mathbf{X}^{n_{max}}| \leq \epsilon_{tol}. \quad (4.21)$$

Where  $\epsilon_{tol}$  is the prescribed tolerance.

#### 4.1.4 Exponential map derivative

The Cartesian components of the derivative of the tensor exponential function at an argument  $\mathbf{X}$  have the following series representation [54]

$$[\text{Dexp}(\mathbf{X})]_{ijkl} = \sum_{n=1}^{\infty} \frac{1}{n!} \sum_{m=1}^n [\mathbf{X}^{m-1}]_{ik} [\mathbf{X}^{n-m}]_{jl}. \quad (4.22)$$

The formula above was derived by de Souza Neto and was obtained by directly differentiating the series representation of the exponential tensor function [54]. The evaluation of the tensor exponential derivative is carried in a finite element

environment by truncating the above series to the form seen in equation (4.23).

Where  $n_{max}$  satisfies the accuracy conditions shown in (4.21)

$$[\text{Dexp}(\mathbf{X})]_{ijkl} = \sum_{n=1}^{n_{max}} \frac{1}{n!} \sum_{m=1}^n [\mathbf{X}^{m-1}]_{ik} [\mathbf{X}^{n-m}]_{jk}. \quad (4.23)$$

#### 4.1.5 Perić slip rate law

As metal crystals have the ability to deform elastically and plastically, the rate of deformation can have significant effects upon the mechanics of the material. The implementation of a slip rate law with yield surfaces will therefore provide a better numerical framework to model high rate deformation cases, such as a bird strike on an aero engine fan blade. A slip rate law that is implemented into the section 4.1.2 framework is the Perić law, which is presented below [54]:

$$\dot{\gamma}^\alpha = \begin{cases} \frac{1}{\mu} \left[ \left( \frac{|\tau^\alpha|}{\tau_y} \right)^{1/\epsilon} - 1 \right] & \text{if } \Phi^\alpha(\tau^\alpha, \tau_y) \geq 0 \\ 0 & \text{if } \Phi^\alpha(\tau^\alpha, \tau_y) < 0. \end{cases} \quad (4.24)$$

The constants  $\mu$  and  $\epsilon$  are the viscosity and rate-sensitivity parameter respectively. In the absence of hardening the critical resolved shear stress ( $\tau_y$ ) is also a constant.

#### 4.1.6 Exponential map-based integration algorithm

As the model is based on a hyperelastic law which defines  $\boldsymbol{\tau}$  as a function of  $\mathbf{F}^e$ , the following can be written

$$\tau^\alpha = \tau^\alpha(\mathbf{F}^e) \text{ and } \dot{\gamma}^\alpha = \dot{\gamma}^\alpha(\mathbf{F}^e). \quad (4.25)$$

Taking the standard backward Euler discretisation of equation (4.24), the following is obtained

$$\Delta \gamma^\alpha = \Delta t \dot{\gamma}^\alpha(\mathbf{F}_{n+1}^e). \quad (4.26)$$

When equation (4.26) is substituted into equation (4.15) the following is the result:

$$\mathbf{S}(\mathbf{F}_{n+1}^e) = \mathbf{F}_{n+1}^e - \mathbf{F}_{n+1}^{e \text{ trial}} \exp \left[ -\Delta t \sum_{\alpha}^{2nsyst} \dot{\gamma}^{\alpha}(\mathbf{F}_{n+1}^e) \mathbf{s}_0^{\alpha} \otimes \mathbf{m}_0^{\alpha} \right] = 0. \quad (4.27)$$

#### 4.1.7 The local Newton-Raphson algorithm

The exact Jacobian used in the Newton-Raphson scheme for the solution of residual equation (4.27) is obtained by differentiating  $\mathbf{S}$  with respect to the equation variable  $\mathbf{F}_{n+1}^e$ . This leads to equation (4.28) in Cartesian components.

$$J_{ijkl} \equiv \left[ \frac{d\mathbf{S}}{d\mathbf{F}^e} \right] = \delta_{ik} \delta_{jl} + \Delta t \mathbf{F}_{im}^{e \text{ trial}} E_{mjpk} \left[ \sum_{\alpha=1}^{nsyst} \mathbf{s}_0^{\alpha} \otimes \mathbf{m}_0^{\alpha} \otimes \frac{d\dot{\gamma}^{\alpha}}{d\mathbf{F}^e} \right] = 0. \quad (4.28)$$

## **Chapter 5 RVE-based multiscale modelling of polycrystals**

### **5.1 RVE-based modelling**

In this research the principle of single crystal plasticity, as described in the previous chapter, is used to model the grains of the alpha and beta phases in titanium. This strategy is then coupled with the Representative Volume Elements (RVE) that are generated by the method in section 5.2.2. This means several grains of the alpha and beta phase are created and connected together to form a polycrystalline microstructure for simulation. This RVE then has a finite element discretisation applied to it and the individual grains have material properties assigned to them.

As the load is applied, the deformation of the RVE is dependent upon the response of each of the grains through the use of the single crystal plasticity equations. At the grain boundaries resistance to slip may occur due to the unfavourable orientation of the next grain. This model does not account for grain boundary slip and the grain boundaries have no explicit modelling parameters.

### **5.2 RVE generation**

RVEs are a simulated microstructure that can be used for finite element analysis. They are designed to give an accurate representation of the microstructure. This allows for the microstructural interaction to be studied when the RVE is subject to loading conditions.

In the work of Bridier [75] the lamellar alpha and beta were not explicitly modelled with alternating alpha and beta laths, since this would make the integration of an FE model with both a large number of primary grains and fine detail of colonies computationally infeasible. Bridier created a statistical volume element using a finite element mesh composed of 30 x 30 hexagonal shaped grains in the order of 20  $\mu\text{m}$  diameter. This led to a computational domain of approximately 900 grains.

In the work by Dunne [14] a model polycrystalline containing 27 grains, where the crystal orientations can be specified, is created. Dunne himself notes that this is relatively few grains to be modelling, and that the boundary effects are likely to be large in the grains close to the free surfaces. He does, however, go on to say that the

effects of the boundary on the main grain analysed are limited [14]. This supports the view that the number of grains needed to create a reliable RVE is quite large.

In the Cellular Automaton (CA) work conducted by Pourian [13], an equiaxed hexagonal close-packed microstructure was created, and represented as cells in the model. The cells in the CA model morphology were assumed to be spherical [13]. The CA technique does not capture the geometrical dependencies of the microstructure due to the nature of the method compared to other methods such as Voronoi tessellation.

Compared to the CA model morphology, Voronoi tessellation methods give more realistic microstructures of metals [75]. This is due to the 3D Voronoi producing complex random shapes rather than utilising idealised shapes such as the CA model that uses spheres [76]. The Voronoi tessellations are defined analytically. This gives the grains created straight edges and planar faces, whilst still giving a realistic microstructure that has no voids or grain overlaps [77]. The process of Voronoi tessellation is described below:

1. Assuming a finite set of points  $N$  (nuclei) positioned within a Euclidian space, the Voronoi tessellation divides the entire space into  $N$  convex polyhedra.
2. Each polyhedra generated from a nucleus  $P$  contains all the points closer to  $P$  than to any other nuclei.

The grains are then grown in a way akin to growth of metallurgical grains in real microstructures:

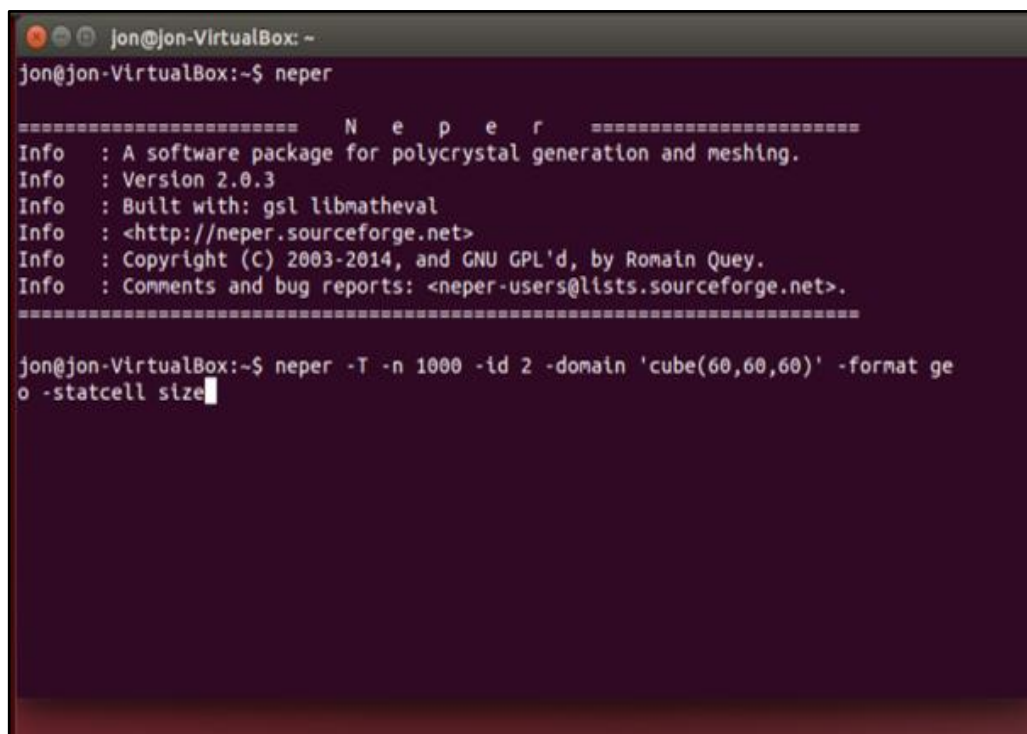
1. All nuclei are created simultaneously.
2. Original nucleation points' coordinates in the Euclidian space remain set throughout the growth process.
3. The growth of the grains is isotropic and constant.
4. Grain growth in a direction stops when it comes into contact with another grain in that direction, ensuring no voids or grain overlaps is present in the generated microstructure.

The Hardcore method adds a sphere of influence of radius  $\rho$  emulating from the nucleation point  $N$ , at the stage where the nucleation points are being placed [75]. If another nucleus falls inside the sphere then it is moved to be outside of this sphere

[75]. The advantage of using the Hardcore method is it reduces the number of small grains and produces more regular grains [75]. Due to the nature of the method the grains produced are of irregular shape and, as such, tetrahedral elements have to be used to discretise the domain [75].

### 5.2.1 NEPER

This software is open source but is only supported on the Linux operating system. The Neper program is run from the Linux terminal which can be seen in Figure 5.1. *neper -T* calls the tessellation module of the Neper program. This is the first part of the command line to be entered. *-n 1000* refers to how many grains the user wishes to have within the domain space, which is then followed by an id tag. *-domain 'cube(60,60,60)'* sets the domain of the RVE to be a cube shape of size 60 x 60 x 60. This is then followed by the *-format geo* section, which means the output file is a .geo file. This is useful to the research as this allows for GMSH software to be used to visualise the RVE structure.



```
jon@jon-VirtualBox: ~
jon@jon-VirtualBox:~$ neper

===== N e p e r =====
Info  : A software package for polycrystal generation and meshing.
Info  : Version 2.0.3
Info  : Built with: gsl libmatheval
Info  : <http://neper.sourceforge.net>
Info  : Copyright (C) 2003-2014, and GNU GPL'd, by Romain Quey.
Info  : Comments and bug reports: <neper-users@lists.sourceforge.net>.
=====

jon@jon-VirtualBox:~$ neper -T -n 1000 -id 2 -domain 'cube(60,60,60)' -format geo
o -statcell size
```

Figure 5.1: Neper terminal.

The last section of the command line, *-statcell size*, creates a text file with the statistics of the grain sizes that have been produced to create the RVE. It allows the



user to analyse the RVE that has been created, and relate it back to the EBSD data, to make sure the virtual grain structure resembles the physical grain structure seen in the EBSD map.

### 5.2.1.1 Laguerre tessellation

The weighting system in Neper uses the Laguerre tessellation [78], [79]. This tessellation system gives bigger spheres of influence to the higher weighted grains, but all grains grow at the same rate. In this form of tessellation the seed point for the grain does not need to be in the grain it generates and some seed points can produce no grain if they are surrounded by much higher weighted seed points. This can be seen in Figure 5.2 with  $W$  being the weight assigned to the seed point.

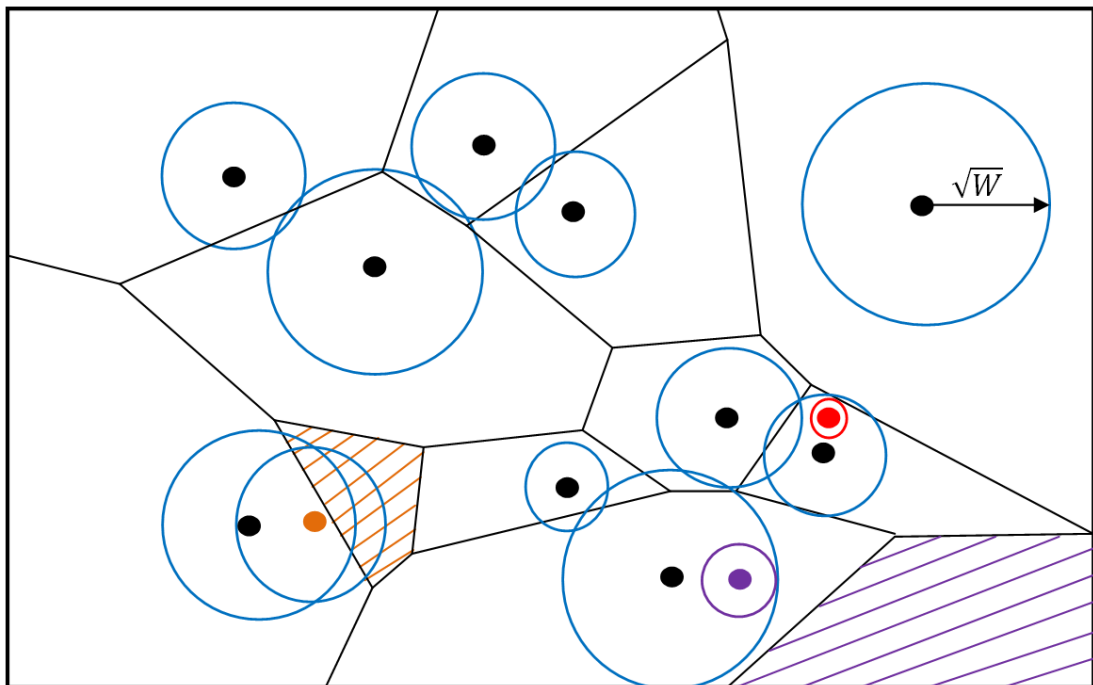


**Figure 5.2:** Laguerre tessellation diagram [79].

As can be seen, the purple seed point generates the purple grain, yet it is not contained within the final grain shape. It can also be seen that the red seed point is swamped by the other seed points around it and, therefore, does not generate a grain in the final tessellation.

### 5.2.1.2 Voronoi tessellation

Another method used by Neper is the Voronoi tessellation. Like the Laguerre tessellation the domain is populated by seed points, however, unlike the Laguerre tessellation, the seeds that generate the grains are contained in the grains as there is no weighting function. This can be seen in Figure 5.3, where the black dots represent the seed point for each grain.

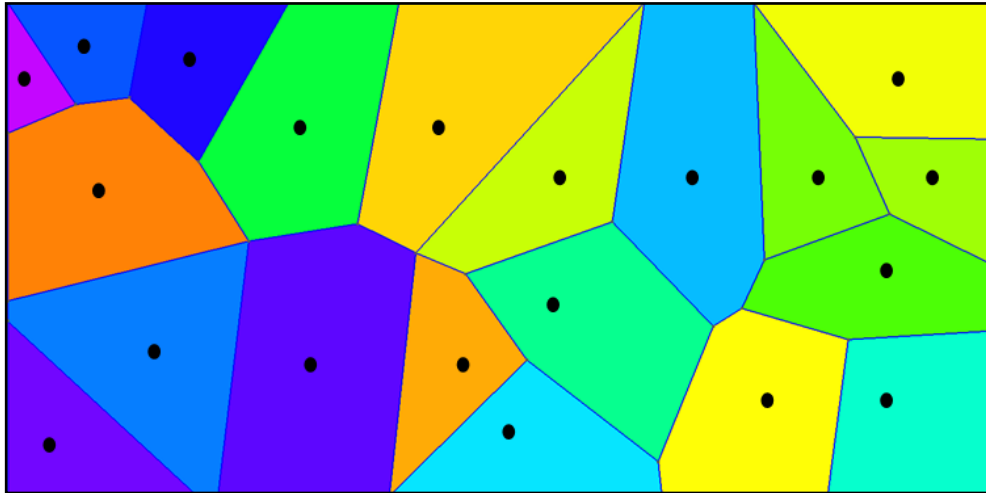


Figure 5.3: Voronoi tessellation diagram [79].

All the grains grow from their seed point at the same rate and stop when they come into contact with another grain. This means this method does not normally lend itself to dual phase microstructures which have two phases at different sizes.

However, Neper allows the user to specify the location of the seed points. This function has been used in this research, coupled with the Voronoi tessellation described above.

### 5.2.2 Coupled MATLAB and Neper RVE generation

In this research a MATLAB code has been created to generate the seed points input for Neper. This code, however, places the seed points in such a way that allows for two distinct sizes of grains to be produced. This is necessary to create a realistic model, as in titanium the alpha phase and the beta phase are two distinct sizes, with the alpha phase volume on average being 260 times that of the beta phase.

A number of alpha-beta configurations were trialled to create an RVE with a volume fraction close to that of the EBSD data. In the final chosen configuration a fifth of the total desired beta seed points are randomly distributed throughout the domain. The

MATLAB code then checks to see if any of the initial beta seed points are in violation of the distance condition set between them and redistributes any offending seed points. This ensures an even distribution throughout the RVE. The MATLAB code also checks to make sure that no seed point is placed too close to the outer bounds of the domain, as this could result in other seed points being placed outside of the domain in the next step. Once these initial beta seed points have been placed an additional 4 beta seeds are placed around each of the initial beta seed points. These new beta seeds are placed in set positions in relation to the initial beta seed. After the beta points have been placed, 12 alpha seed points for each of the initial beta seeds is placed. The placement of these seed points is such that the beta grain growth is constricted by the alpha seed points. As the beta grains are smaller than the alpha grains, they need to be constricted due to the equal growth rate of all seed points in a Voronoi tessellation. If they were not constricted this would lead to both alpha and beta grains having a similar average volume, a result that is not representative of a real life grain structure.

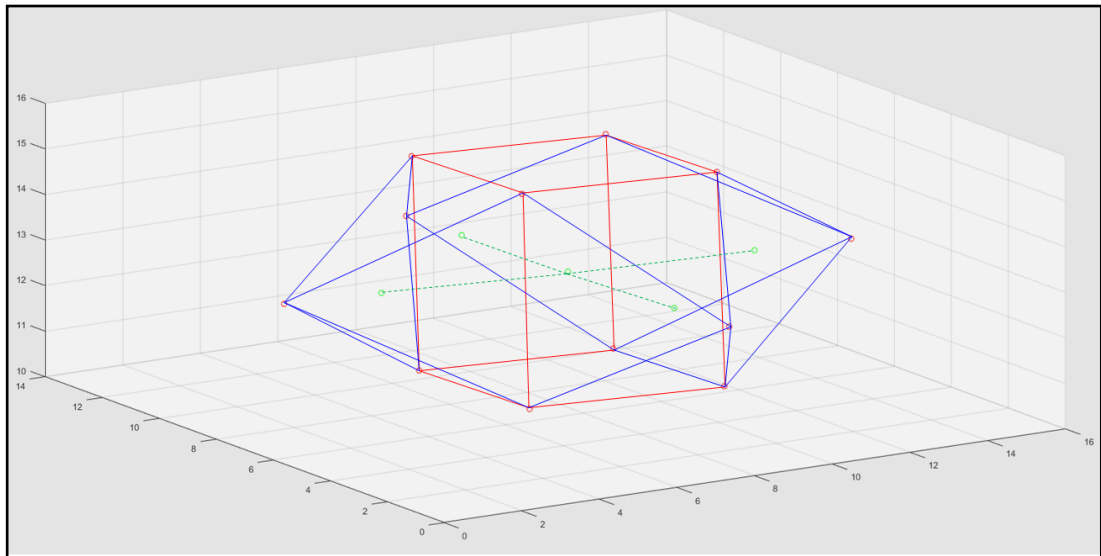


**Figure 5.4:** MATLAB code seed points. Green and red circles represent beta and alpha seed point respectively.

In Figure 5.4 the green circles are the beta seed points. These beta seed points are all on the same Z axis, as can be seen by the green dashed lines connecting them. The alpha seed points are the red circles in the diagram. Eight of the alpha seed points form a cube around the central initial beta seed as seen by the red lines. Four more

alpha seeds are then placed to form square based pyramids around the remaining beta seeds as shown by the blue lines.

This method of placing the seed points allows you to track the phase type of each grain. Grains 1 to n are the beta grains, where n is the number of beta grains, and n+1 to m are the alpha grains, where m is the total number of grains within the RVE.

This seed point file is passed to Neper, which generates the Voronoi tessellation in three dimensions, and regularisation upon the tessellation takes place to eliminate any small edges.

### **5.2.3 Trimming the EBSD data**

For this work EBSD maps and data have been provided by Timet UK Ltd. From the raw data any readings that were under two step sizes were removed, as this is believed to be erroneous data due to poor recognition of the Kikuchi band [80]. Once these data points had been trimmed from the data the average grain radiuses of the alpha and beta phases were calculated as 5.75  $\mu\text{m}$  and 0.90  $\mu\text{m}$  respectively. From the calculated averages the MATLAB code could be used to generate the seed points, such that the grain volumes would match closely to the EBSD data set.

### **5.2.4 RVE generated from EBSD data**

Using EBSD data, a RVE can be generated that closely matches the volume fraction of Ti-6Al-4V. EBSD data showed the average volume of alpha and beta grains to be 794  $\mu\text{m}^3$  and 3.07  $\mu\text{m}^3$  respectively and at room temperature the beta volume fraction in Ti-6Al-4V is approximately 3-4% [81]. The volume fraction of the alloy needs to be preserved over other considerations due to the deformation of the two phase alloy being dependent on the volume fraction of both phases [21]. Therefore, a volume fraction of 3-4% will be prioritised over matching the average grain volumes of the phases for this project.

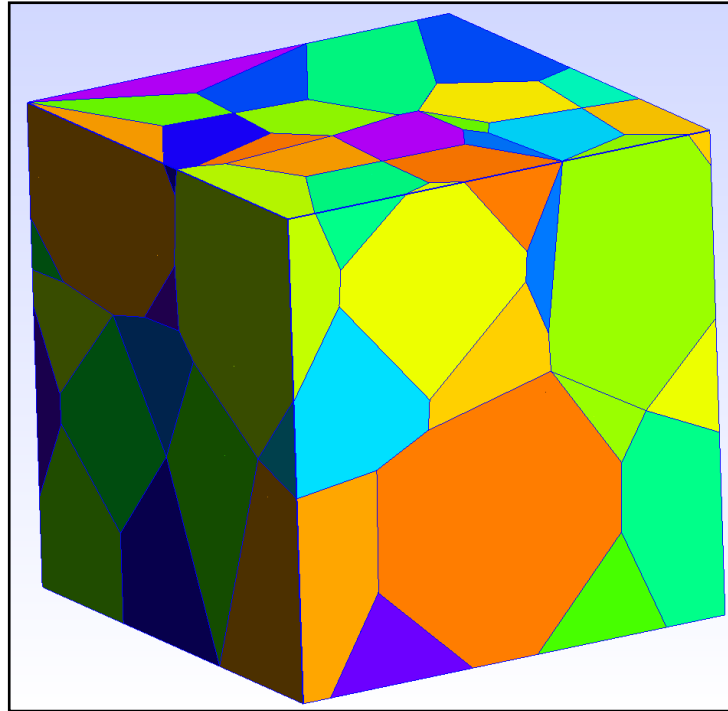


**Figure 5.5:** 102 Grain RVE created in GMSH from EBSD data.

The internal grain structure of the RVE (Figure 5.6) has no voids and has realistic grain geometries, demonstrating the advantage of the Voronoi technique.

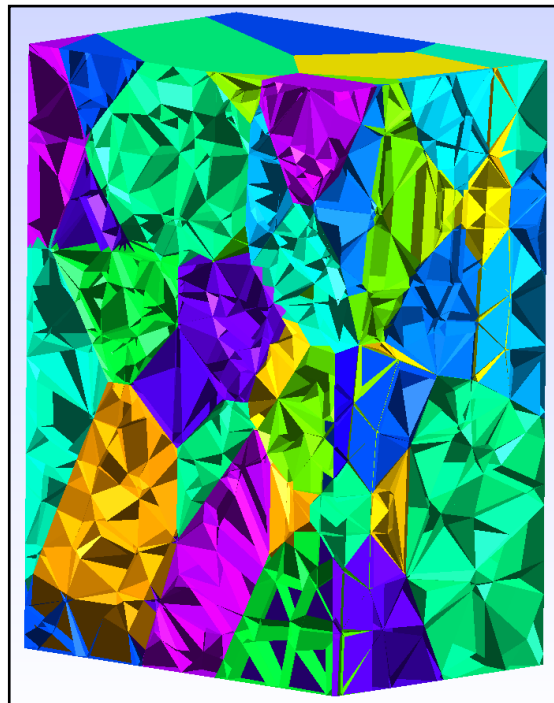


**Figure 5.6:** Cross section view of RVE in GMSH, showing realistic geometries achieved by the voronoi method.

This method of generating RVEs will allow for the study of volume fraction effect as well as grain distribution and texture. The RVE is meshed by Neper using hexahedral elements. This does affect the shape of the grains, giving them a more blocky appearance compared to the original Voronoi generated grains. The computational benefits of using the eight-noded brick elements over tetrahedral elements, however, far outweighs the loss in complex geometries.

## Chapter 6 Simulations of Titanium-6AL-4V

In this research improvements to the HYPLAS 3D code have been made that allow for the simulation of HCP crystal in a hyperelastic-viscoplastic single crystal routine. The ability to define different families of slip systems has been added to all crystal types used in HYPLAS. The user can define as many slip families as they require with as many slip systems in each family. This allows for full customisation of the material properties, allowing the user to construct what they need. Each family of slip systems can have its own CRSS value and hardening curve associated with it. This can allow for the different slip systems to yield and harden according to their own parameters. Each family can also have its own rate sensitivity parameters, allowing for different rate effects on each family.

Several MATLAB codes have been written to aid in the construction of the HYPLAS inform files. These MATLAB files include the creation of the hardening data as explained in section 6.2.1 and a MATLAB code, HYPLAS INPUT to create the inform file necessary to provide HYPLAS with the information needed to run. HYPLAS INPUT reads in the nodes and elements from the mesh along with the hardening data from the created HARDENING code. For this research the material parameters for the alpha and beta phase have been hard coded into HYPLAS INPUT. The MATLAB code also asks the user to specify the number of beta grains and total number of grains, along with the desired number of increments and simulation time. Figure 6.1 shows the process required to go from RVE creation to simulation results.

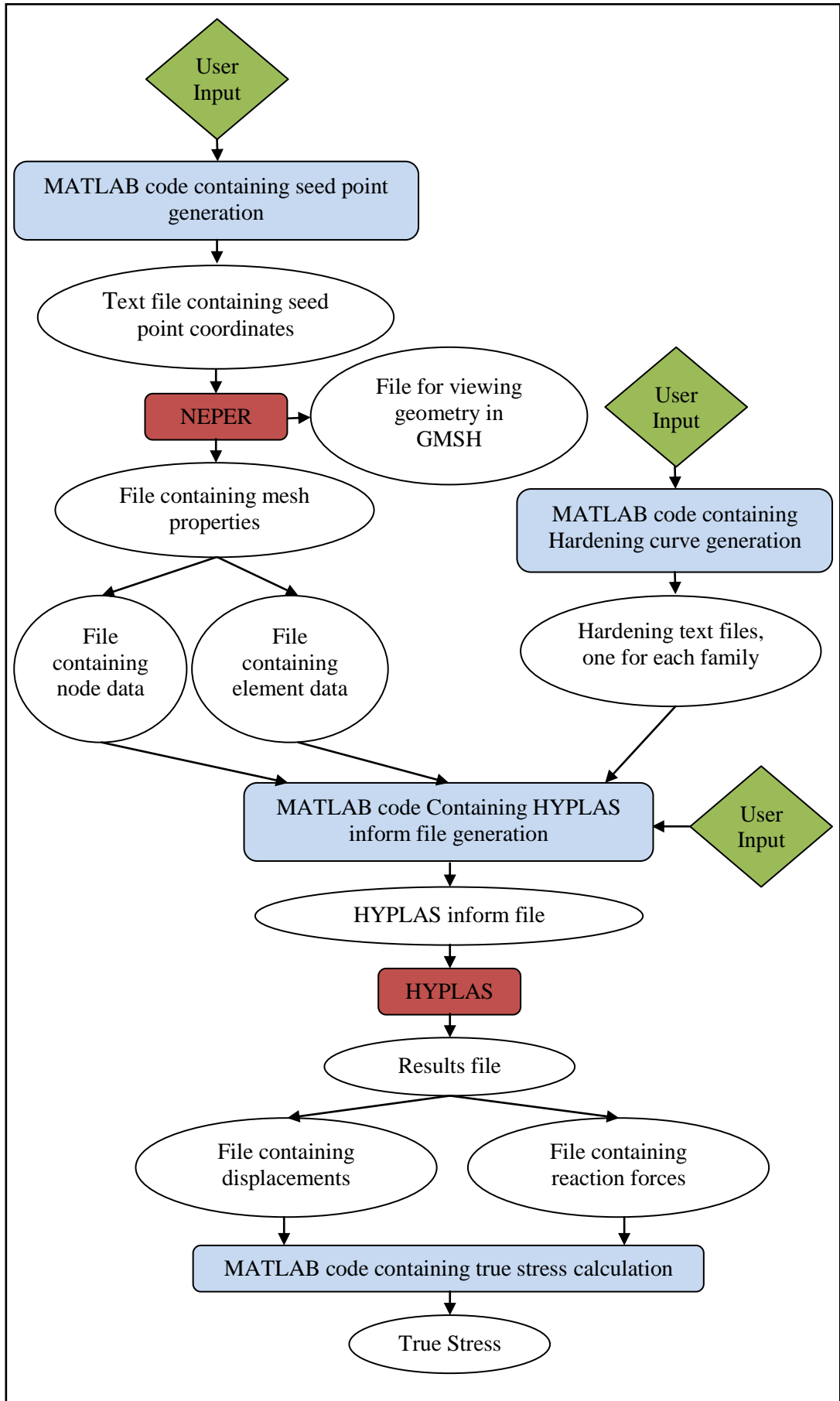


**Figure 6.1:** Process of RVE simulation, from RVE generation through to final results.



## 6.1 EBSD data and RVE generation

The EBSD map shown in Figure 6.2 is for an equiaxed Ti-6Al-4V microstructure. In addition to the image, the EBSD data also provides data on grain sizes and orientations in terms of Euler angles using the Bunge convention. The average grain size for each phase can then be calculated and used to inform the creation of the RVEs. The orientation data will be used to write the inform file for the simulation, therefore each grain will have an orientation assigned to it.

For this project, 100 grains was deemed large enough to reduce the percentage of grains affected by the boundary conditions, therefore giving a more reliable model, whilst maintaining a reasonable simulation run time.

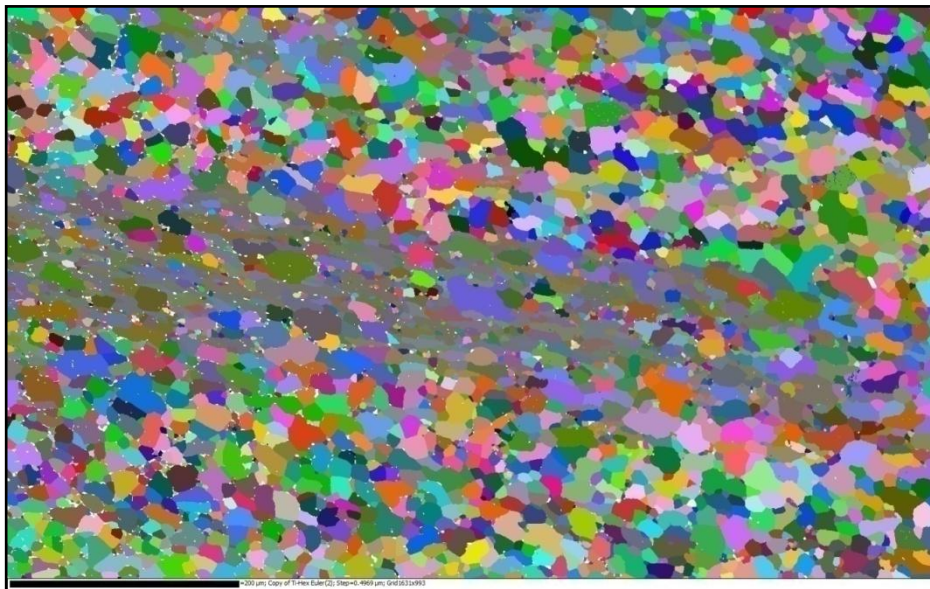


**Figure 6.2:** Ti-6Al-4V EBSD map showing the variety of grain sizes and there distribution.

The RVE for the simulations consisted of 102 grains, 30 beta grains and 72 alpha grains, with a volume fraction of 3.5% beta. The RVE has an average alpha grain volume of  $753 \mu\text{m}^3$  and the beta grains have an average volume of  $66 \mu\text{m}^3$ . The average beta volume is higher than the EBSD data due to the configuration of the alpha and beta seed points, for which an optimal configuration could not be found that constrained the betas to a volume matching that of experimental data. The RVE was meshed with 2366 hexahedral elements

## 6.2 Macroscale modelling of RVE

### 6.2.1 Rate independent case

In this simulation the RVE is subjected to an axial tensile loading condition at a quasi-static rate, for which the parameters are in Appendix A. In this case a match between the simulation and the quasi-static uniaxial tensile experiment by M. Wojtaszek [82] is to be sought. Matching the experiment would prove that the model constructed from grain level properties could predict the macroscale response of the alloy.

For the simulation the RVE is constrained, such that the nodes on the XZ plane are fixed in the Y direction but free to move in the X and Z directions. In addition to this the nodes along the axis where X equals zero are fixed so they cannot move in the Z direction as well as the Y direction. Lastly, the origin node is fully fixed so that no movement is permitted in any direction. The XZ plane at  $Y = 33 \mu\text{m}$  is subjected to a uniaxial tensile load, at a strain rate of  $2e^{-3}$ . Figure 6.3 shows the true stress-strain curve obtained from the experiment by Wojtaszek [82] and the curve obtained by the simulation of the RVEA MATLAB code is used to calculate the current cross sectional area of the fixed surface at any given iteration, along with summing the total reaction forces of the nodes upon that surface. The true stress is then calculated by dividing the total reaction force acting upon the surface by the current cross sectional area.

It can be seen from Figure 6.3 that the simulation captures the general trends of Titanium 6Al-4V, however, the exact values of true stress are not captured. This is most likely down to the hardening curve used for the simulation. The values for the CRSS for each of the families' slip systems came from the paper by Warwick [33] along with the equation that governs the hardening curve. These values appear to be close to the values for single crystals, but the experiment used a material with multiple grains. This may lead to a slight difference in values as slip can occur on multiple systems at the same time.

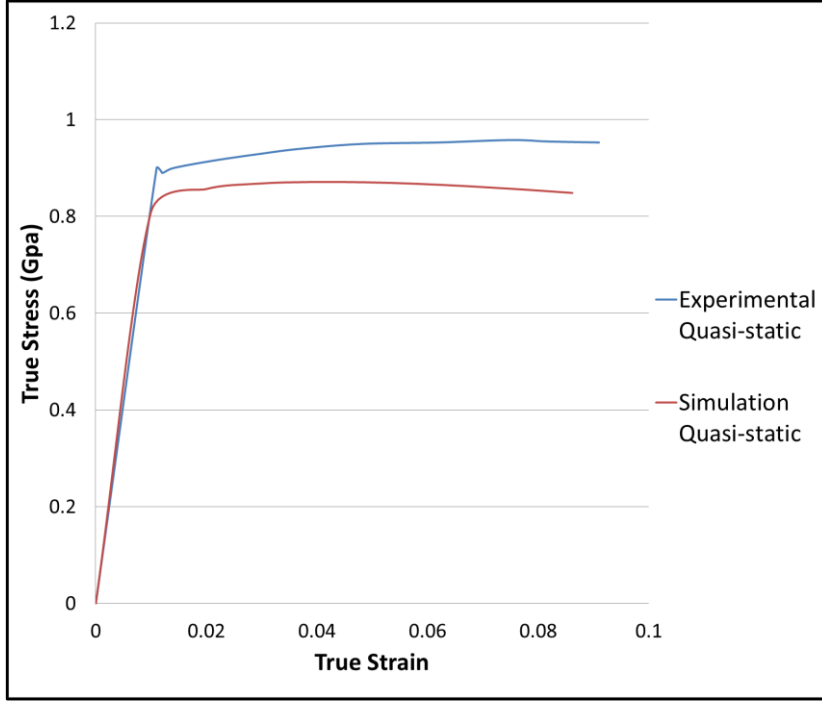


**Figure 6.3:** Comparison of True Stress - Strain curves for experimental and simulated Quasi-static rate case.

This therefore means more localised testing of single grains is necessary to find the exact CRSS values for each and every slip system within the material. However, this was not feasible within the scope of the current project. With more specialised testing the hardening curve could also be improved as well, although the shape of the hardening is well defined by the Vocé equation from Warwick's [33] paper.

$$\tau^s = \tau_0^s + (\tau_1^s + \theta_1^s \Gamma) \left( 1 - \exp\left(\frac{-\theta_0^s \Gamma}{\tau_1^s}\right) \right). \quad (6.1)$$

For use in HYPLAS the hardening curve must be in a series of data points relating plastic strain to expected stress. In this research a MATLAB code was used to calculate the expected stress for a given set of plastic strains through the use of equation (6.1) and output them to separate text files. Due to the formulation of the rate equation (4.24) setting  $\mu$  or  $\epsilon$  to zero would cause a divide by zero within the equation. For this simulation the hardening parameters were set close to zero to obtain the rate independent case.

The deformed configuration of the grains in the RVE (Figure 6.4) shows the new positions of the grain boundaries at the final time step. This is useful when compared to stress distributions of the RVE in Figure 6.5.

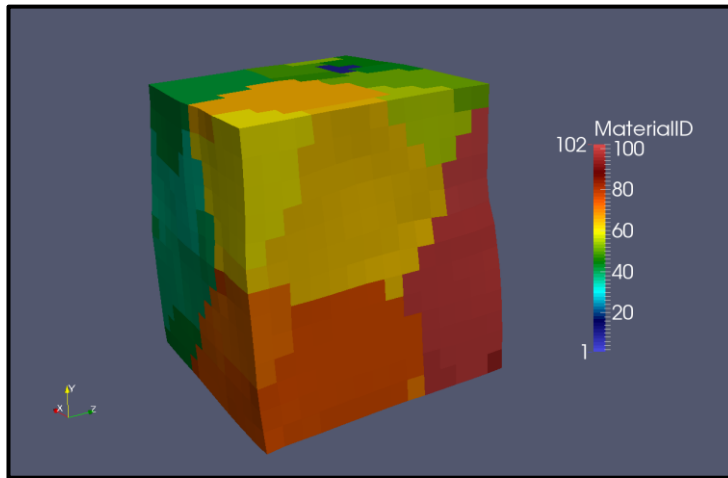


**Figure 6.4:** Grains in the final deformed configuration showing the positions of grain boundaries. The colouring is based on the material ID, not the grain orientation.

It can be seen that there is a build up of stress at the grain boundaries. This is to be expected as slip is inhibited by the grain boundary. This means the slipping grain is not free to deform as it wishes due to the different orientation of the neighbouring grain. The images of the stresses in the YY and ZZ direction have good examples of this occurring with the red and yellow areas being zones of high stress. The image of stress in the XZ direction also gives a good view of this, as the yellow band stretches from the near edge of the cube to the top edge. When the placement of this line is compared with the grain edge of the yellow grain that wraps round the top near edge of the RVE in Figure 6.4, it can be seen that it follows the grain boundary exactly.

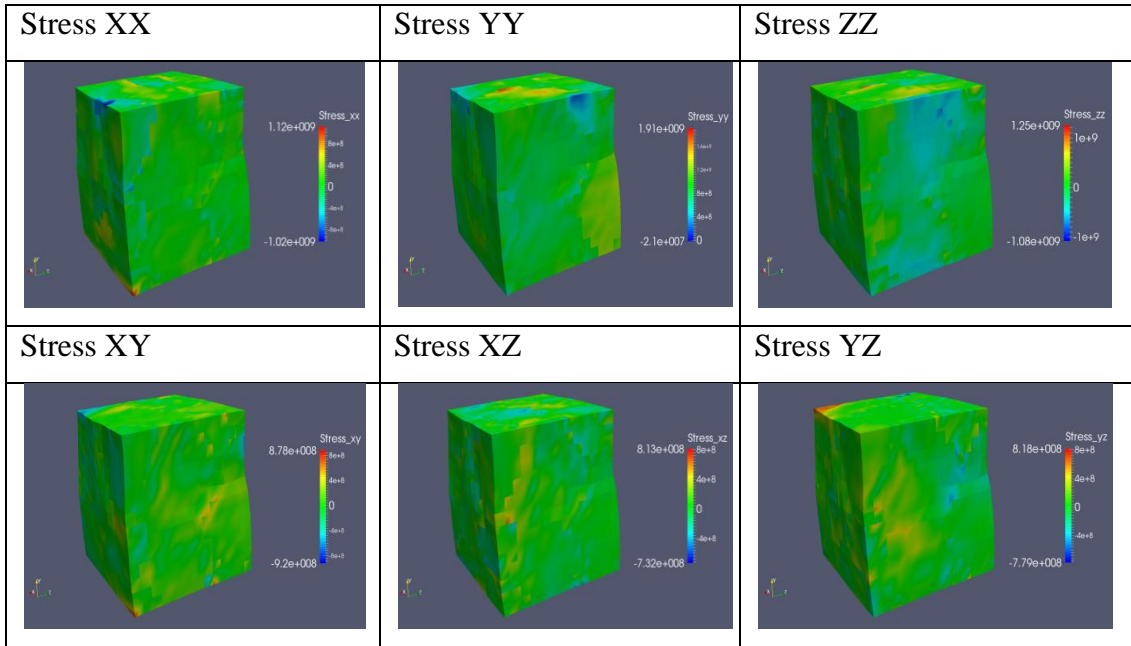


**Figure 6.5:** Stress distributions on RVE for Quasi-static uniaxial tension.

The model does not capture grain boundary sliding or other grain boundary effects as the grain boundaries are not explicitly modelled. The inhibition of slip across the grain boundaries is solely from mis-orientation of the grains and non-alignment of preferential slip systems.

### 6.2.2 High strain rate case

In this simulation a strain rate of 20 is used on the RVE with the same loading conditions as outlined in section 6.2.1. The rate sensitivity parameters have been set as  $\mu = 0.08$  and  $\epsilon = 0.666$ . where the value of  $\epsilon$  is calculated from Bridier's [40] paper, where he specifies the inverse rate sensitivity parameter.  $\mu$  on the other hand has been set to try and match the macro curve of the high strain rate experiment of Wojtaszek [82].

The rest of the material parameters are as they were for the quasi-static case in section 6.2.1, which are found in appendix A. The same amount of strain is applied to the RVE of 10% as in the quasi-static case. Figure 6.6 shows the response of the simulation in relation to that obtained by Wojtaszek [82] in his experiment.

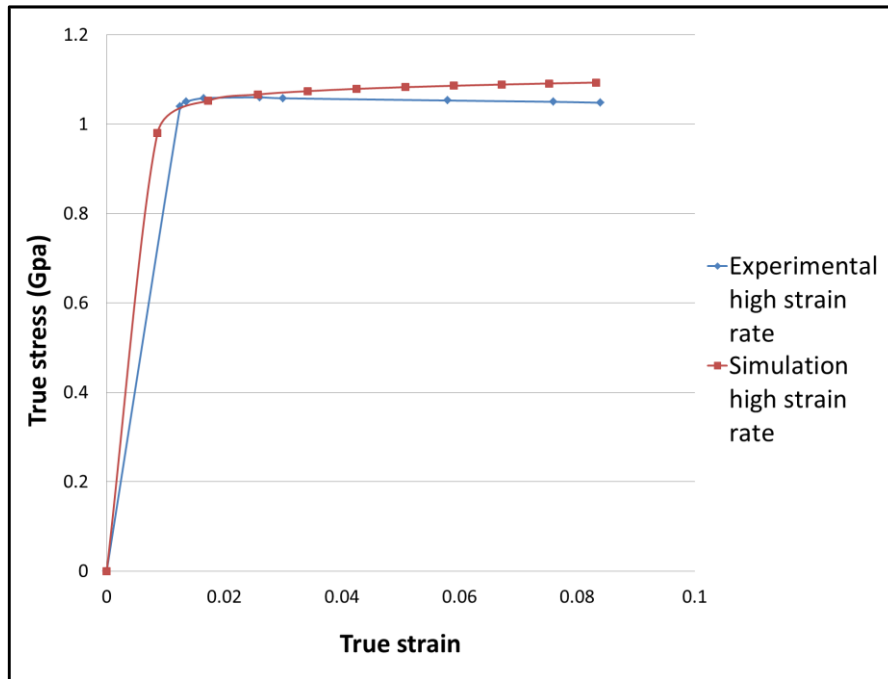


**Figure 6.6:** Comparison of Experimental and simulation response to a high strain rate loading condition.

From Figure 6.6 it can be seen that the height of the simulation curve gives a good match to that obtained by the experiment. This shows that the rate sensitivity of the material can be captured as a general trend. In this case though a more defined set of rate parameters are needed. As can be seen the curve has deviated from the elastic region. It is believed that the  $\mu$  parameter could be too high, in which case the  $\epsilon$  parameter needs to be increased. This would therefore be in contradiction to Bridier's [40] paper where the inverse of rate sensitivity parameter is given as fifteen. Again it is clear that more study is needed in the parameters needed to accurately model titanium in this way. The model is capable of capturing the rate sensitivity as long as the right parameters have been found. Figure 6.7 shows the grains in the final deformed state. Again the colouring is the material ID of the grain, not the orientation. Figure 6.8 shows the distribution of the stresses over the RVE for the high strain case.

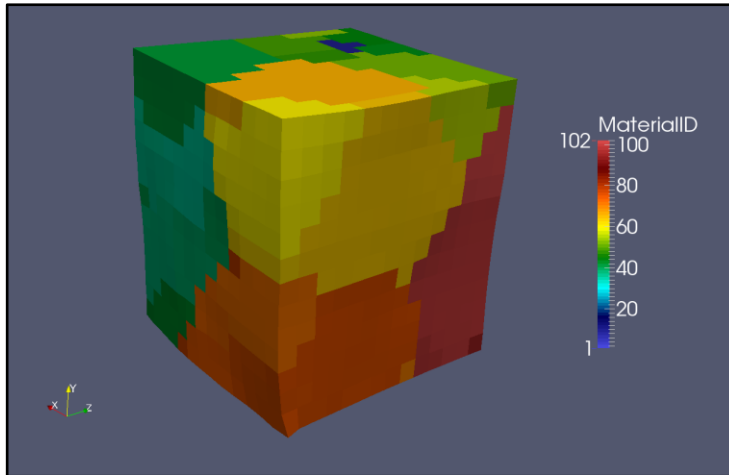


**Figure 6.7:** Grain deformation for high strain rate loading.

In Figure 6.8 the stresses can be seen to be highest at the grain boundaries. This is expected due to the inhibition of slip across grain boundaries as explained in the quasi-static case. The image of the stress in the YZ direction clearly shows several grain boundaries that are acting as slip inhibitors. It can be seen that more slip is trying to happen in the high strain rate case compared to the quasi static case.

Comparing the images for stress in YZ direction in Figures 6.5 and 6.8 it can be seen that more boundaries have stress acting upon them. This is likely due to more non-preferential slip systems being activated due to the higher strain rate and therefore having to accommodate plastic deformation in a shorter time frame.

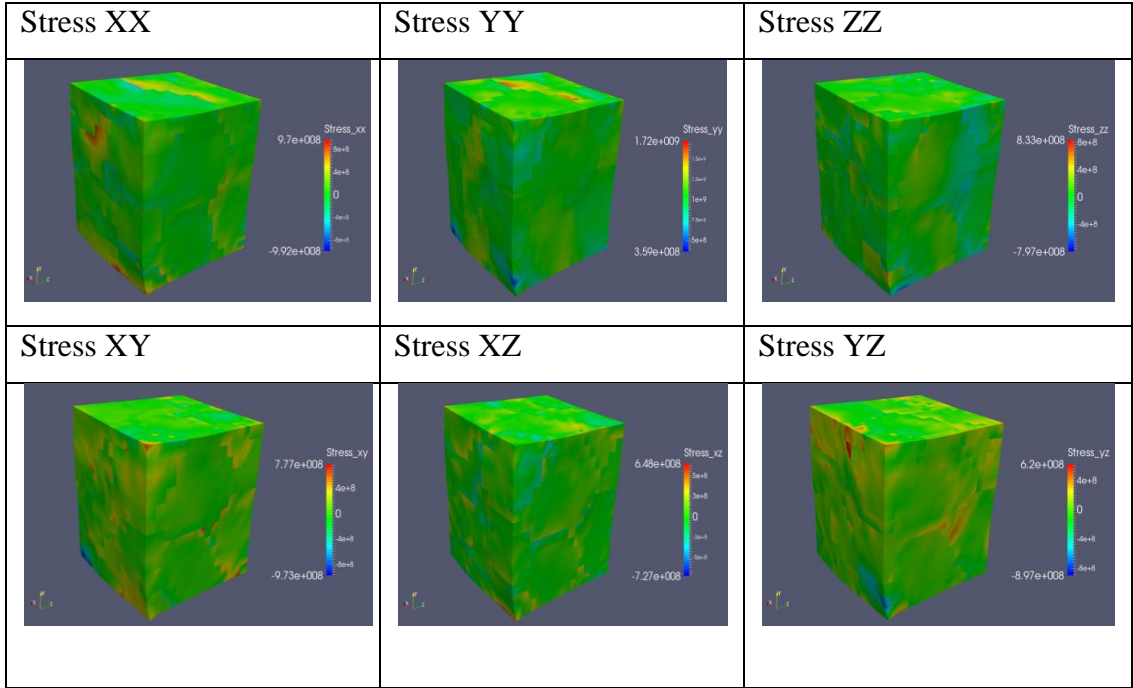


**Figure 6.8:** Distribution of stresses on RVE for high strain rate.

### 6.3 Microscopic modelling of RVE

In the previous sections of this chapter the RVE has been subjected to macroscale loading to try and match it to macroscale true stress-strain curves. In this section the RVE has a deformation gradient prescribed to it and has a periodic boundary condition set. This closer mimics what grains would experience in the bulk material, with the loads coming from the surrounding metal rather than being directly applied as in the macroscale tests.

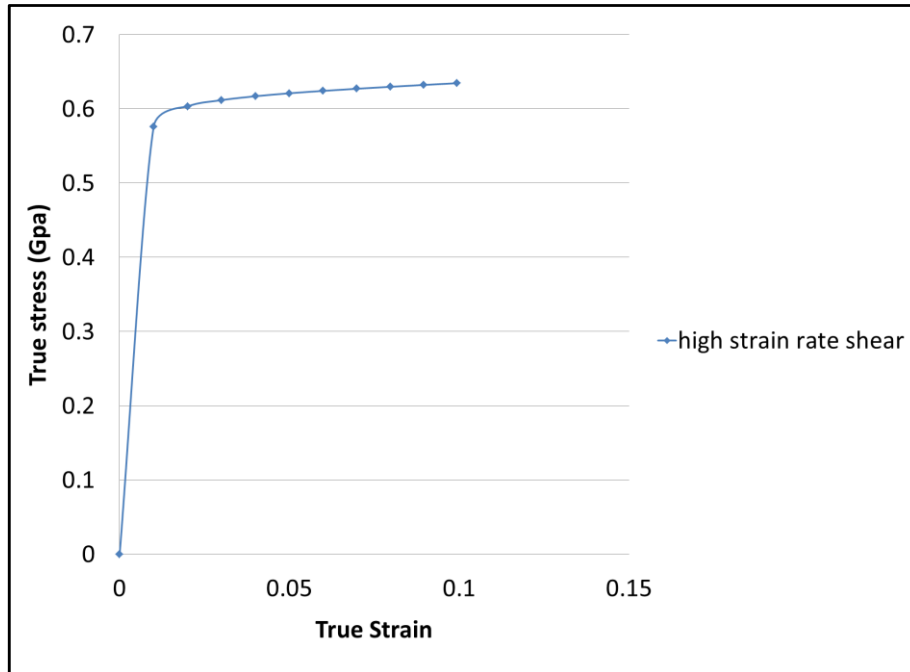
The advantage of the microscale modelling is deformations that are difficult to carry out in reality can be imposed. When the RVE has periodic boundary conditions these represent what happens to the microstructure for a given macroscale deformation, which is applied through the use of the deformation gradient.

In this section a deformation gradient as shown in equation (6.2) is applied to the same 102 grain RVE as used before in the macroscale simulations.

$$\mathbf{F} = \begin{bmatrix} 1.0 & 0.2 & 0.0 \\ 0.0 & 1.0 & 0.0 \\ 0.0 & 0.0 & 1.0 \end{bmatrix}. \quad (6.2)$$



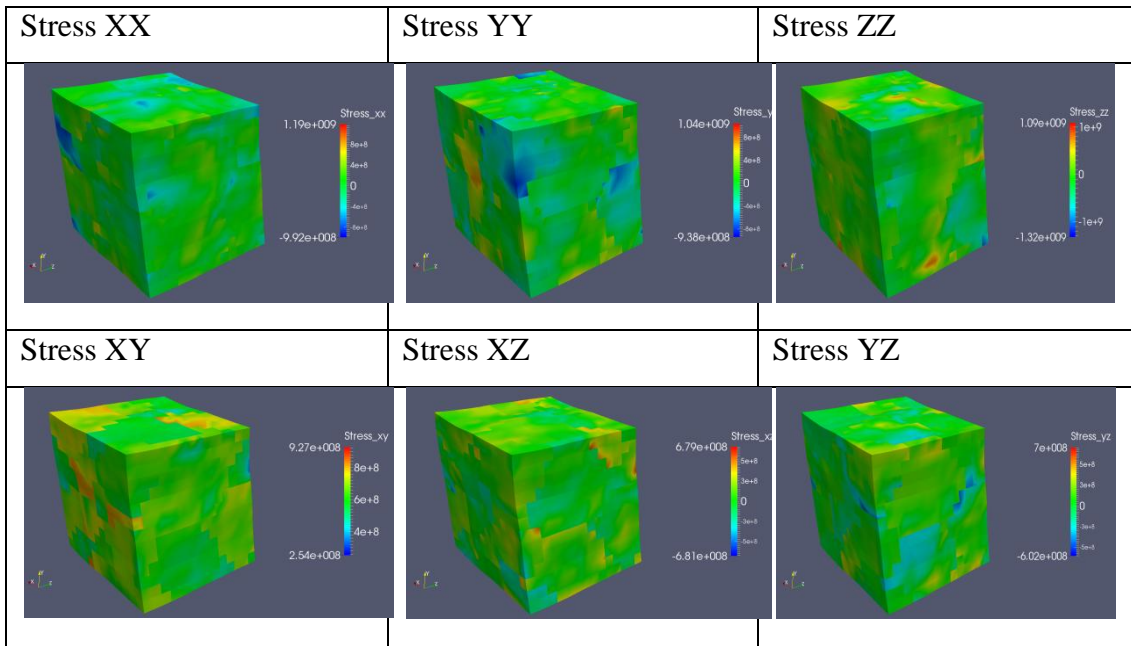
The material parameters are set as before as well as the rate sensitivity parameters from the high strain rate case of section 6.2.2. Figure 6.9 shows the response of the RVE to the applied deformation gradient as shown in equation (6.2). The simulation is again run at a strain rate of 20.



**Figure 6.9:** True stress -strain response of the RVE.

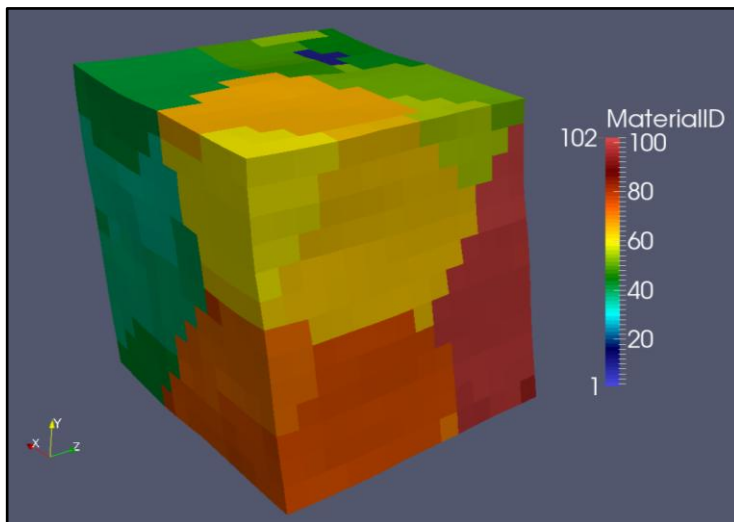
Figure 6.9 shows the homogenised stress of the RVE against the true strain for the shear loading in the XY direction. Even at the microscale level we still see a sharp transition from the elastic to the plastic region.

Figure 6.10 shows the stress distributions in the different directions upon the RVE. Again we see the stress concentrations around the grain boundaries from the resistance of slip across different orientated grains.



**Figure 6.10:** Stress distribution for shear loading in microscale.

This can especially be seen in the *ZZ* direction when it is compared to the grain image in Figure 6.11. We also see significant stress concentrations in the *XY* direction.



**Figure 6.11:** Deformed grains in microscale shear.

## **Chapter 7 Conclusions**

### **7.1 Research outcomes**

In this research a three dimensional hyperelastic-viscoplastic single crystal constitutive model is outlined. This model uses the perić rate law with yield surfaces. The model allows for each slip family to have its own unique set of governing variables that allows for a more customisable material.

A process for creating RVEs with the correct volume fraction of beta phase has been described. This method also produces alpha grain sizes that match well with the EBSD data. The beta grains, however, are bigger than is found in the EBSD data and this is due to the seed point generation and grain growth process used in this thesis.

Simulations show that the model can capture the trends of titanium 6Al-4V at the macro scale, though an exact match was not achieved with the experimental data. The simulations also show that an applied deformation gradient can be placed upon the RVE with periodic boundary conditions that mimic the surrounding metal.

This model allows for early stage alloy development as it captures the trends of the alloy. This is helpful to manufacturers as they can explore the effect of different parameters upon the material response. This allows them to see what ideas are worth pursuing before committing to more expensive sample manufacture and testing.

### **7.2 Looking forward**

Moving on from this research a few points of interest that the author feels would be useful to the advancement of this current method are:

1. A more in-depth analysis of CRSS values and hardening curves. The values used in this research have given results that show the general trends of the material. These values, however, do not give the exact values that are obtained by the experiments. Obtaining more fine-tuned values would help provide a closer match to the experimental values and therefore give a more accurate representation of the materials response.
2. A more in-depth analysis of rate sensitivity parameters. Again the more accurate the values the closer the simulation results will be to the

experiments. It will also give better predictions of the rate dependence of the material.

3. Adding a thermal component so that thermal effects can be taken into account, allowing for more investigations.
4. Incorporating the twinning mechanism. This mechanism is more prevalent in lower aluminium content titanium alloys. Adding this would allow for more accurate simulations of the lower aluminium content alloys.

The current method lays down a starting point for more advanced simulations that capture more of the micro structural effects and how they affect the macro scale response. This method should allow for a bottom up approach to preliminary designing of new titanium alloys.

## Appendix

**Table 1: Elastic properties and CRSS values [33].**

Property	Value (Gpa)
Bulk modulus alpha phase	43.99
Shear modulus alpha phase	106.43
Bulk modulus beta phase	20.7
Shear modulus beta phase	87.7
B1 CRSS	0.29
B2 CRSS	0.31
B3 CRSS	0.35
Basal CRSS	0.33
Prismatic CRSS	0.35
Pyramidal CRSS	0.38
Pyramidal 1 <sup>st</sup> order	0.49
Pyramidal 2 <sup>nd</sup> order	0.52

**Table 2: Vocé hardening parameters [33].**

Slip system	$\tau_1$	$\theta_0$	$\theta_1$
B1	0.3	0.1	0.5
B2	0.3	0.1	0.5
B3	0.3	0.1	0.5
Basal	0.01	0.01	0.01
Prismatic	0.15	0.4	0.01
Pyramidal	0.01	0.01	0.01
Pyramidal 1 <sup>st</sup> order	0.01	0.1	0.08
Pyramidal 2 <sup>nd</sup> order	0.01	0.7	0.08

## References

- [1] F. Team, “Strong recovery in air travel and freight traffic.” [Online]. Available: [http://www.finfacts.ie/irishfinancenews/article\\_1020256.shtml](http://www.finfacts.ie/irishfinancenews/article_1020256.shtml). [Accessed: 13-May-2016].
- [2] R. A. Dolbeer, S. E. Wright, J. Weller, and M. J. Begier, “Wildlife Strikes to Civil Aircraft In The United States 1990-2012. Federal Aviation Administration, National Wildlife Strike Database. Serial Report Number 19,” Washington, DC, 2013.
- [3] R. A. D, W. Services, and L. Drive, “Population trends of resident and migratory Canada geese in relation to strikes with civil aircraft,” *Human-Wildlife Interact.*, vol. 8, no. 1, pp. 88–99, 2014.
- [4] J. B. Dunning Jr., Ed., *CRC Handbook of Avian Body Masses*, Second. Boca-Raton: CRC Press, 2007.
- [5] B. MacKinnon, R. Sowden, and S. Dudley, Eds., *Sharing the Skies: an aviation guide to management of wildlife hazards*. Ottawa: Civil Aviation and Communications Centre, 2001.
- [6] R. Dolbeer, “Amplified birdstrike risks related to population increases of large birds in North America,” in *Proceedings of the 26th International Bird Strike Committee*, no. Volume 1, pp. 48–67.
- [7] R. A. Dolbeer, “Trends in Wildlife Strike Reporting, Part 1 - Voluntary System 1990-2008,” Washington, D.C., 2009.
- [8] R. and I. T. Administration, “National transportation statistics, Tables 1–13: active U.S. air carrier and general aviation fleet by type of aircraft.” .
- [9] P. P. Marra, C. J. Dove, R. Dolbeer, N. F. Dahlan, M. Heacker, J. F. Whatton, N. E. Diggs, C. France, and G. Henkes, “Migratory Canada geese cause crash of US Airways Flight 1549,” *Front. Ecol. Environ.*, 2009.
- [10] C. E. Marek Darecki Tom Enders, Emma Fernandez, Peter Hartman, Jean-Paul Herteman, Micheal Kerkloh, Ian King, Patrick Ky, Micheal Mathieu, Giuseppe Orsi, Gerald Schotman, Colin Smith, Johann-Dietrich Worner, “Flightpath 2050 Europe’s Vision for Aviation.” Publications office of the European Union, Luxembourg, 2011.
- [11] A. Alankar, P. Eisenlohr, and D. Raabe, “A dislocation density-based crystal plasticity constitutive model for prismatic slip in alpha-titanium,” *Acta Mater.*, vol. 59, no. 18, pp. 7003–7009, 2011.

- [12] H. W. Meyer Jr and D. S. Kleponis, "Modeling the high strain rate behavior of titanium undergoing ballistic impact and penetration," *Int. J. Impact Eng.*, vol. 26, no. 1–10, pp. 509–521, 2001.
- [13] M. Hamid Pourian, P. Pilvin, F. Bridier, and P. Bocher, "Modeling the elastoplastic behaviors of alpha Ti-alloys microstructure using Cellular Automaton and finite element methods," *Comput. Mater. Sci.*, vol. 99, pp. 33–42, Mar. 2015.
- [14] F. P. E. Dunne, D. Rugg, and A. Walker, "Lengthscale-dependent, elastically anisotropic, physically-based hcp crystal plasticity: Application to cold-dwell fatigue in Ti alloys," *Int. J. Plast.*, vol. 23, no. 6, pp. 1061–1083, Jun. 2007.
- [15] G. Kugler and R. Turk, "Study of the influence of initial microstructure topology on the kinetics of static recrystallization using a cellular automata model," *Comput. Mater. Sci.*, vol. 37, no. 3, pp. 284–291, Sep. 2006.
- [16] R. Ding and Z. X. Guo, "Microstructural modelling of dynamic recrystallisation using an extended cellular automaton approach," *Comput. Mater. Sci.*, vol. 23, no. 1–4, pp. 209–218, Apr. 2002.
- [17] K. G. F. Janssens, "An introductory review of cellular automata modeling of moving grain boundaries in polycrystalline materials," *Math. Comput. Simul.*, vol. 80, no. 7, pp. 1361–1381, Mar. 2010.
- [18] T. Sourmail, "No Title." [Online]. Available: <http://thomas-sourmail.net/coatings/materials.html>. [Accessed: 13-May-2016].
- [19] G. P. Dinda, L. Song, and J. Mazumder, "Fabrication of Ti-6Al-4V Scaffolds by Direct Metal Deposition," *Metall. Mater. Trans. A*, vol. 39, no. 12, pp. 2914–2922, 2008.
- [20] A. F. Gerday, M. Ben Bettaieb, L. Duchêne, N. Clement, H. Diarra, and A. M. Habraken, "Material behavior of the hexagonal alpha phase of a titanium alloy identified from nanoindentation tests," *Eur. J. Mech. - A/Solids*, vol. 30, no. 3, pp. 248–255, 2011.
- [21] G. E. Dieter, *Mechanical Metallurgy SI Metric Edition*, Third. London: McGraw-Hill, 1988.
- [22] R. Clark and B. Chalmers, "Mechanical deformation of aluminium bicrystals," *Acta Metall.*, vol. 2, no. 1, pp. 80–86, 1954.
- [23] N. J. Petch and I. J. Iron Steel, "No Title," *London*, vol. 173, p. 25, 1953.
- [24] B. Bhav Singh, G. Sukumar, A. Bhattacharjee, K. Siva Kumar, T. Balakrishna

- Bhat, and A. K. Gogia, "Effect of heat treatment on ballistic impact behavior of Ti-6Al-4V against 7.62 mm deformable projectile," *Mater. Des.*, vol. 36, no. 0, pp. 640–649, 2012.
- [25] D.-G. Lee, Y. G. Kim, D.-H. Nam, S.-M. Hur, and S. Lee, "Dynamic deformation behavior and ballistic performance of Ti-6Al-4V alloy containing fine  $\alpha_2$  (Ti<sub>3</sub>Al) precipitates," *Mater. Sci. Eng. A*, vol. 391, no. 1–2, pp. 221–234, 2005.
- [26] D.-G. Lee, Y. Lee, S. Lee, C. Lee, and S.-M. Hur, "Dynamic deformation behavior and ballistic impact properties of Ti-6Al-4V alloy having equiaxed and bimodal microstructures," *Metall. Mater. Trans. A*, vol. 35, no. 10, pp. 3103–3112, 2004.
- [27] S. Liao and J. Duffy, "Adiabatic shear bands in a Ti-6Al-4V titanium alloy," *J. Mech. Phys. Solids*, vol. 46, no. 11, pp. 2201–2231, 1998.
- [28] J. Peirs, W. Tirry, B. Amin-Ahmadi, F. Coghe, P. Verleysen, L. Rabat, D. Schryvers, and J. Degrieck, "Microstructure of adiabatic shear bands in Ti6Al4V," *Mater. Charact.*, vol. 75, pp. 79–92, 2013.
- [29] Z. W. Wyatt, W. J. Joost, D. Zhu, and S. Ankem, "Deformation mechanisms and kinetics of time-dependent twinning in an alpha-titanium alloy," *Int. J. Plast.*, vol. 39, pp. 119–131, 2012.
- [30] H. Abdolvand and M. R. Daymond, "Multi-scale modeling and experimental study of twin inception and propagation in hexagonal close-packed materials using a crystal plasticity finite element approach-Part I: Average behavior," *J. Mech. Phys. Solids*, vol. 61, no. 3, pp. 783–802, 2013.
- [31] X. Feaugas and M. Clavel, "Cyclic deformation behaviour of an alpha/beta titanium alloy—i. micromechanisms of plasticity under various loading paths," *Acta Mater.*, vol. 45, no. 7, pp. 2685–2701, 1997.
- [32] T. Neeraj, D. H. Hou, G. S. Daehn, and M. J. Mills, "Phenomenological and microstructural analysis of room temperature creep in titanium alloys," *Acta Mater.*, vol. 48, no. 6, pp. 1225–1238, 2000.
- [33] J. L. W. Warwick, J. Coakley, S. L. Raghunathan, R. J. Tailing, and D. Dye, "Effect of texture on load partitioning in Ti-6Al-4V," *Acta Mater.*, vol. 60, no. 10, pp. 4117–4127, 2012.
- [34] J. R. Mayeur and D. L. McDowell, "A three-dimensional crystal plasticity model for duplex Ti-6Al-4V," *Int. J. Plast.*, vol. 23, no. 9, pp. 1457–1485,



Sep. 2007.

- [35] H. Ledbetter, H. Ogi, S. Kai, S. Kim, and M. Hirao, “Elastic constants of body-centered-cubic titanium monocrystals,” *J. Appl. Phys.*, vol. 95, no. 9, pp. 4642–4644, 2004.
- [36] I. P. Jones and W. B. Hutchinson, “Stress-state dependence of slip in Titanium-6Al-4V and other H.C.P. metals,” *Acta Metall.*, vol. 29, no. 6, pp. 951–968, Jun. 1981.
- [37] J. Gong and A. J. Wilkinson, “Anisotropy in the plastic flow properties of single-crystal alpha titanium determined from micro-cantilever beams,” *Acta Mater.*, vol. 57, no. 19, pp. 5693–5705, 2009.
- [38] J. C. Williams, R. G. Baggerly, and N. E. Paton, “Deformation behavior of HCP Ti-Al alloy single crystals,” *Metall. Mater. Trans. A*, vol. 33, no. 13, pp. 837–850, 2002.
- [39] F. Han, B. Tang, H. Kou, J. Li, and Y. Feng, “Experiments and crystal plasticity finite element simulations of nanoindentation on Ti–6Al–4V alloy,” *Mater. Sci. Eng. A*, vol. 625, no. 0, pp. 28–35, 2015.
- [40] F. Bridier, D. L. McDowell, P. Villechaise, and J. Mendez, “Crystal plasticity modeling of slip activity in Ti–6Al–4V under high cycle fatigue loading,” *Int. J. Plast.*, vol. 25, no. 6, pp. 1066–1082, 2009.
- [41] J. Gong and A. Wilkinson, “Investigation of elastic properties of single-crystal  $\alpha$ -Ti using microcantilever beams,” *Philos. Mag. Lett.*, vol. 90, no. 7, pp. 503–512, 2010.
- [42] T. R. Bieler and S. . Semiatin, “The origins of heterogeneous deformation during primary hot working of Ti–6Al–4V,” *Int. J. Plast.*, vol. 18, no. 9, pp. 1165–1189, Sep. 2002.
- [43] A. F. Gerday, M. Ben Bettaieb, L. Duchêne, N. Clément, H. Diarra, and A. M. Habraken, “Interests and limitations of nanoindentation for bulk multiphase material identification: Application to the  $\beta$  phase of Ti-5553,” *Acta Mater.*, vol. 57, no. 17, pp. 5186–5195, Oct. 2009.
- [44] H. Abdolvand and M. R. Daymond, “Multi-scale modeling and experimental study of twin inception and propagation in hexagonal close-packed materials using a crystal plasticity finite element approach; part II: Local behavior,” *J. Mech. Phys. Solids*, vol. 61, no. 3, pp. 803–818, 2013.
- [45] B. . Seth, “Generalized strain measure with application to physical problems,”

- Second order Eff. elasticity, plasticity and fluid Dyn.*, pp. 162–172, 1964.
- [46] R. Hill, “Aspects of Invariance in Solid Mechanics,” *Adv. Appl. Mech.*, vol. 18, pp. 1–75, 1978.
- [47] R. W. Ogden, *Non-Linear Elastic Deformations*. Chichester: Ellis Horwood, 1984.
- [48] C. C. Wang and C. Truesdell, *Introduction to Rational Elasticity*. Leyden: Noordhoff.
- [49] M. . Gurtin, “The linear Theory of elasticity,” *Handb. der Phys.*, vol. VIa/2, pp. 1–295, 1972.
- [50] M. . Gurtin, *An Introduction to Continuum Mechanics*. New York, 1981.
- [51] M. . Gurtin and L. C. Martins, “Cauchy’s Theorem in classical physics,” *Arch. Rat. Mech. Anal.*, vol. 60, no. 4, pp. 305–324.
- [52] J. E. Marsden and T. J. R. Hughes, *Mathematical Foundations of Elasticity*. New Jersey: Prentice-Hall, 1983.
- [53] P. G. Ciarlet, “Mathematical Elasticity. Volume I: Three dimensional elasticity,” 1988.
- [54] E. A. de Souza Neto, D. Peric, and D. R. J. Owen, *Computational Methods for Plasticity: Theory and Applications*. Wiley, 2008.
- [55] C. Truesdell, *Rational Thermodynamics*. New York: McGraw-Hill, 1969.
- [56] M. Eckert, “Max von Laue and the discovery of X-ray diffraction in 1912,” *Ann. Phys.*, vol. 524, no. 5, pp. A83–A85, May 2012.
- [57] E. Schmid and W. Boas, *Plasticity of crystals: with special reference to metals*. London: F. A. Hughes & Co., 1950.
- [58] D. Peirce, R. J. Asaro, and A. Needleman, “AN ANALYSIS OF NONUNIFORM AND LOCALIZED DEFORMATION,” *Acta Metall.*, vol. 30, pp. 1087–1119, 1982.
- [59] R. J. Asaro, “Micromechanics of crystals and polycrystals,” *Adv. Appl. Mech.*, vol. 23, pp. 1–115, 1983.
- [60] R. J. Asaro and A. Needleman, “texture Development and strain hardening in rate dependent polycrystals,” *Acta Metall.*, vol. 33, pp. 923–953, 1985.
- [61] Q. Xue, M. A. Meyers, and V. F. Nesterenko, “Self-organization of shear bands in titanium and Ti-6Al-4V alloy,” *Acta Mater.*, vol. 50, no. 3, pp. 575–596, 2002.
- [62] L. Nervo, A. King, A. Fitzner, W. Ludwig, and M. Preuss, “A study of

- deformation twinning in a titanium alloy by X-ray diffraction contrast tomography,” *Acta Mater.*, vol. 105, pp. 417–428, 2016.
- [63] E. Alabort, P. Kontis, D. Barba, K. Dragnevski, and R. C. Reed, “On the mechanisms of superplasticity in Ti-6Al-4V,” *Acta Mater.*, vol. 105, pp. 449–463, 2016.
- [64] K. Havner, *finite plastic deformation of crystalline solids*. Cambridge: University press, 1992.
- [65] M. A. Meyers, R. W. Armstrong, and H. O. Kirchner, *Mechanics and materials: fundamentals and linkages*. Wiley, 1999.
- [66] F. Roters, P. Eisenlohr, L. Hantcherli, D. Tjahjanto, T. Bieler, and D. Raabe, “Overview of constitutive laws, kinematics, homogenization and multiscale methods in crystal plasticity finite-element modeling: Theory, experiments, applications,” *Acta Mater.*, vol. 58, no. 4, pp. 1152–1211, 2010.
- [67] T. Belytschko, W.-K. Liu, and B. Moran, *Nonlinear Finite Elements for Continua and Structures*. Chichester: Wiley, 2000.
- [68] O. Zienkiewicz, R. Taylor, and J. Zhu, *The Finite Element Method: Its Basis and Fundamentals*. Elsevier Science, 2005.
- [69] E. A. D. S. Neto and R. A. Feijóo, *Variational Foundations of Large Strain Multiscale Solid Constitutive Models : Kinematical Formulation*. Wiley, 2011.
- [70] E. A. de Souza Neto and R. A. Feijóo, “Variational foundations of large strain multiscale solid constitutive models: kinematical formulation,” *Adv. Comput. Mater. Model. From Class. to Multi-Scale Tech.*, pp. 341–378, 2010.
- [71] R. Hill, “A self-consistent mechanics of composite materials,” *J. Mech. Phys. Solids*, vol. 13, no. 4, pp. 213–222, 1965.
- [72] D. Peri, E. A. de Souza Neto, R. A. Feijóo, M. Partovi, and A. J. Carneiro Molina, “On micro-to-macro transitions for multi-scale analysis of non-linear heterogeneous materials : unified variational basis and finite element implementation,” *Int. J. Numer. Methods Eng.*, vol. 87, pp. 149–170, 2011.
- [73] C. Miehe, “Exponential Map Algorithm for Stress Updates in Anisotropic Multiplicative Elastoplasticity for Single Crystals,” *Int. J. Numer. Methods Eng.*, vol. 39, no. 19, pp. 3367–3390, Oct. 1996.
- [74] C. Miehe, “Multisurface thermoplasticity for single crystals at large strains in terms of eulerian vector updates,” *Int. J. Solids Struct.*, vol. 33, no. 20–22, pp. 3103–3130, Aug. 1996.

- [75] S. Falco, P. Siegkas, E. Barbieri, and N. Petrinic, "A new method for the generation of arbitrarily shaped 3D random polycrystalline domains," *Comput. Mech.*, vol. 54, no. 6, pp. 1447–1460, 2014.
- [76] S. Kumarit and S. K. Kurtz, "SIMULATION OF MATERIAL MICROSTRUCTURE USING A 3D VORONOI TESSELATION : CALCULATION OF EFFECTIVE THERMAL EXPANSION COEFFICIENT OF POLYCRYSTALLINE MATERIALS," *Acta Metall.*, vol. 42, no. 12, pp. 3917–3927, 1994.
- [77] F. Aurenhammer, "Voronoi Diagrams — A Survey of a Fundamental Data Structure," *ACM Comput. Surv.*, vol. 23, no. 3, pp. 345–405, 1991.
- [78] X. Xue, F. Righetti, H. Telley, T. M. Liebling, and A. Mocellin, "The laguerre model for grain growth in three dimensions," *Philos. Mag. Part B*, vol. 75, no. 4, pp. 567–585, Apr. 1997.
- [79] C. Lautensack and S. Zuyev, "Laguerre Tessellations," *Journées de Probabilites 2008, Lille, France*, 2008. [Online]. Available: <http://math.univ-lille1.fr/~heinrich/proba2008/slidesexpo/Zuyev.pdf>. [Accessed: 20-Sep-2016].
- [80] V. Randle and E. O., *Introduction to texture analysis, microtexture and orientation mapping*. Taylor & Francis, 2003.
- [81] R. Pederson, "Microstructure and Phase Transformation of Ti-6Al-4V," Lulea University of Technology, 2002.
- [82] M. Wojtaszek, A. Czulak, G. Weber, and W. A. Hufenbach, "Quasi-static and Dynamic tensile properties of Ti-6Al-4V alloy," *Arch. Metall. Mater.*, vol. 58, no. 4, pp. 1261–1265, 2013.